

NUMERICAL MODELING OF ANISOTROPIC GRANULAR MEDIA

Takeichi Kanzaki Cabrera

Dipòsit legal: Gi. 899-2014
<http://hdl.handle.net/10803/133834>



<http://creativecommons.org/licenses/by/4.0/deed.ca>

Aquesta obra està subjecta a una llicència Creative Commons Reconeixement

Esta obra está bajo una licencia Creative Commons Reconocimiento

This work is licensed under a Creative Commons Attribution licence



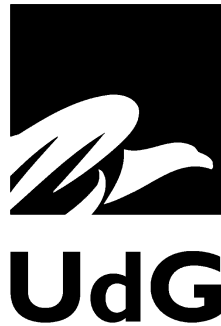
Universitat de Girona

Numerical modeling of anisotropic
granular media

PhD thesis
by

Takeichi Kanzaki Cabrera

2013



Universitat de Girona

PhD thesis

Numerical modeling of anisotropic granular media

Takeichi Kanzaki Cabrera

2013

Doctoral Programme in Technology

Thesis supervisors

Dr. Raúl Cruz Hidalgo

University of Navarra, Spain

Dr. Jordi Farjas Silva

Universitat de Girona, Spain

Report submitted to qualify for the PhD degree at the Universitat de Girona

To whom it might concern,

Dr. Raúl Cruz Hidalgo, Profesor Titular del Departamento de Física y Matemática Aplicada Universidad de Navarra.

Dr. Jordi Farjas Silva, Profesor Titular del Departament de Física de la Universitat de Girona.

CERTIFY that the study entitled "Numerical modeling of anisotropic granular media" has been carried out under their supervision by Takeichi Kanzaki Cabrera to obtain the PhD degree, and accomplishes all the requirements to be considered for the International Mention.

Girona, June 2013

Dr. Raúl Cruz Hidalgo
University of Navarra, Spain

Dr. Jordi Farjas Silva
Universitat de Girona, Spain

A ti,
que me has hecho todo lo que soy

The Spanish Government (Ministerio de Ciencia e Innovación) under research grant FIS2008-06034-C02-01/02 and the Universitat de Girona (PhD Fellowship Program) have supported this work.

The research stay of the author at the University of Twente has been founded by the Universitat de Girona (Movability Research Stay Program).

Acknowledgements - Agradecimientos

First of all I would like to say thanks to my supervisors, Dr. Raúl Cruz Hidalgo and Dr. Jordi Farjas Silva. Thanks for giving me this opportunity, for all the advices and for the time you devoted to me.

I would like to acknowledge the Department of Physics of the Universitat de Girona, and particularly to the research groups "Grup de Recerca en Materials i Termodinàmica" and "Analysis of Advanced Materials for Structural Design (AMADE)".

I would also like to thank the research group "Multi Scale Mechanics (MSM)" of the University of Twente, and specially to Professor Stefan Luding, Sebastian Gonzalez and Fabian Uhlig for their support and interesting discussions during my research stay at the University of Twente.

Professors Diego Maza, Iker Zuriguel, Ignacio Pagonabarraga and Fernando Alonso-Marroquin has also made a great contribution to this work with their wise advices and helpful professional exchanges.

There are many people to whom I owe a lot, without you it would have been impossible to finish this work, many thanks to you all.

Als col·legues d'AMADE, moltes gràcies per el vostre suport, per donar-me la benvinguda a casa vostra, per els anys compartits, per les discussions a la sobre taula, per els partits de futbol jugats.

A mi **mamá**, sin ti nada de esto hubiera pasado, muchas gracias por intentar educarme, que no te lo he puesto nada fácil, por enseñarme que hay que **luchar** por lo que uno quiere, y por los que uno quiere, por estar **siempre** ahí, simplemente, **GRACIAS**.

A la meva **dona**, per tot el **suport** que m'has donat, per estar al **meu costat**, per no donar-me **treva** els dies que no reaccionava, t'estimo amor.

A la vertiente cubana de mi familia, mi abuela, tío, tías, primos, mi papá, hermanas, mi familia es un dibujo, pero es **mi dibujo**. Al vessant català de la familia, moltes gràcies per fer-me sentir **com a casa**, per mitigar la sensació de no tenir l'altra part de la familia a prop.

A mis **amigos**, a los de verdad, a los que **siempre estuvieron ahí**, cuando los momentos no eran tan buenos, **i encara hi són**. A **Raúl**, sin ti no estaría aquí, a Carmen, Tatá, Claudia, M.J., mi pequeña familia al llegar.

**Una vez más, a mis dos mujeres, mis bastones, mis dos amores,
mis dos niñas.**

List of Published papers

As a result of the present work there have been published the following papers:

- Pagonabarraga, I.; Kanzaki, T.; Hidalgo, R.C. *The European Physical Journal Special Topics*, **179**, pp.43-53 (2009) doi:10.1140/epjst/e2010-01193-3
- Kanzaki, T.; Hidalgo, R.C.; Maza, D.; Pagonabarraga, I. "Cooling dynamics of a granular gas of elongated". *J. Stat. Mech.* **2010** (2010) P06020 doi:10.1088/1742-5468/2010/06/P06020
- Kanzaki, T; M. Acevedo, I. Zuriguel, I. Pagonabarraga, D. Maza, R. C. Hidalgo "Stress distribution of faceted particles in a silo after its partial discharge" *Eur. Phys. J. E* **34** 133 (2011) doi:10.1140/epje/i2011-11133-5
- R.C. Hidalgo, D. Kadau, T. Kanzaki and H. J. Herrmann "Granular packings of cohesive elongated particles" *Granular Matter* **14** 191-196 (2012) doi:10.1007/s10035-011-0303-2
- R.C. Hidalgo; Kanzaki, T; F. Alonso-Marroquin and S. Luding "On the use of graphics processing units (GPUs) for molecular dynamics simulation of spherical particles" *Powders & Grains 2013* 169-172 (2013) doi:http://dx.doi.org/10.1063/1.4811894

List of Figures

1.1	Interaction of two particles	10
1.2	Wall effect in MD simulations	14
1.3	Periodic boundary condition	15
1.4	Heterogeneous programming model	17
1.5	CPU and GPU Architecture	19
1.6	Evolution of FLOP	20
1.7	CUDA Heterogeneous Programming Model	21
2.1	Time evolution of the particle size densities	28
2.2	Scaled fragment size distribution (symmetric product kernels) . .	30
2.3	Scaled fragment size distribution (symmetric sum kernels)	31
2.4	Evolution of the normalized cumulative size density	32
2.5	Fragment size distribution	34
2.6	Normalized cumulative size density (asymmetric sum kernels) . .	35
2.7	Normalized cumulative size density (asymmetric product kernels)	36
2.8	Scaled fragment size distribution (asymmetric product kernel) . .	37
3.1	Particles interaction	43
3.2	Periodic boundary conditions	46
3.3	Spatial evolution of a system with $\gamma^N = 1s^{-1}$	48
3.4	Spatial evolution of a system with $\gamma^N = 10^3s^{-1}$	49
3.5	Evolution of the translational kinetic energy	50
3.6	Evolution of the rotational kinetic energy	51
3.7	Scaled speed distribution	53
3.8	Radial distribution function	55
3.9	Radial orientation distribution functions	55

3.10 Nematic parameter	57
4.1 Photograph of the experimental setup	60
4.2 Packings of square nuts and simulated particles	64
4.3 Experimental and numerical orientation distributions	65
4.4 Experimental and numerical orientation of the squares	67
4.5 Polar distribution of the principal directions of the <i>local stress</i>	69
4.6 Trace of the mean stress tensor after the silo loading	70
4.7 Trace of the mean stress tensor after the load for rods	71
4.8 Trace of the mean stress tensor after the load for squares	72
5.1 Simulated packings of elongated cohesive particles	76
5.2 Density profiles of different granular deposits	79
5.3 Orientation distributions of particles for two aspect ratios	80
5.4 Radial orientation distribution functions, $Q(r)$	82
5.5 Polar distribution of the principal direction	82
5.6 Profiles of the trace of the mean stress tensor	84
6.1 Cundall number behavior on CPU and GPU	89
6.2 Two bodies interaction	91
6.3 Flowchart of the granular gas simulation	94
6.4 Comparison of numerical with theoretical results	98
6.5 Scaled linear speed distribution	99
6.6 Scaled angular speed distribution	99
6.7 Cundall number behavior for different number of GPU	101

Contents

Summary	v
1 Introduction	1
1.1 Computational Physics	2
1.1.1 Monte Carlo method	3
1.1.2 Molecular Dynamics	5
1.2 Scientific programming	16
2 Collision induced fragmentation: a simple numerical algorithm	23
2.1 Mean Field Theory	24
2.2 Direct Simulation Monte Carlo Algorithm	25
2.3 Symmetric Kernels	28
2.3.1 Symmetric Deterministic Fragmentation	28
2.3.2 Symmetric Stochastic Fragmentation	29
2.4 Asymmetric Kernels	31
2.4.1 Asymmetric Deterministic Fragmentation	31
2.4.2 Asymmetric Stochastic Fragmentation	35
2.5 Discussion	38
3 Cooling dynamics of a granular gas of elongated particles	41
3.1 2D granular gas of irregular convex polygons	43
3.1.1 Boundary conditions	46
3.2 Freely evolving anisotropic grains	47
3.3 Discussion	57

4	Stress distribution of faceted particles in a silo	59
4.1	Experiment	60
4.2	Model of 2D Spheropolygons	62
4.3	Results	64
4.3.1	Packing Morphology	64
4.3.2	Micromechanics	68
4.4	Conclusions	73
5	Granular packings of cohesive elongated particles	75
5.1	2D spheropolygons with cohesion	75
5.2	Results and discussion	78
5.3	Conclusions	85
6	CUDA	87
6.1	GPGPU vs CPU benchmark	88
6.1.1	Realistic MD implementation of spheres on GPUs	90
6.1.2	Sphere Rotation on GPUs	91
6.2	Flowchart of the granular gas simulation	93
6.3	Validation	95
6.3.1	Equivalent dissipative parameters	96
6.3.2	Numerical Results	97
6.3.3	Optimal number of GPU	100
6.4	Conclusions	102
7	General conclusions	103
	Bibliography	128

Summary

Granular materials are multi-particle systems involved in many industrial process and everyday life. The mechanical behavior of granular media such as sand, coffee beans, planetary rings and powders are current challenging tasks. In the last years, these systems have been widely examined experimentally, analytically and numerically, and they continue producing relevant and unexpected results. Despite the fact that granular media are often composed of grains with anisotropic shapes like rice, lentils or pills, most experimental and theoretical studies have concerned spherical particles. The aim of this thesis have been to examine numerically the behavior of granular media composed by spherical and non-spherical particles. Our numerical implementations have permitted the description of the macroscopic properties of mechanically stable granular assemblies, which have been experimentally examined in a framework of the projects "Estabilidad y dinámica de medios granulares anisótricos" (FIS2008- 06034-C02-02) University of Girona and "Interacciones entre partículas y emergencia de propiedades macroscópicas en medios granulares" (FIS2008-06034-C02-01) University of Navarra.

The thesis is structured as follows. First, we have introduced the main concepts regarding the topics, which are studied in the subsequent chapters. Moreover, we also described the algorithms that are used to face the challenges that arise.

In Chapter 2, we introduced a numerical algorithm to describe the dynamic fragmentation in multi-particles systems. We have considered that fragmentation is induced by collisions between pairs of particles and perform numerical modeling for several classes of interaction kernels, and types of breakage models. The algorithm is validated by comparing our results with previous

analytical findings for symmetric and asymmetric kernels.

In Chapter 3, the cooling dynamics of a 2D granular gas of elongated particles is examined. We performed simulations on the temporal evolution of soft particles, using a molecular dynamics algorithm. For weakly dissipative particles, we found an homogeneous cooling process where the overall translational kinetic energy decreases analogously to viscoelastic circular particles. On the contrary, for strongly dissipative particles we observed an inhomogeneous cooling process where the diminishing of translational kinetic energy notably slows down. The rotational kinetic energy, however, always decays in agreement with Haff's prediction for the homogeneous cooling state of inelastic particles. We mainly found that the cooling kinetics of the system is controlled by the mechanisms that determine the local energy dissipation (collisions). However, we detected a strong influence of particle shape and inelasticity on the structure of the clusters which develop in the inhomogeneous cooling regimes. Our numerical outcomes suggest that strong dissipation and the particle anisotropy induce the formation of ordered cluster structures that retards the relaxation to the final asymptotic regime.

Experimental and numerical results of the effect that a partial discharge has on the morphological and micro-mechanical properties of non-spherical, convex particles in a silo are shown in Chapter 4. The comparison of the particle orientation when filling the silo and after its partial discharge reveals important shear induced orientation, which affects stress propagation. For elongated particles, the flow induces an increase in the packing disorder which leads to a reduction of the vertical stress propagation developed during the deposit generated prior to the partial discharge. For square particles, the flow favors particle alignment with the lateral walls promoting a behavior opposite to the one of the elongated particles: vertical force transmission, parallel to gravity, is induced. Hence, for elongated particles the flow developed during the partial discharge of the silo leads to force saturation with depth whereas for squares the flow induces hindering of the force saturation observed during the silo filling.

In Chapter 5 we examined the effect of an attractive force on the packing properties of two-dimensional elongated grains. In deposits of non-cohesive

rods in 2D, the topology of the packing is mainly dominated by the formation of ordered structures of aligned rods. Elongated particles tend to align horizontally and the stress is mainly transmitted from top to bottom, revealing an asymmetric distribution of local stress. However, for deposits of cohesive particles, the preferred horizontal orientation disappears. Very elongated particles with strong attractive forces form extremely loose structures, characterized by an orientation distribution, which tends to a uniform behavior when increasing the Bond number. As a result of these changes, the pressure distribution in the deposits changes qualitatively. The isotropic part of the local stress is notably enhanced with respect to the deviatoric part, which is related to the gravity direction. Consequently, the lateral stress transmission is dominated by the enhanced disorder and leads to a faster pressure saturation with depth.

In Chapter 6, we reported outcomes concerning the implementation on GPUs of an accurate molecular dynamics algorithm for a system of spheres. The new hybrid CPU-GPU implementation takes into account all the degrees of freedom, including the quaternion representation of 3D rotations. For additional versatility, the contact interaction between particles is defined using a force law of enhanced generality, which accounts for the elastic and dissipative interactions, and the hard-sphere interaction parameters are translated to the soft-sphere parameter set. We have proved that the algorithm complies with the statistical mechanical laws by examining the homogeneous cooling of a granular gas with rotation. The results are in excellent agreement with well established mean-field theories for low-density hard sphere systems. This technique dramatically reduces computational time, compared with the traditional CPU implementation.

Resumen

Los materiales granulares son sistemas de muchas partículas implicados en diversos procesos industriales y en nuestra vida cotidiana. El comportamiento mecánico de medios granulares, tales como arena, granos de café, anillos o polvos planetarios, representa actualmente todo un reto para la ciencia. En los últimos años estos sistemas se han estudiado ampliamente de forma experimental, analítica y numérica. Aún así, hoy día se continúan obteniendo resultados relevantes, y en muchas ocasiones, inesperados. A pesar del hecho de que los materiales granulares a menudo están compuestos por granos con forma anisotrópica, como el arroz, las lentejas o las píldoras, la mayoría de los estudios experimentales y teóricos se centran en partículas esféricas. El objetivo de esta tesis ha sido analizar numéricamente el comportamiento de los medios granulares compuestos por partículas esféricas y no esféricas. Los métodos numéricos implementados han permitido la descripción de las propiedades macroscópicas de pilas y columnas granulares, que se han examinado experimentalmente en el marco de los proyectos "Estabilidad y dinámica de medios granulares anisótropos" (FIS2008-06034-C02-02) de la Universidad de Girona y "Interacciones entre partículas y emergencia de propiedades macroscópicas en medios granulares" (FIS2008-06034-C02-01) de la Universidad de Navarra.

La tesis se estructura de la manera siguiente. En primer lugar, realizamos una introducción a los principales conceptos relacionados con los temas que se estudian en los capítulos siguientes. Además, se describen los algoritmos utilizados para resolver los retos que se plantean.

En el Capítulo 2 presentamos un algoritmo numérico para describir la dinámica de fragmentación en sistemas de múltiples partículas. Para este estudio hemos considerado que la fragmentación es inducida por las colisiones entre pares de partículas. De ese modo realizamos el modelado numérico para varias clases de *kernels* de interacción y para diferentes tipos de modelos de rotura. El algoritmo creado se validó comparando los resultados obtenidos con resultados analíticos, obtenidos por algunos colaboradores, para *kernels* simétricos y asimétricos.

En el Capítulo 3 estudiamos la dinámica de enfriamiento en gas granular de partículas alargadas en 2D. Realizamos simulaciones sobre la evolución temporal de un sistema de partículas blandas usando un algoritmo de dinámica molecular. Para sistemas poco disipativos, encontramos un proceso de enfriamiento homogéneo donde la energía cinética de traslación disminuye de forma análoga a los gases de partículas circulares visco-elásticas. Por otra parte, para partículas muy disipativas se observó un proceso de enfriamiento no homogéneo donde la disminución de la energía cinética de traslación se ralentiza de manera significativa. La energía cinética de rotación, sin embargo, siempre decae de acuerdo con la predicción de Haff para el estado de enfriamiento homogéneo de partículas inelásticas. Hemos encontrado que la cinética de enfriamiento del sistema está controlada por los mecanismos de disipación de energía local (las colisiones). Sin embargo, encontramos una fuerte influencia de la geometría y elasticidad de las partículas en la estructura de los *clusters* que se desarrollan en los regímenes de enfriamiento no homogéneo. Los resultados numéricos obtenidos sugieren que la alta disipación y la anisotropía de las partículas inducen la formación de *clusters* ordenados, que retardan la relajación a un régimen asintótico final.

Resultados experimentales y numéricos de los efectos de una descarga parcial sobre las propiedades morfológicas y micro-mecánicas de un silo de partículas convexas y no esféricas se muestran en el Capítulo 4. La comparación de la orientación de las partículas luego del llenado del silo y después de la descarga parcial revela cambios importantes en la orientación inducido por el *shear*, lo que afecta a la propagación del estrés. Para partículas alargadas, el flujo de llenado induce un aumento del desorden inicial, que conlleva a la reducción de la propagación de la tensión vertical desarrollada durante el proceso de depósito, antes de la descarga parcial. En el caso de las partículas cuadradas, el flujo favorece la alineación de las partículas con las paredes laterales del silo, lo que provoca un comportamiento opuesto al caso anterior. Es decir, se induce la transmisión del esfuerzo en dirección vertical. De ese modo, para las partículas alargadas, el flujo desarrollado durante la descarga parcial del silo induce la saturación del esfuerzo con la profundidad. Por el contrario, para los cuadrados, el flujo induce la obstaculización de la satu-

ración del esfuerzo con la profundidad.

En el Capítulo 5 examinamos el efecto de una fuerza de atracción sobre las propiedades de empaquetamiento de granos alargados. En depósitos de varillas no-cohesivas en 2D, la topología del empaquetamiento está dominada principalmente por la formación de estructuras ordenadas alineadas. Las partículas alargadas tienden a alinearse horizontalmente y la tensión se transmite, principalmente, de arriba a abajo, revelando una distribución asimétrica de la tensión local. Sin embargo, para los depósitos de partículas cohesivas, la tendencia a la orientación horizontal desaparece. Para partículas muy alargadas con fuertes fuerzas atractivas se forman estructuras muy desordenadas que se caracterizan por una distribución de la orientación, que tiende a un comportamiento uniforme cuando se incrementa el número de Bond. Como resultado de estos cambios, la distribución de la presión en los depósitos cambia cualitativamente. La parte isótropa de la tensión local aumenta notablemente con respecto a la parte desviadora, la cual está relacionada con la dirección de la gravedad. Por consiguiente, la transmisión de la tensión lateral está dominada por el aumento del desorden y conduce rápidamente a la saturación de la presión con la profundidad.

En el Capítulo 6 mostramos los resultados de la implementación de un algoritmo de dinámica molecular para un sistema de partículas esféricas, que utiliza el poder de cálculo de las GPU. El nuevo algoritmo híbrido CPU-GPU tiene en cuenta todos los grados de libertad de las partículas, incluida la representación en 3D de la rotación mediante *quaternions*. Para más versatilidad, la interacción entre las partículas se define mediante una fuerza generalizada, que representa las interacciones disipativas y elásticas. Los parámetros de interacción entre esferas duras se adaptaron para la interacción entre esferas blandas. Se demostró que el algoritmo desarrollado cumple con las leyes de la mecánica estadística mediante el estudio del enfriamiento homogéneo de un gas granular de esferas con rotación. Los resultados obtenidos concuerdan excelentemente con las teorías de campo medio para sistemas de baja densidad de partículas esféricas duras. Esta técnica reduce drásticamente el tiempo de cálculo en comparación con las implementaciones tradicionales sobre CPUs.

Resum

Els materials granulars són sistemes de moltes partícules implicats en diversos processos industrials i en la nostra vida quotidiana. El comportament mecànic de conjunts granulars, com la sorra, grans de cafè, anells o pols planetàries, representa actualment un repte per a la ciència. En els últims anys aquests sistemes s'han estudiat àmpliament de forma experimental, analítica i numèrica. De totes maneres, avui dia es continuen obtenint resultats rellevants, i en moltes ocasions, inesperats. Malgrat el fet que els materials granulars sovint estan compostos per grans amb forma anisotròpica, com l'arròs, les lleties o les píndoles, la majoria dels estudis experimentals i teòrics se centren en partícules esfèriques. L'objectiu d'aquesta tesi ha estat analitzar numèricament el comportament dels mitjans granulars compostos per partícules esfèriques i no esfèriques. Els mètodes numèrics implementats han permès la descripció de les propietats macroscòpiques de piles i columnes granulars, que s'han estudiat experimentalment en el marc dels projectes "Estabilidad y dinámica de medios granulares anisótropos" (FIS2008-06034-C02-02) de la Universitat de Girona i "Interacciones entre partículas y emergencia de propiedades macroscópicas en medios granulares" (FIS2008-06034-C02-01) de la Universitat de Navarra.

La tesi s'estructura de la següent manera. En primer lloc, realitzem una introducció als principals conceptes relacionats amb els temes que s'estudien en els capítols següents. A més, es descriuen els algorismes utilitzats per resoldre els reptes que es plantegen.

En el Capítol 2 presentem un algorisme numèric per descriure la dinàmica de fragmentació en sistemes de múltiples partícules. Per a aquest estudi hem considerat que la fragmentació és induïda per les col·lisions entre parells de partícules. D'aquesta manera realitzem el modelatge numèric per a diverses classes de *kernels* d'interacció i per a diferents tipus de models de trencament. L'algorisme creat es va validar comparant els resultats obtinguts amb resultats analítics, obtinguts per alguns col·laboradors, per *kernels* simètrics i asimètrics.

En el Capítol 3 estudiem la dinàmica de refredament d'un gas granular de

partícules allargades en 2D. Realitzem simulacions sobre l'evolució temporal d'un sistema de partícules toves fent servir un algorisme de dinàmica molecular. Per a sistemes poc dissipatius, hem trobat un procés de refredament homogeni on l'energia de translació disminueix de forma anàloga als gasos de partícules visco-elàstiques circulars. D'altra banda, per a partícules molt dissipatives es va observar un procés de refredament no homogeni on la disminució de l'energia cinètica de translació es ralentia de manera significativa. No obstant això, l'energia cinètica de rotació sempre decau seguint la predicció d'Haff per a l'estat de refredament homogeni de partícules inelàstiques. Hem trobat que la cinètica de refredament del sistema està controlada pels mecanismes de dissipació d'energia local (les col·lisions). No obstant això, trobem una forta influència de la geometria i elasticitat de les partícules en l'estructura dels *clusters* que es desenvolupen en els règims de refredament no homogeni. Els resultats numèrics obtinguts suggereixen que l'alta dissipació i l'anisotropia de les partícules indueixen la formació de *clusters* ordenats, que retarden la relaxació a un règim asimptòtic final.

Els resultats experimentals i numèrics dels efectes d'una descàrrega parcial sobre les propietats morfològiques i micro-mecàniques d'una sitja de partícules convexes i no esfèriques es mostren en el Capítol 4. La comparació de l'orientació de les partícules després de l'ompliment de la sitja i després de la descàrrega parcial revela canvis importants en l'orientació induït per el *shear*, la qual cosa afecta a la propagació de la tensió. Per a partícules allargades, el flux d'ompliment indueix un augment del desordre inicial, que comporta a la reducció de la propagació de la tensió vertical desenvolupada durant el procés de dipòsit, abans de la descàrrega parcial. En el cas de les partícules quadrades, el flux afavoreix l'alineació de les partícules amb les parets laterals de la sitja, la qual cosa provoca un comportament oposat al cas anterior. És a dir, s'indueix la transmissió de l'esforç en la direcció vertical. D'aquesta manera, per a les partícules allargades, el flux desenvolupat durant la descàrrega parcial de la sitja indueix la saturació de l'esforç amb la profunditat. Per contra, per als quadrats, el flux indueix l'obstaculització de la saturació de l'esforç amb la profunditat.

En el Capítol 5 examinem l'efecte d'una força d'atracció sobre les propi-

etats d'empaquetament de grans allargats. En dipòsits de varetes no-cohesives en 2D, la topologia de l'empaquetament està dominada principalment per la formació d'estructures ordenades alineades. Les partícules allargades tendeixen a alinear-se horitzontalment i la tensió es transmet, principalment, de dalt a baix, revelant una distribució asimètrica de la tensió local. No obstant això, per als dipòsits de partícules cohesives, la tendència a l'orientació horitzontal desapareix. Para partícules molt allargades amb fortes forces atractives es formen estructures molt desordenades, que es caracteritzen per una distribució de l'orientació que tendeix a un comportament uniforme quan s'incrementa el número de Bond. Com a resultat d'aquests canvis, la distribució de la pressió en els dipòsits canvia qualitativament. La part isòtropa de la tensió local augmenta notablement pel que fa a la part desviadora, la qual està relacionada amb la direcció de la gravetat. Per tant, la transmissió de la tensió lateral està dominada per l'augment del desordre i condueix ràpidament a la saturació de la pressió amb la profunditat.

En el Capítol 6 vam mostrar els resultats de la implementació d'un algorisme de dinàmica molecular per a un sistema de partícules esfèriques, que utilitza el poder de càlcul de les GPU. El nou algorisme híbrid CPU-GPU té en compte tots els graus de llibertat de les partícules, inclosa la representació en 3D de la rotació mitjançant *quaternions*. Para més versatilitat, la interacció entre les partícules es defineix mitjançant una força generalitzada, que representa les interaccions dissipatives i elàstiques. Els paràmetres d'interacció entre esferes dures es van adaptar per a la interacció entre esferes toves. Es va demostrar que l'algorisme desenvolupat compleix amb les lleis de la mecànica estadística mitjançant l'estudi del refredament homogeni d'un gas granular d'esferes amb rotació. Els resultats obtinguts concorden excel·lentment amb les teories de camp mitjà per a sistemes de baixa densitat de partícules esfèriques dures. Aquesta tècnica redueix dràsticament el temps de càlcul en comparació de les implementacions tradicionals sobre CPUs.

Chapter 1

Introduction

Granular Media are one of the most handled materials in industry and everyday life. As examples of granular media can be mentioned: kitchen salt, sugar, sand or grains of corn. In general, substances known as granular media (GM), or granular material, include things that are made up of many distinct grains. In the physics community, they are considered multi particles systems characterized by a loss of energy whenever particles interact [1].

Huge experimental and theoretical efforts have been made to understand the global behavior of granular media, in terms of their local particle-particle interactions. Nevertheless, despite the fact that granular media are often composed of grains with anisotropic shapes like rice, lentils or pills, most experimental and theoretical studies have concerned spherical particles.

One of the major problems, currently faced by computational modeling researchers, is the computational cost of the numerical algorithms, both in runtime and memory usage. Moreover, the era of Moore's law [2, 3] is practically over, and the velocity of new microprocessors is not growing as fast as in the last years. An irrefutable evidence is that the largest producers of microprocessors, Intel© Corporation and AMD© Inc., have stopped substantially increasing the clock speed of their processors and have chosen to increase the number of cores. In this framework, it is mandatory to continuously develop more and more efficient and realistic numerical tools for better describing natural and technological processes.

In this thesis, several numerical algorithms for modeling granular media

are introduced and discussed, in detail. All the presented results are published in indexed scientific journals or in preparation for submission.

1.1 Computational Physics

In mathematical modeling, to achieve analytical solutions is always desirable. However, in many cases mathematical equations do not have analytical solution or their resolution is not feasible from a practical point of view. In those cases is where numerical methods acquire greater relevance. However, its application is not limited to these cases. Thus nowadays, computational methods are essential tools for the study any kind of technological and natural issues.

Computational Physics is a branch of science devoted to study and implement numerical algorithms to solve physical problems, which may or not have an exact solution. Some researchers regard it as part of theoretical physics, while others consider it an intermediate branch between Experimental and Theoretical Physics. Besides simulating physical systems, more general numerical issues are object of study by this branch of science. Many of them could be considered part of pure mathematics. Such topics include, solving integro-differential equations, systems of differential equations as well as solving stochastic processes. Moreover, there are also a large number of applied areas.

In computational physics, the numerical methods can be divided into two main groups: deterministic and stochastic methods. A deterministic methods are Mathematical techniques based on the concept that future behavior can be predicted precisely from the past values of the data set. These methods ignore the existence of disturbances that may alter the data's future pattern. Contrary, nondeterministic methods refer to numerical algorithms that can exhibit different behaviors on different runs.

Monte Carlo methods are stochastic techniques based on the use of random number generator and probability distributions. They were introduced to investigate many different natural and applied issues [4]. Its applications can be found almost in all branches of science, from gambling to nuclear physics, and of course, granular media is not an exception.

Molecular dynamics is a computational method used to calculate the time dependent behavior of discrete systems. Using this approach, the movement of the particles is always governed by the equation of motion, and the particles interact through a given potential. This method was first introduced by Alder and Wainwright in 1950 [5, 6]. In contrast with Monte Carlo methods, *Molecular dynamics* is a deterministic method.

1.1.1 Monte Carlo method

Monte Carlo methods provide approximate solutions to a large number of mathematical and physical problems by performing statistical sampling experiments. Note that this method can be applied to processes with no probabilistic content at all, as well as to those with inherent probabilistic structure. John von Neumann, Stanislaw Ulam and Nicholas Metropolis are considered the fathers of the Montecarlo method. They introduced it while they were working on the *Manhattan Project* in Los Alamos National Laboratory, USA back in 1940s. It seems like MC was named "in homage" to the Monte Carlo Casino, because there was where Ulam's uncle often gambled away his money [7]. However, most of the authors say that the reason is that roulette is the simplest random number generator.

MC algorithms are especially helpful to simulate systems with many degrees of freedom, such as fluids, disordered materials, strongly coupled solids and cellular structures. They are widely used in mathematics [8–10], physics [11–16], materials science [17], robotics [18–20], medicine [21–26], as well to model phenomena with significant uncertainty in inputs, such as the calculation of risk in business [27–30].

Since MC relies on repeated *random* samplings to compute the results, it is perfectly suited for calculation on a computer. Among other numerical methods that rely on the evaluation of N -points in an D -dimensional space to produce approximate solutions, the Monte Carlo method has absolute error that decreases as $N^{-1/2}$ (under the central limit theorem [31]). However, in the absence of exploitable special structure all others have errors that decrease as $N^{-1/D}$ at best. This property gives the MC a considerable edge in compu-

tational efficiency as the system size, N , increases. Moreover, combinatorial settings also illustrate this fact especially well. Whereas the exact solution to a combinatorial problem with N elements often has a computational cost that increases exponentially with N , the Montecarlo method frequently provides an estimated solution with a tolerable error at a cost that increase no faster than a polynomial dependence of N [32].

Metropolis-Hastings method

The Metropolis-Hastings (MH) algorithm was developed by Metropolis *et al.* [33] in 1953 and generalized in 1970 by Hastings [34]. This method can draw samples from any probability distribution $P(x)$, requiring only that a function proportional to the density can be calculated. In statistics this function is known as *probability density function* or *pdf*.

Consider two configurations at time t and $t + 1$, each of which occurs with probability proportional to the Boltzmann factor. Then the transition probability reads as

$$\frac{P_t}{P_{t+1}} = \frac{e^{-\frac{E(t)}{kT}}}{e^{-\frac{E(t+1)}{kT}}} = e^{-\frac{E(t+1)-E(t)}{kT}} \quad (1.1)$$

where k is the Boltzmann constant and T is the temperature of the system.

In their paper Metropolis et al. [34], noted that we can achieve the transition probability of Eq.1.1 in a simulation by proceeding as follows

1. Starting from a configuration with known energy $E(t)$, make a random change in the configuration
2. Calculate the potential energy $E(t + 1)$, for the new probable state of the system and calculate $\Delta E = E(t + 1) - E(t)$
3. If $\Delta E \leq 0$ the new state is accepted
4. If $\Delta E > 0$ a random number α between 0 and 1 is generated. If $\alpha < e^{-\frac{\Delta E}{kT}}$ the new state is accepted, otherwise, the new state is refused and the current state is kept.

If we follow these rules, then we will sample on the phase space, all possible configurations with probability proportional to the Boltzmann factor. That is consistent with the theory of equilibrium statistical mechanics. We can compute average properties by summing them along the path we follow through possible configurations. The ergodic hypothesis [35–38] states that an ensemble average obtained by MC simulation is equivalent to an average time obtained through a simulation of molecular dynamics in the limit of an adequate sampling (MC) and sufficient time (MD). In physics and thermodynamics, the ergodic hypothesis says that, over long periods of time, the time spent by a particle in some region of the phase space of micro-states with the same energy is proportional to the volume of this region, *i.e.*, that all accessible micro-states are equal-probable over a long period of time.

In the next chapter, we describe in details an example of MC called Direct Simulation Monte Carlo (DSMC). The DSMC method was proposed by Graeme Bird [39] and uses probabilistic (Monte Carlo) simulations to solve the Boltzmann equation. In our case, we examine the solution of the integro-differential equation that describe the collision-induced fragmentation of a granular gas.

1.1.2 Molecular Dynamics

Molecular systems usually consist of a large number of interacting particles whose typical size ranges from micrometers to nanometers. Very often, it is impossible to describe such complex systems analytically, thus, numerical methods are specially suited.

Molecular dynamic (MD) is a method commonly used to determine macroscopic thermodynamic properties of molecular systems. It was first introduced by Alder and Wainwright in the 1950's to study the interactions of hard spheres [5, 6]. The next major advance was in 1964, when Rahman carried out the first simulation using a realistic potential for liquid Argon [40]. In 1967, Verlet calculated the full phase diagram of Argon, and computed correlation functions testing several theories of the liquid state [41, 42].

MD describes deterministically the physical movements of atoms and molecules. That's why, it either requires the definition of a potential function, or a de-

scription of the terms by which the particles in the simulation will interact. The force acting on a particle can be divided into two classes, short-range and long-range forces. Short-range forces are the actions exerted by objects that are near to the particle and that after a certain distance threshold becomes zero, such as particles collisions. Long-range forces is said of those forces that do not become equal to zero within any distance. Classic long-range forces are gravity or external electrical fields.

The application of molecular dynamics algorithms to macroscopic systems is called by the engineering community Discrete Elements Simulations (DEM). This is generally distinguished by its inclusion of rotational degrees-of-freedom as well as state-full contact and often complicated particle shape. Note that the physics community does not make distinctions between molecular dynamics (MD) and Discrete Elements Simulations (DEM).

Molecular dynamics simulation of granular system

Event-driven

In dilute systems, where the typical collision time is much shorter than the mean time between successive collisions, particles are rarely in contact with more than one particle. Hence, most of the time particles propagate along a ballistic trajectory only interrupted by collisions with other particles. Therefore, the pairwise collisions of particles can be considered as instantaneous *events*, which may be treated separately [43].

In these conditions, after the collision of particles i and j , their final velocities (\vec{v}' and $\vec{\omega}'$) can be written as a function of their values (\vec{v} and $\vec{\omega}$) just before the collision [44–48]. Considering spherical particles of radius R , mass m , linear velocity \vec{v} , angular velocity $\vec{\omega}$ and momentum of inertia I , this functions can be written as [43]:

$$\begin{aligned}
 \vec{v}'_i &= \vec{v}_i - \frac{1+\epsilon_n}{2} v_{ij}^n + \frac{\tilde{I}(\epsilon_t-1)}{2(I+1)} v_{ij}^t, \\
 \vec{v}'_j &= \vec{v}_j + \frac{1+\epsilon_n}{2} v_{ij}^n + \frac{\tilde{I}(\epsilon_t-1)}{2(I+1)} v_{ij}^t, \\
 \vec{\omega}'_i &= \vec{\omega}_i - \frac{\epsilon_t-1}{2R(I+1)} (e_{ij}^n \times v_{ij}^t), \\
 \vec{\omega}'_j &= \vec{\omega}_j + \frac{\epsilon_t-1}{2R(I+1)} (e_{ij}^n \times v_{ij}^t)
 \end{aligned} \tag{1.2}$$

where $\vec{v}_{ij} = \vec{v}_i - \vec{v}_j$ is the relative velocity, with components in normal (v_{ij}^n) and tangential directions (v_{ij}^t). \vec{e} represents a unit vector pointing along the line of centers of mass from particle i to particle j and $\tilde{I} = I/mR^2$ is the reduced momentum of inertia. The normal restitution coefficient ϵ_n varies between 1 and 0, $\epsilon_n = 1$ means no dissipation (elastic system) and $\epsilon_n = 0$ means full dissipation (perfectly inelastic system). The tangential restitution coefficient $\epsilon_t = 1$ goes from -1 (smooth particles) to $+1$ (rough particles), corresponding to 0 the maximum coupling. The strength of the coupling between rotational and translational motion is connected to $1 + \epsilon_t$ [49–52].

Modeling event-driven MD, only one particle-particle interaction is considered each step of time. Moreover, the interaction takes an infinitesimal time. On the time elapsed between two collisions, the particles move following known ballistic trajectories. A general outline of the algorithm could be

1. Initialize positions \vec{r}_i , velocities \vec{v}_i and angular velocities $\vec{\omega}_i$ (if considered) for each particle i ($i = 1, \dots, N$).
2. Calculate the time t^* when the next collision occur. For equal-sized spheres of radius R

$$t^* \equiv \min(|\vec{r}_i(t_{ij}) - \vec{r}_j(t_{ij})| = 2R; i, j = 1, \dots, N) \quad (1.3)$$

3. Determine the position of all particles at $t = t^*$

$$\vec{r}_i = \vec{r}_i + (t^* - t)\vec{v}_i + F_i^{ext} \quad (1.4)$$

where F_i^{ext} are external long-range forces acting on particle i , as gravity.

4. Compute the new velocities accordingly to Equations 1.2.
5. Update the simulation time $t = t^*$.
6. Back to step 2 until the stop condition is satisfied.

The event-driven method is specially efficient for the study of dilute, non-disperse, hard spheres materials [43, 52–55], but its application is not limited to those systems [56–60]. In the presented algorithm, a constant restitution coefficient is considered, some authors consider that this is not very realistic [61, 62] and that the restitution coefficient should depend on the relative velocity [46, 63–69].

Force-based molecular dynamics

In force-based molecular dynamics the forces that govern the motion of the particles are determined from the (small) mutual deformation of the particles. That's why these methods are more appropriated for describing the micro-mechanic properties of dense granular media and systems with complicated particles shapes.

The general idea of molecular dynamics simulation is to numerically solve the Newton's equation of motion for all particles i ($i = 1, \dots, N$)

$$\sum_{j=1}^N \vec{F}_{ij} + \vec{F}_e = m_i \ddot{\vec{r}}_i \quad (1.5)$$

$$\sum_{j=1}^N L_{ij} = I_i \ddot{\theta}_i \quad (1.6)$$

where m_i is the mass of the particle, I_i is its moment of inertia and \vec{r}_i and θ_i are the particle's position and orientation respectively. \vec{F}_e represents an external field, \vec{F}_{ij} corresponds to the force exerted by particle j on particle i and L_{ij} the torque related with the force \vec{F}_{ij} , which points in the direction perpendicular to the plane in which the particles displace. The total force and the total torque acting on particle i are given as sums of the pair-wise interaction of particle i with its contacting neighbors. Accordingly, the grains' trajectories will be determined by the nature of the collisional forces.

When two particles come in contact they deform inelastically. In force-based molecular dynamics, rather than describing the actual grain deformations, the most common strategy consists in keeping the *shape* of the particles and allow them to overlap. Hence, the interaction force and torque are determined in terms of the overlapping distance or area [43, 70–75].

The total force between the two grains, can be decomposed in normal F_{ij}^N and tangential F_{ij}^T components, to the interface defined by the contact points of the two particles when they overlap

$$\vec{F}_{ij} = F_{ij}^N \cdot \vec{n} + F_{ij}^T \cdot \vec{t} \quad (1.7)$$

\vec{n} and \vec{t} are the vectors in normal and tangential direction of the common surface.

The normal component of the force contains an elastic contribution, proportional to the pair overlapping distance or area, and a dissipative contribution $F_{ij}^N = F_e^N + F_v^N$. The tangential component of the interaction force is also characterized by an elastic and a dissipative contribution $F_{ij}^T = F_e^T + F_v^T$, and obeys the Coulomb constraint [76], $F_{ij}^T \leq \mu |F_{ij}^N|$, where μ stands for the static friction coefficient

$$F_{ij}^T = -\min(F_{ij}^T, \mu F_{ij}^N) \quad (1.8)$$

In general, for circular or spherical particles it is possible to derive analytic expressions for F_{ij}^N and F_{ij}^T as a function of the overlapping distance. However, for particles of irregular shape this is not feasible and it is computed numerically [43, 71–75, 77, 78].

In Figure 1.1 the interaction of two particles is illustrated. In the case of interacting disc (Figure 1.1a) all authors agree to apply the force in the center of mass of the overlap area, while for non-circular particles –where the overlap area forms more complex shapes– different strategies are used [74, 75, 77, 78]. In the case shown in Figure 1.1b the force is applied in the middle of the line connecting the farthest points of the common area.

Integration methods

Numerical integration of ordinary differential equations (ODE) is a frequent task in numerical analysis of physical and engineering issues [79–88]. As examples one can mention the simple Euler method (also known as Forward Euler) [80, 81], Backward Euler method [82], Leapfrog integration [83], Verlet integration [41, 42, 84], Runge-Kutta methods [84–86], or the Predictor-Corrector method [86–89]. In the next sections, Euler’s method, Verlet integration and the Predictor-Corrector method are explained in detail.

An important point when solving ODE is that a differential equation $y(t)$ of order n can be represented as a first order ODE in more than one variable by introducing $n - 1$ further variables ($y'(t), y''(t), \dots, y^{(n)}(t)$) and formulating n

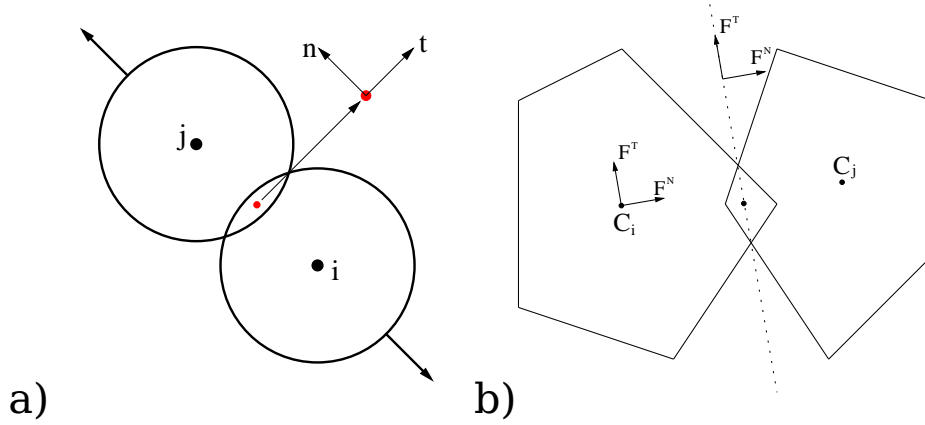


Figure 1.1: Interaction of two particles. The normal force is parallel to the line that connect the center of both particles and the tangential force is perpendicular to this imaginary line. a) For interacting disc, the force is applied in the center of mass of the overlap area. b) When non-regular particles are modeled different points are used to apply the force, in this case the center of the line connecting the farthest vertex of the overlap area.

first-order equations in these new variables. For that reason, next epigraphs focus on integration methods of first order differential equations.

Euler integration method

Euler's method is the most basic first-order numerical method for solving ODEs [80]. For using this approach two things are necessary, the differential equation and the value of the function at some point

$$\frac{dy}{dt} = f(t, y), \quad y(t_0) = y_0 \quad (1.9)$$

The method consist in approximate the solution of Equation 1.9 using the linear approximation of y around the point $P_0(t_0, y(t_0))$ (the first two terms of the Taylor expansion [90])

$$y_{n+1} = y_n + hf(t_n, y_n) \quad (1.10)$$

where $h = (t_{n+1} - t_n)$ is known as the integration step. Equation 1.10 is calculated iteratively until $t_n < t_f$. The algorithm in pseudocode is shown in Algorithm 1.

```
 $y(t_0) \leftarrow y_0$   
 $n := 0$   
while  $t_n < t_f$  do  
     $t_{n+1} := t_n + h$   
     $y_{n+1} := y_n + hf(t_n, y_n)$   
     $n := n + 1$   
end while
```

Algorithm 1: Pseudocode of Euler’s method. It is the simplest and least accurate first-order method for solving ODEs. The derivate y_{n+1} at each point t_{n+1} is calculated using the derivate y_n at the previous point t_n .

The Euler’s method is unsymmetrical, it advances the solution through an interval h , but uses derivative information only at the beginning of the interval. That means that the step’s error is of the order of $O(h^2)$ [91]. A solution to minimize the error is decreasing h , however, this action increase the number of necessaries steps and therefore the computational cost.

This method is not recommended for most problems, mainly because it is not accurate when compared to other methods running at equivalent step-size and neither it is very stable [91].

Verlet integration method

Verlet integration was first used by Carl Störmer to compute the trajectories of particles moving in a magnetic field (hence it is also called Störmer’s method) [91] and was popularized in molecular dynamics by French physicist Loup Verlet in 1967 [41, 42]. It is a numerical method used to integrate Newton’s equations of motion (Equations 1.5 and 3.1) and frequently applied to calculate trajectories of particles in molecular dynamics simulations and computer graphics. The basic idea is to write two third-order Taylor expansions for the positions r and orientations θ , one forward and one backward in time.

A related algorithm, and more commonly used in molecular dynamics simulations, is the Velocity Verlet algorithm, the basic implementation scheme of this method is presented in Algorithm 2, for more details about the algorithm see the section Appendix in [92].

```

 $a(t_0) \leftarrow 0$ 
 $v(t_0) \leftarrow v_0$ 
 $t := 0$ 
while  $t < t_f$  do
   $v(t + \frac{1}{2}\Delta t) = v(t) + a(t)\frac{1}{2}\Delta t$ 
   $x(t + \Delta t) = x(t) + v(t + \frac{1}{2}\Delta t)\Delta t$ 
  Derive  $a(t + \Delta t)$  from the forces equations using  $x(t + \Delta t)$ 
   $v(t + \Delta t) = v(t + \frac{1}{2}\Delta t) + a(t + \Delta t)\frac{1}{2}\Delta t$ 
   $t := t + \Delta t$ 
end while

```

Algorithm 2: Pseudocode of Velocity Verlet method. It is a second-order method for solving ODEs, developed for integrating the Newton's equations of motion and with application in physics and computational graphics. An intermediate integration is made at the mid-point between t_n and $t_{n+\Delta t}$. The step size is called Δt instead of h

The Verlet integrator offers greater stability, as well as time-reversibility and preservation of the symplectic form on phase space, at no significant additional cost over the Euler's method. Nevertheless, the error is still of the order of $O(\Delta t^2)$. The disadvantage of this method respect to Euler algorithm consist in that, as it is calculated in three stages, it is more computationally expensive, in both time and memory consuming.

Predictor-Corrector integration method

Predictor-corrector method consists of an implicit method of good accuracy (corrector equation) and an explicit method (predictor equation) that provides an initial approximation for the iterative process and the implicit method. Different implementations has been developed, those more often used in molecular dynamics are due to C.W. Gear [87], and consists of three steps:

1. *Predictor*. From the positions and their derivatives up to order n in t are obtained the same quantities at $t + \Delta t$ by Taylor expansions. Among these quantities are accelerations a . The predictor step for a fourth order Gear

algorithm can be written in matrix form [44]

$$\begin{pmatrix} r_0^p(t + \Delta t) \\ r_1^p(t + \Delta t) \\ r_2^p(t + \Delta t) \\ r_3^p(t + \Delta t) \end{pmatrix} = \begin{pmatrix} 1 & 1 & 1 & 1 \\ 0 & 1 & 2 & 3 \\ 0 & 0 & 1 & 3 \\ 0 & 0 & 0 & 1 \end{pmatrix} \begin{pmatrix} r_0(t) \\ r_1(t) \\ r_2(t) \\ r_3(t) \end{pmatrix}$$

2. *Forces.* With the positions and the velocities predicted, forces are calculated according to the contact model, and then the accelerations. The difference between predicted accelerations and the ones calculated in these step give the error of the method

$$\Delta r_2(t + \Delta t) = r_2^c(t + \Delta t) - r_2^p(t + \Delta t)$$

3. *Corrector.* This error signal ϵ is used to correct positions and their derivatives. The coefficients of proportionality are determined to maximize the stability of the method. In matrix form

$$\begin{pmatrix} r_0^c(t + \Delta t) \\ r_1^c(t + \Delta t) \\ r_2^c(t + \Delta t) \\ r_3^c(t + \Delta t) \end{pmatrix} = \begin{pmatrix} r_0^p(t + \Delta t) \\ r_1^p(t + \Delta t) \\ r_2^p(t + \Delta t) \\ r_3^p(t + \Delta t) \end{pmatrix} \begin{pmatrix} c_0 \\ c_1 \\ c_2 \\ c_3 \end{pmatrix} \Delta r_2(t + \Delta t)$$

In [87], C.W. Geard discusses the best choice for the corrector coefficients c_i , which depends on how many derivatives of r_i are used.

The main advantage of the predictor-corrector algorithm is its high accuracy. However, it is harder to implement and more time consuming (requires additional calculations) and, numerically, is unstable against relatively big integration steps [93].

Boundary conditions

In general the behavior of granular systems are strongly influenced by the interaction of the grains with the system boundaries, *i.e.*, the interaction with the container or the surface on which the system lays. As examples can be

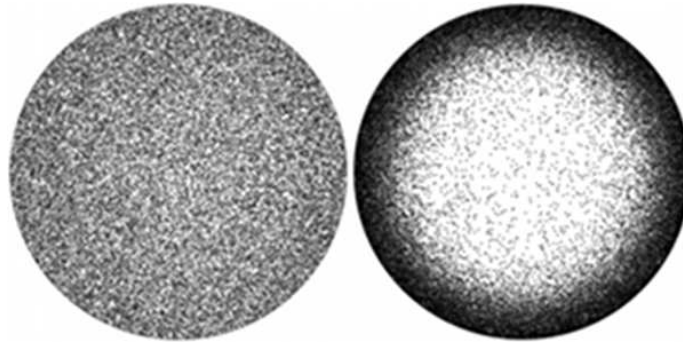


Figure 1.2: A dilute granular system evolves in a circular container in the absence of external forces. Initialized homogeneously (left), the particles accumulate close to the reflecting wall after a long time (right). Taken from [43].

mentioned the convective motion of granular material in vibrating containers, the formation of density waves in pipes, the motion of granular materials on conveyors, and the clogging of hoppers. In these cases, the interaction with the container has to be examined carefully [43]. Hence, depending on the applications the implemented boundaries should be different. The most used types are reflecting boundaries, periodic boundary conditions and heated walls. In the next section the first and second methods are explained. Moreover, some of their physical implications are discussed.

Reflecting Boundaries

There are two ways of applying reflecting boundary conditions: the first one, when particles collide with the system walls its velocity component reverts (conservatively or non-conservatively) perpendicular to the wall, whereas the velocity component parallel to the wall remains invariant. The second method is to build walls made of particles that follow the same interaction rules than "internal particles" obey, varying –if necessary– the particle size. Such walls are very simple to implement into the MD simulation due to no extra interaction rules are needed. The interaction of the particles with the wall are computed in the same way that a particle-particle interaction.

Molecular dynamics simulations using reflecting boundaries shows strong system size effect. For instance, after some time the particles clusterize near

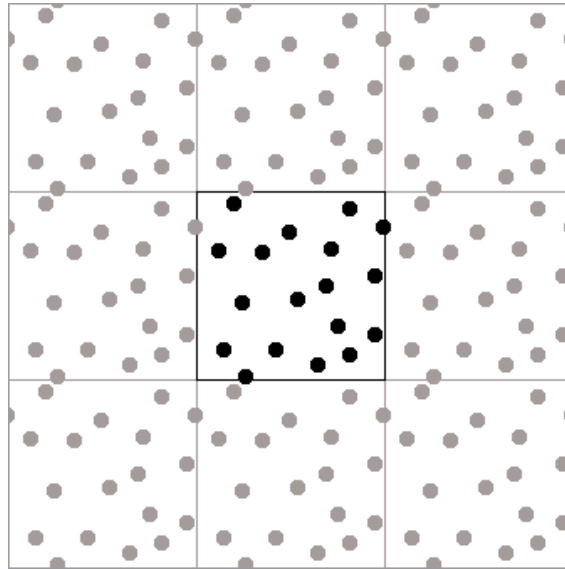


Figure 1.3: The main volume of the simulation (in black color) is repeated in all directions (drawn in gray), simulating an infinite system from a finite volume.

to the walls (see Figure 1.2). This happens even in the absence of external forces such as gravity and it is caused by an enhanced collision frequency close to the walls. Furthermore, at the borders the typical relative velocity is larger than in the bulk of the system. On average, particles located near the system boundaries collide more times and with higher relative velocities than particles located close to the walls. It leads to a faster temperature decay in the vicinity of reflecting walls and consequently, decreasing pressure and increasing particle density [43, 45].

Periodic Boundary Conditions

Surface effects can be ignored for all system sizes if we use periodic boundary conditions (PBC). In PBC, when a particle reaches the limits of the main box it returns through the opposite side. PBC allows the simulation to proceed as if the primary volume was surrounded by identical copies of itself (Figure 1.3). Any particle i at position r_i in the primary volume represents an infinite set of particles located at

$$\vec{r}_i^{k,l,m} = \vec{r}_i + k\vec{X} + l\vec{Y} + m\vec{Z} \quad (1.11)$$

where \vec{X} , \vec{Y} and \vec{Z} are the edge vectors of the primary volume and k , l and m are integer numbers taken values from $-\infty$ to ∞ . In practice the this set is reduced to $\{-1, 0, 1\}$.

Implementing periodic boundary conditions there are some important details to take into account:

1. Particles not only interact with those located in its volume, but also with their periodic images.
2. A particle i can only interact with the closest image of particle j , *i.e.*, two particles i and j can not interact more than once in a single time step.
3. The distance between two particles i and j is the smallest distance between i and all images of j .

Moreover, it is important to remark that using PBC the studied system is thought to be much larger than the simulated number of particles. In general, the system size effects are smoothed and better controlled but not totally diminished.

1.2 Scientific programming

General Overview

One of the major problems, currently faced by computational modeling researchers, is the computational cost of the numerical algorithms, both in runtime and memory usage. Moreover, the velocity of the new microprocessors is not growing as fast as in the last years. An irrefutable evidence of this is that the largest producers of microprocessors, Intel© Corporation and AMD© Inc., have stopped substantially increasing the clock speed of their processors and have chosen to increase the number of cores.

With the introduction of multi-cores processors, computer programmers have the option to develop their applications to run in parallel on their personal computers [94–96]. However, the use of multiple cores, specially when

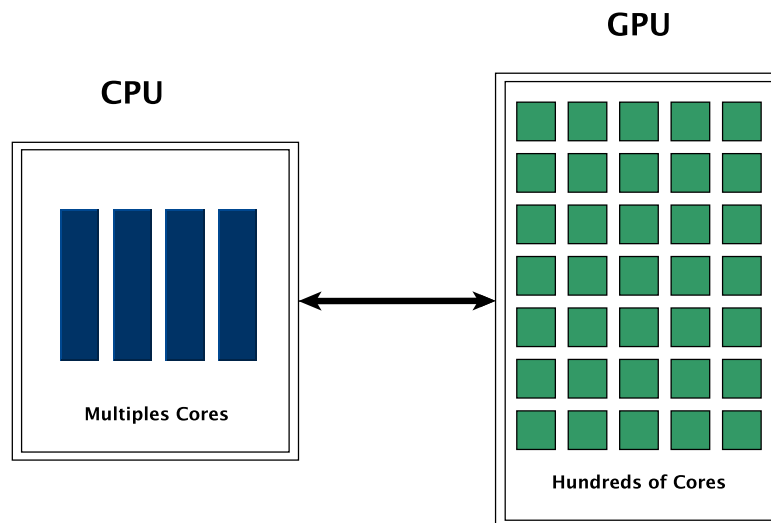


Figure 1.4: Heterogeneous programming model. The less expensive operations will be executed on the CPU, whilst the more time consuming will be executed on a GPU.

the independent cores share the pathway to the system memory, leads to the advent of the *memory wall* problem, given by the increasing gap between processor and memory speeds. In numerical modeling, where a lot of matrix and vector operations are required, it is relative simple to reach the point when this difference becomes a bottleneck. Furthermore, developing a program to take advantage of multi-cores processors is a complicated task, and in most cases it does not guaranty a linear increase of the performance with the number of used cores.

In todays scenario, general-purpose computation on graphics processing units (GPGPU) [97–99] has become a serious alternative for parallel computing [100] on personal computers. The methodology that follows this technology is based on the combined use of a CPU (Central Processing Unit) and GPU co-processing in a heterogeneous system, where the sequential part of the program runs on the CPU and the part that is more computational expensive is accelerated in the GPU (see Figure 1.4).

Although using graphical cards for general purpose computing is currently reaching its peak, research in this area was also made several years ago [101–106]. One of the reasons for using GPUs to perform some especial tasks is

that CPUs are designed for high performance on sequential operations, while GPUs are optimized for the high parallelism of vertex and fragment processing [107].

Nowadays, to develop numerical applications on graphics cards there are three choices NVIDIA© CUDA™, AMD© APP and OpenCL™

- *CUDA* is NVIDIA's parallel computing architecture, giving to developers the necessary tools to perform GPGPU on NVIDIA's graphic cards [108].
- *AMD APP* technology is a set of advanced hardware and software technologies that enable AMD graphics processing cores, working in concert with the system's cores, to accelerate many applications beyond just graphics using ATI graphic cards [109].
- *OpenCL (Open Computing Language)* is the first open, royalty-free standard for general-purpose parallel programming of heterogeneous systems. OpenCL provides a uniform programming environment for software developers to write efficient, portable code for high-performance compute servers [110].

Our research, in chapter 6 concerns NVIDIA CUDA, mainly because the available GPU-hardware was NVIDIA's graphic cards.

GPGPU with CUDA

In November 2006, NVIDIA© release the GeForce 8800 GTX, the first GPU built with NVIDIA's CUDA Architecture. This architecture included several new components designed strictly for GPU computing, and aimed to alleviate many of the limitations that prevented previous graphics processors from being legitimately useful for general-purpose computation. Because NVIDIA intended this new family of graphics processors to be used for GPGPU, the processor's ALUs (arithmetic logic unit) were built to comply with IEEE requirements for single-precision floating-point arithmetic and were designed to use an instruction set tailored for general computation rather than specifically for graphics [99].



Figure 1.5: CPU and GPU Architecture. GPU devotes more transistors to data processing. Taken from [111].

To reach the maximum number of developers, NVIDIA took industry-standard C and added a relatively small number of keywords in order to harness some of the special features of the CUDA Architecture. A few months after the launch of its graphic card, NVIDIA made public a compiler for this language, CUDA C, which became the first language specifically designed by a GPU company to facilitate general-purpose computing on GPUs [99]. Nowadays there are third party wrappers for many programming language, like: Python, Perl, Fortran, Java, Ruby, MATLAB, and native support exists in Mathematica.

The reason behind the difference in performance of floating-point capability between the CPU and the GPU is that the GPU is specialized for compute-intensive, highly parallel computation. GPU are designed such that more transistors are devoted to data processing rather than data caching and flow control (see Figure 1.5). The GPU is especially well-suited to address problems that can be expressed as data-parallel computations with high arithmetic intensity –the ratio of arithmetic operations to memory operations. Because the same program is executed for each data element, there is a lower requirement for sophisticated flow control, and since it is executed on many data elements and has high arithmetic intensity, the memory access latency can be hidden with calculations instead of big data caches [111]. The evolution of the number of floating-point operations per second (FLOP) that a processor can do is shown in Figure 1.6.

To develop CUDA C applications it is indispensable to have a CUDA-enable

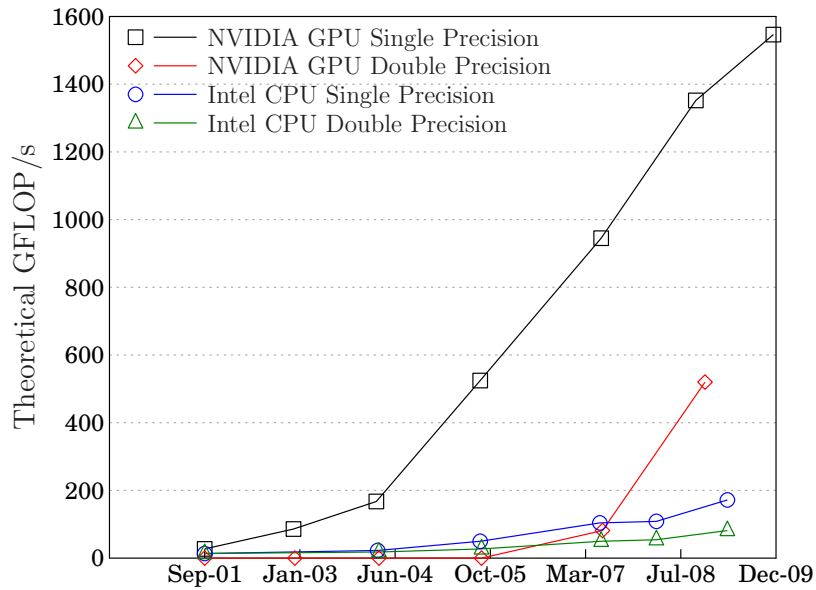


Figure 1.6: Evolution of the floating-point operations per second performed by processors in last years. Data extracted from [111].

graphic processor (generally an NVIDIA graphic card), an NVIDIA developer device driver, a CUDA development toolkit and a standard C compiler. The CUDA-enable graphics cards are listed in the *CUDA GPUs Web Page* [112]. The necessary tools from NVIDIA can be downloaded from the *NVIDIA GPU Computing SDK Web Page* [113] for different computing platforms. Standards C compilers exists for most platforms.

As illustrated on Figure 1.7, in a program developed with CUDA there are a set of functions that run on the CPU and others that do it on a CUDA-enable graphic processor, the *host* and the *device* in CUDA's argot, respectively. The operations that run into the CPU are the less time consuming, or those ones that, by their nature, can not be parallelized. The CUDA functions are known as *kernels*.

Besides the expected applications on computer graphics, softwares that take benefit of the computing capabilities of CUDA have been developed in many different areas. In oil and natural resource exploration scientists used to work with very small sample sets, and low resolutions in order to find possible sources of oil [114–117]. Because the ground reconstruction algorithms

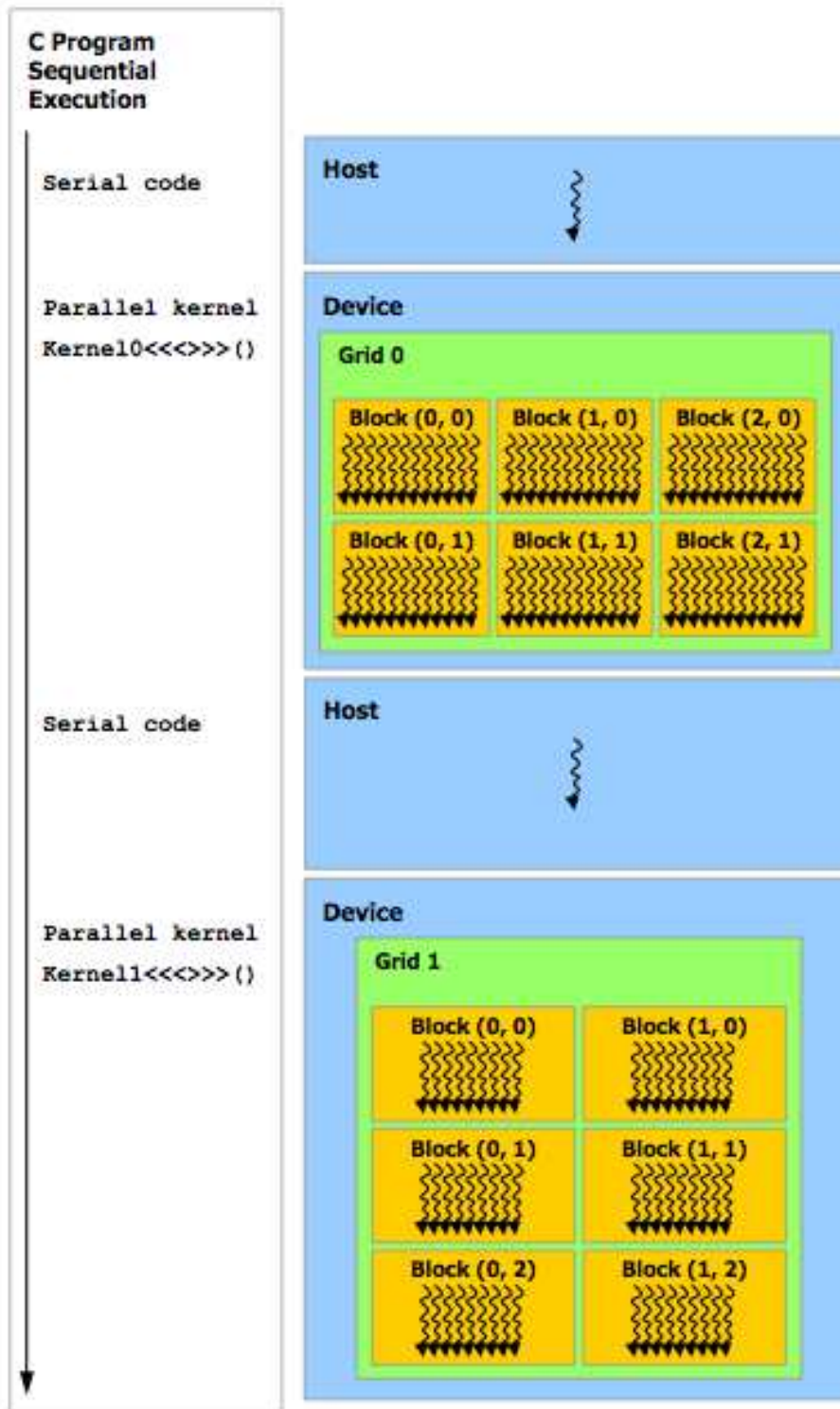


Figure 1.7: CUDA Heterogeneous Programming Model. Some operations will be executed on the CPU (Host) and the more expensive operations on the GPU (Device). Taken from [111].

are highly parallel, CUDA is perfectly suited to this type of challenge. For medical imaging processing CUDA is a significant advancement [118–120]. Using CUDA, MRI machines can now compute images faster than ever possible before, and for a lower price. Before CUDA, it used to take an entire day to make a diagnosis of breast cancer and now this can take only 30 minutes.

In chapter 6 we describe in detail the implementation of a hybrid CPU-GPU molecular dynamics algorithm of dissipative spheres including rotation. Starting from the crude CUDA-particles example we have developed a very accurate algorithm for examining a realistic granular system.

Chapter 2

Collision induced fragmentation: a simple numerical algorithm

Fragmentation processes are of significant scientific interest and have enormous technological impact. These phenomena usually arise in many natural and technological processes, such as granulate processing [121], shattering of solid and shell-like objects [122–124], meteorite [125], mineral grinding [126], liquid droplets [127] and atomic nuclei [128]. In some cases fragmentation can be regarded as linear. That is the case when the process dynamics is only sensitive particle properties (such as size) and it does not depend significantly on particle interaction [129]. Contrary, when the interaction between grains plays a significant role the evolution of the granular system is intrinsically non-linear.

Most of the theoretical studies on fragmentation have been carried out within the framework of Smoluchowski-like equations [129–134], where particle fragmentation is determined by impacts of pairs of particles. Here, the role of particle velocity at impact is neglected, and the evolution of the distribution of particle sizes have been described. These studies have led to explicit results and have addressed the emergence and properties of dynamic scaling regimes [129–137]. Although less explored, the effect of particle velocity at collision and its relevance in fragmentation has also been addressed recently [137–139].

McGrady and Ziff realized that under special circumstances a fragmenting

system can give rise to a singularity the so-called shattering transition [130]. This refers to a finite time, t_c , at which a finite fraction of the system mass is carried by an infinite number of particles of infinitesimal size, which can be regarded as dust [130, 132–134]. This transition shares close analogies with the reverse process of gelation in aggregation kinetics, which has also been analyzed in the context of the Smoluchowski equation where aggregation arises as a result of two particle interactions [140–142]. The particular details of the collision-induced fragmentation process may lead to different types of shattering transitions, which may resemble first or second-order non-equilibrium phase transitions [133, 134]. Specifically, at the transition either the entire mass of the system is instantly transformed into dust or the dust mass gradually increases once the shattering transition occurred.

Because of its complexity, explicit solutions of generic non-linear fragmentation equations are generally not accessible. Hence, in generic cases a detailed study of the dynamics of fragmenting systems requires the use of numerical tools. To this end, we have adapted the Direct Simulation Monte Carlo (DSMC) technique, which has been widely used in the context of rarefied gases [143] and granular gases [144, 145], to the study of non-linear fragmenting systems.

2.1 Mean Field Theory

Collision-induced fragmentation can be described at the mean field level by the Smoluchowski fragmentation equation of the mass density $c(x, t)$ as

$$\partial c(x, t)/\partial t = -c(x, t) \int_0^\infty dy K(x, y) c(y, t) + \int_x^\infty dy \int_0^\infty dz b(x|y) K(y, z) c(y, t) c(z, t) \quad (2.1)$$

which assumes binary collisions and the kernel $K(x, y)$ describes the interaction rate of pairs of particles $[x; y]$. Equation (2.1) is composed of a loss (first) and a gain (second) term [131]. In the gain term, $b(x|y)$ represents a conditional probability which describes the distribution of outgoing fragments of mass x , given that a particle of mass y breaks [130, 131]. Here, one may distinguish between *deterministic* kinetics [131, 133], where a particle breaks into two equal fragments, hence $b(x|y) = 2\delta(x - y/2)$, and *stochastic* fragmentation

processes, where a fragment of random mass x breaks off from a particle of mass y . As mass is conserved in a single breakup event, the outgoing fragment distribution has to obey the homogeneity requirement, of $b(x|y) = y^{-1}b(\frac{x}{y})$. For simplicity, the standard form $b(s) = (\beta + 2)s^\beta$ is adopted and it obeys

$$\int_0^y dx x b(x|y) = y, \quad \bar{N} = \int_0^y dx b(x|y) = \frac{\beta+2}{\beta+1} \quad (2.2)$$

where \bar{N} is the mean number of outgoing fragments, which satisfies $\bar{N} \geq 2$, and implies $-1 < \beta \leq 0$. Binary breakup corresponds to $\beta = 0$.

The size dependence of the collision kernels depends on the physical processes underlying particle interactions. A variety of collision kernels, $K(x, y)$, has been proposed in applications of the non-linear Smoluchowski equation [140, 141, 146]. Because of their physical motivation and mathematical simplicity, most kernels have a sum-product form, such as

$$K(x, y) = 1, x^p + y^p, (xy)^p, x^p y^q + x^q y^p \quad (2.3)$$

In Equation (2.1), the kernel $K(x, y)$ may also contain the probability that breakage indeed occurs, expressed as $\bar{p}(x, y)$. Although in general, it will depend on particles' properties, if we can assume it as a constant we can already identify three classes of fragmentation kinetics depending on whether particle x or y breaks: (i) *symmetric breakage*, where a randomly chosen particle of the interacting pair (x, y) breaks [131, 133], and where $\bar{p}(x, y) = 1$; (ii) *L-breakage*, where the larger particle breaks, hence $\bar{p}(x, y) = \theta(x - y)$; and (iii) *S-breakage*, where the smaller particle breaks and $\bar{p}(x, y) = \theta(y - x)$; $\theta(x)$ stands for the unit step function. The general expression, Eq.(2.1) reduces for *L-breakage* and *S-breakage* to

$$\begin{aligned} \frac{\partial c(x, t)}{\partial t} &= -c(x) \int_0^\infty dy K(x, y) \theta(x - y) c(y) + \int_x^\infty dy \int_0^\infty dz b(x|y) K(y, z) \theta(y - z) c(y) c(z) \\ \frac{\partial c(x, t)}{\partial t} &= -c(x) \int_0^\infty dy K(x, y) \theta(y - x) c(y) + \int_x^\infty dy \int_0^\infty dz b(x|y) K(y, z) \theta(z - y) c(y) c(z) \end{aligned} \quad (2.4)$$

respectively.

2.2 Direct Simulation Monte Carlo Algorithm

Due to the non-linear character of the Smoluchowski fragmentation equation, it is useful to develop a numerical scheme which can explore efficiently the

main features of fragmentation kinetics. To this end, we have developed a numerical approach which follows the basic idea of Direct Simulation Monte Carlo (DSMC) technique, introduced by Bird to directly simulate the Boltzmann equation [143], and which has been extended to study other systems, such as granular gases [144]. The general idea underlying the approach is easily generalized to other kinetic equations.

Instead of solving Equation (2.1) numerically, we follow its temporal evolution through a stochastic sampling of the fragmentation process. We represent the fragmentation system by N particles with variable masses. These particles, however, do not correspond to real particles, they rather represent the continuum distribution which evolves according to the fragmentation equation. We follow the basic scheme in DSMC and fix a time step Δt_0 , smaller than the characteristic relaxation time of the kinetic equation. We then take a pair of particles at random, i and j with masses x_i and x_j respectively, and make them fragment with a probability

$$P_{coll}(i, j) = \frac{w_{ij}}{\sum_{n=1}^N \sum_{m=1}^{N-1} w_{nm}} \quad (2.5)$$

where we define the fragmentation frequency

$$w_{ij} \equiv K(x_i, y_j) \quad (2.6)$$

Following DSMC, we avoid the expensive calculation of the denominator by estimating the largest fragmentation frequency, w_{max} , and accept fragmentation events with a probability $P_{coll}(i, j) = w_{ij}/w_{max}$. One can also compute the number of pairs that must be sampled during Δt_0 , since the number of colliding pairs is fixed by the fragmentation frequency

$$M_{coll} = N^2 \langle w \rangle \Delta t_0 \quad (2.7)$$

where $\langle w \rangle$ stands for the averaged fragmentation frequency during the corresponding time interval. In order to maintain the proper fragmentation probability, we must then sample $M_{sample} = N^2 w_{max} \Delta t_0$ pairs. For the particular choice $\Delta t_0 = 1/N^2 w_{max}$, it is enough to increment the time by an amount Δt_0 after each attempt to fragment a pair of particles.

Instead of using a fixed time increment, it is possible to use the previous discussion considering that to observe a collision one needs to try to fragment $M_{sample} = w_{max}/\langle w \rangle$ pairs. Hence, $w_{max}/\langle w \rangle$ trials need to be carried out before a pair is fragmented, which corresponds to a fragmentation probability of

$$P(w) = \frac{w}{\frac{N(N-1)}{2}\langle w \rangle/w_{max}} \quad (2.8)$$

Only when a pair fragments is time is incremented by the amount

$$\Delta t = \frac{1}{N^2 w_{max}} \quad (2.9)$$

to ensure consistency with the previous scheme for a prescribed, constant time step. Making use of the fragmentation probability associated with this scheme, the mean time step can be derived from the expression for the general moments of the fragmentation distribution

$$\langle \Delta t^n \rangle = \sum_i \sum_j \frac{w_{ij}}{\frac{N(N-1)}{2}\langle w \rangle} \left(\frac{1}{N^2 w_{ij}} \right)^n = \frac{1}{\langle w \rangle N^2} \left\langle \frac{1}{(N^2 w)^{n-1}} \right\rangle \quad (2.10)$$

where $\langle w \rangle = \sum_i \sum_j w_{ij}/(N(N-1)/2)$. As anticipated, from the previous expression for the moments of the distribution we can derive in particular the mean time step, $\langle dt \rangle = 1/(N^2 \langle w \rangle)$, consistent with Equation (2.9).

Once the fragmentation event is accepted, we need to decide whether particle i or j will subsequently break. In this work, we study *symmetric fragmentation*, where a randomly chosen particle breaks [131, 133] and *asymmetric fragmentation* where either the larger *L-breakage* or the smaller particle *S-breakage* breaks [133]. We also distinguish between *deterministic* fragmentation [131, 133], where the chosen particle breaks into two equal fragments, and *stochastic* fragmentation, where the chosen particle breaks randomly into two off-springs. By following this procedure, it is possible to keep track of the kinetic evolution of the system, as well as gather statistics on the distribution of sizes.

In the next sections, we validate the proposed algorithm by comparing the results of kinetic evolution and statistics of sizes with previous analytical findings for symmetric and asymmetric kernels. In addition, the method allow us to examine the *L-breakage* and *S-breakage* models for generic kernels $K(x, y)$, for which no exact scaling solutions are known.

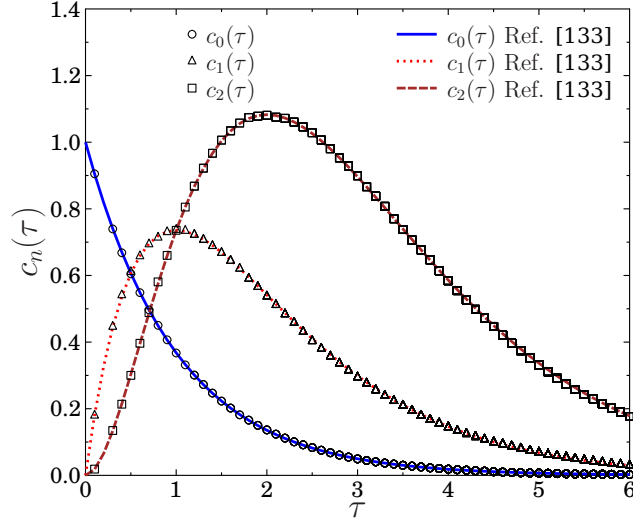


Figure 2.1: Time evolution of the particle size densities $c_n(\tau)$ in terms of the average number of collisions, τ , for the symmetric kernel $K(x, y) = 1$. The analytic solutions of Equation (2.12) are also shown for comparison

2.3 Symmetric Kernels

2.3.1 Symmetric Deterministic Fragmentation for $K(x,y)=1$

Ben-Naim and Krapivsky have examined analytically the fragmentation kinetics in systems where particles in a fragmentation event break symmetrically and deterministically into two equal fragments for the simplest kernel $K(x, y) = 1$ [133]. Starting from a monodisperse initial distribution where all particles have unit size a fragment produced after n fragmentation events has a mass $x = 2^{-n}$. Using this fact, they derived the dynamic evolution of the density of fragments $c_n(t)$ which have collided n times at time t

$$\frac{d}{dt} c_n(t) = N(t) [2c_{n-1}(t) - c_n(t)] \quad (2.11)$$

where the total density $N(t) = \sum_{j=0}^{\infty} c_j(t)$ represents to the average number of collisions experienced by a fragment up to time t . The evolution of Equation (2.11), in terms of the collision counter, $\tau = \int_0^t dt_1 N(t_1)$, is linear $\frac{d}{d\tau} c_n = 2c_{n-1} -$

c_n . Thus, for the initial conditions $c_n(0) = \delta_{n,0}$, the exact solution reads [133]

$$c_n(\tau) = e^{-\tau} \frac{(2\tau)^n}{n!} \quad (2.12)$$

As can be appreciated, the fragmentation leads to a singularity at a finite *shattering time* $t_c = 1$ (corresponding to $\tau = \infty$) where all the densities vanish: $c_n(t = 1) = 0$ for all n .

In Figure 2.1, we present numerical results for several particle size densities $c_n(\tau)$ obtained with the DSMC algorithm, comparing them with the corresponding analytical prediction, Eq. (2.12). The simulations have been performed starting with $N = 10^4$ particles with unit mass and taking as the collision frequency $w_{ij} = K(x, y) = 1$. In this case the maximum collision frequency could also be taken as $w_{max} = 1$. The comparison shows excellent agreement over the entire time range, indicating the good performance of the numerical scheme.

2.3.2 Symmetric Stochastic Fragmentation for generic a kernel $K(x, y)$

The proposed numerical approach can also describe general symmetric fragmentation kernels. In this case, a fragmenting particle of mass x splits into two fragments of mass y and $(x - y)$ with y chosen stochastically from the interval $0 < y < x$. For simplicity's sake, y is chosen uniformly from the interval $[0, x]$.

We have numerically analyzed product kernels $K(x, y) = x^p y^p$ and sum-kernels, $K = x^p + y^p$. For these systems, Equation (2.1) has scaling solutions of the type $\varphi(u)$ with $u = x/x^*$, which characterizes the late stages of their temporal evolution [134].

Moreover, for product kernels one can solve exactly the temporal evolution of the size distribution function and prove that dynamic scaling corresponds to the asymptotic regime of fragmentation kinetics. The characteristic value x^* generally corresponds to the mean value, $x^* = \bar{x}$, and for binary breakup the scaled distribution function, $\varphi(u)$, reads

$$\varphi(u) \equiv p e^{-u^p} / \Gamma(1/p). \quad (2.13)$$

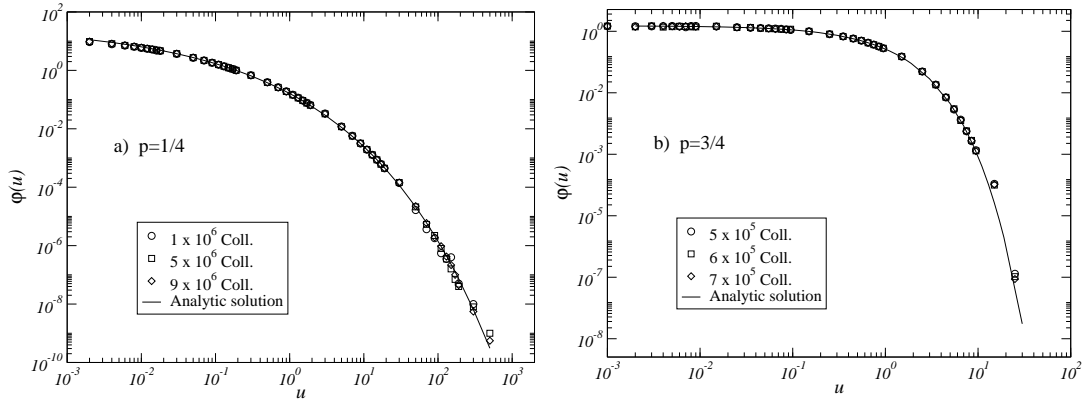


Figure 2.2: Scaled fragment size distribution, $\varphi(u)$, with $u = x/\bar{x}$ obtained during a stochastic fragmentation processes with symmetric product kernels, $K(x, y) = x^p y^p$. a) and b) illustrate results for $p = 1/4$ and $p = 3/4$, respectively.

Similarly, for sum kernels it has been shown that scaling distribution functions are consistent with the nonlinear fragmentation equation. An explicit form for such distribution was obtained [134]

$$\varphi(u) \equiv \frac{p e^{-u^p}}{\sqrt{u} \Gamma(3/2p)} \quad (2.14)$$

Starting from a monodisperse ensemble of fragmenting particles, we have found numerically that the size distribution relaxes towards a scaling distribution. In Figure 2.2.a and Figure 2.2.b the DSMC results for symmetric stochastic fragmentation for the product kernel $K(x, y) = x^p y^p$ and two different values of the exponent p are illustrated. One can observe the relaxation to the scaling distribution which agrees well with the theoretical prediction over a significant number of decades. Starting with $N = 10^3$ particles we can run the simulation up to $N \sim 10^7$ fragments which allows us to cover five orders of magnitude in scaled sizes and eight orders of magnitude in the distribution function making use of logarithmic sampling. The good agreement over such a wide range proves the excellent performance of the proposed approach, and its value in describing kinetics in systems with a variable number of particles. Product kernels show a shattering transition if $p < 1/2$, and hence the time evolution is quite different for the two examples displayed in Figure 2.2. Despite this difference, the fast relaxation to the dynamic scaled distribution

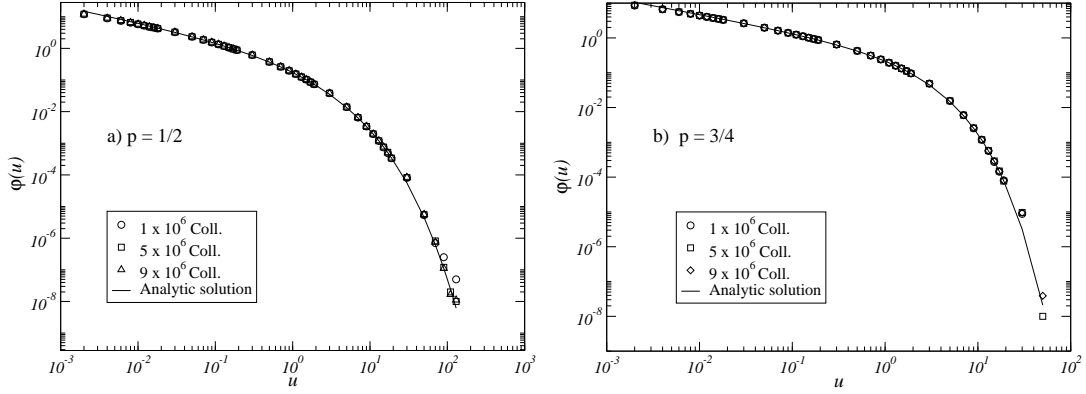


Figure 2.3: Scaled fragment size distribution, $\varphi(u)$, with $u = x/\bar{x}$ obtained during a stochastic fragmentation processes with symmetric sum kernels, $K(x, y) = x^p + y^p$. a) and b) display results for $p = 1/2$ and $p = 3/4$, respectively.

shows that shattering for $p = 1/4$ takes place after the system has reached the scaling regime.

Figure 2.3 displays the relaxation to the scaling distribution for sum-kernels $K(x, y) = x^p + y^p$ for two different values of the exponent p , and the simulation data are compared to the analytic prediction in the scaling regime. In this case we only have a prediction for the asymptotic, scaling regime and lack an exact solution of the fragmentation equation for a general initial condition. The excellent agreement between the numerics and the asymptotic prediction shows the relevance of the scaling distributions in the late stages of the kinetics of these fragmenting systems. For this kernel both examples display a shattering transition, which is not reached until the system relaxes to an asymptotic dynamic scaling regime.

2.4 Asymmetric Kernels

2.4.1 Asymmetric Deterministic Fragmentation for $K(x, y) = 1$

Reference [133] has also examined the asymmetric deterministic fragmentation process for the simplest kernel $K(x, y) = 1$. By exploiting the fact that the fragment mass density develops a traveling wave form and by analyzing the spectrum of possible propagation velocities of the wave front, they deter-

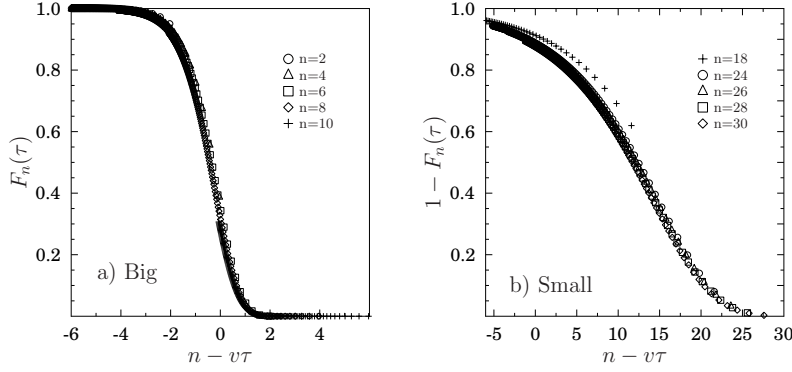


Figure 2.4: Evolution of the normalized cumulative size density $F_n(n - v\tau)$ for deterministic fragmentation, using the asymmetric kernels a) $K(x, y) = \theta(x - y)$ and b) $K(x, y) = \theta(y - x)$. The opposed asymptotic behavior of $F_n(n - v\tau)$ in the two cases is related to the different properties of the densities linked to the details of the fragmentation process.

mined that the extremal front velocity characterizes the asymptotic behavior of the mass distribution.

Larger particle splits. $K(x, y) = \theta(x - y)$

In the case the larger particle fragments deterministically, after n fragmentation events a particle with an initial mass of $x = 1$ will have a mass of $x = 2^{-n}$. Thus, the density $c_n(t)$ of particles which have experienced n fragmentation events at time t reads

$$\frac{d}{dt} c_n = 4c_{n-1}A_n - 2c_nA_{n+1} + 2c_{n-1}^2 - c_n^2 \quad (2.15)$$

where A_n is the cumulative density of fragments of mass 2^{-n} and smaller, and $A_n(t) = \sum_{j=n}^{\infty} c_j(t)$. As a result, starting from a monodisperse system, the density $c_0(t)$ of unit mass particles gives

$$c_0(t) = \frac{3(1-t)^2}{2 + (1-t)^3}. \quad (2.16)$$

Equation (2.15) notably simplifies in terms of the normalized cumulative densities $F_n(\tau) = N^{-1}A_n(t)$, which obey a non-linear evolution equation

$$\frac{d}{d\tau} F_n = 2F_{n-1}^2 - F_n^2 - F_n \quad (2.17)$$

in terms of τ , the average number of fragmentation events at time t . Equation (2.17) also admits asymptotically a traveling wave solution $F_n(\tau) \rightarrow f(n - v\tau)$. Thus, the front location $n_* \approx v\tau$, characterizes typical particle size $x_* = 2^{-n_*}$. For $L - Breakage$ the extremal speed takes the value $v = 1.52961$, so that the typical particle size does not correspond to the mean particle size as was the case for symmetric fragmentation. Such asymptotic behavior associated with the advancing front solution is consistent with a scaling regime for particle size distribution, $c(x) \rightarrow \frac{N}{x_*} \mathcal{F}\left(\frac{x}{x_*}\right)$, which scales with a typical particle size of $x^* = 2^{-v\tau}$ and in which the asymptotic shape of the scaling distribution is exponential for small and decays algebraically for large fragment masses. The algebraic decay depends on the advancing front velocity, v .

We have carried out numerical simulations to validate the development of the wave front profile, and in Figure 2.4.a we display the evolution of the normalized cumulative densities $F_n(\tau)$. We have used the theoretical prediction for the front wave speed to show that an accurate collapse in the front wave is indeed recovered after a short transient. One can see that the smaller the number of fragmentation events suffered by a particle the larger the deviation from the front wave profile, but that the relaxation is fast and deviations become negligible after a few fragmentation events. We have also analyzed the scaled mass distributions ranging over analogous number decades as in previous examples (data not shown), and have verified that a dynamic scaling regime is achieved after a short transient. For large fragments, the exponents characterizing algebraic decay are also consistent with theoretical expectations.

Smaller particle splits. $K(x, y) = \theta(y - x)$

When the smaller particle splits, the fragment mass density, $c_n(t)$, can be found using the rate equations

$$\frac{d}{dt}c_n = 4c_{n-1}B_{n-1} - 2c_nB_n + 2c_{n-1}^2 - c_n^2 \quad (2.18)$$

where $B_n = \sum_{j=0}^{n-1} c_j$ is the cumulative density of particles with mass larger than 2^{-n} .

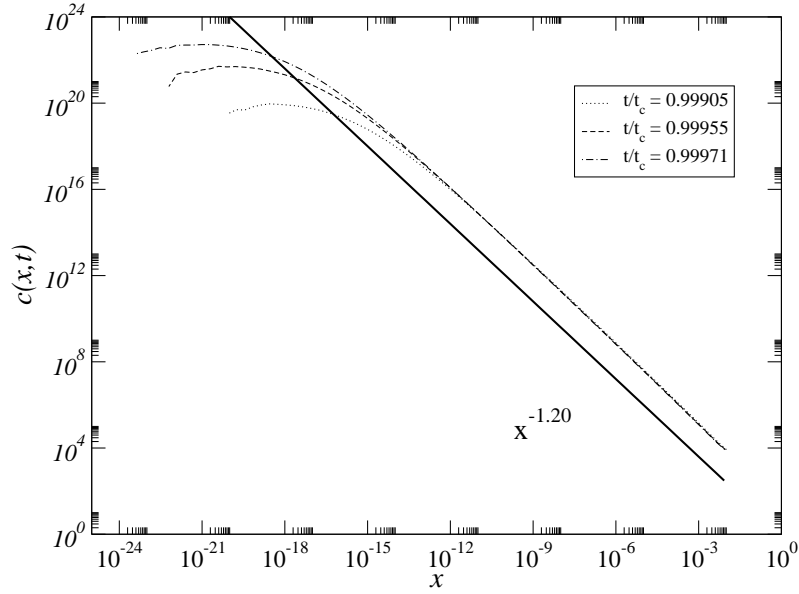


Figure 2.5: Fragment size distribution, $c(x, t)$, obtained for the asymmetric kernel $K(x, y) = \theta(y - x)$. We show the shape of the distribution as it approaches shattering, $t_c = 1$.

The density of unit mass particles is found by solving $\dot{c}_0 = -c_0^2$ and the $c_1(t)$ can also be found

$$c_0(t) = \frac{1}{1+t}, \quad c_1(t) = \frac{2}{1+t} \frac{(1+t)^3 - 1}{2(1+t)^3 + 1} \quad (2.19)$$

We have verified (data not shown) that with our simulation scheme the kinetics for these densities are recovered exactly, within numerical accuracy, in all the relevant time evolution regimes.

As in the previous case where the large particle splits, the evolution equation in terms of the relevant normalized cumulative density $F_n(\tau) = B_n(\tau)/N$ is also consistent with an asymptotic traveling wave behavior [133]. The predicted traveling wave velocity is much greater now than in the previous case, $v = 7.14509$, signaling a big gap between the mean, $\langle x \rangle$, and the characteristic, x^* , fragment sizes. In Figure 2.4.b we display the simulation results of $F_n(\tau)$ using the predicted value for the wave front speed. The simulations have been performed starting from a monodisperse system with $N = 10^3$ particles. There is a clear tendency for the normalized densities to collapse to a universal curve, indicating the relaxation towards the wave front regime. However, contrary to the situation where the larger particle breaks, the tran-

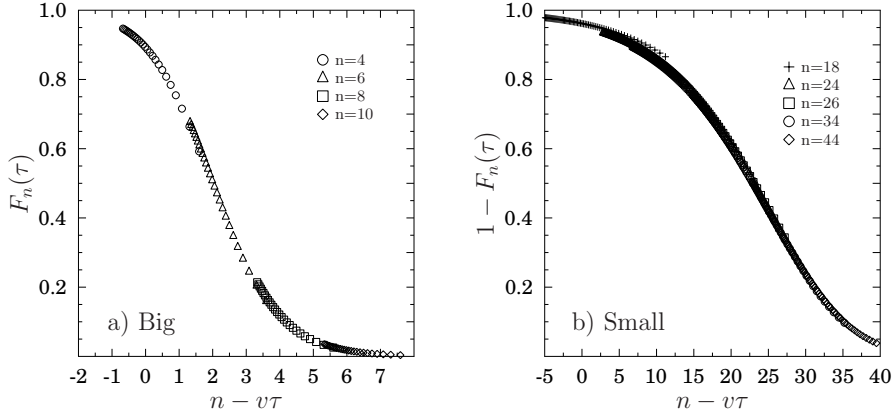


Figure 2.6: Evolution of the normalized cumulative size density, $F_n(n - v\tau)$, for stochastic fragmentation, using the asymmetric kernels a) $K(x, y) = \theta(x - y)$ and b) $K(x, y) = \theta(y - x)$.

sient is now much longer, as can be appreciated from the deviations from the scaling solution. One can see that the relaxation to the asymptotic wave front becomes heterogeneous. This slower relaxation to the traveling wave pattern also implies that mass distribution will approach the scaling asymptotic limit more slowly, as displayed in Figure 2.5. This model shows a shattering transition at $t_c = \frac{1}{N_0}$; the figure illustrates how the predicted algebraic decay, $c(x, t) \sim x^{-\alpha}$ with $\alpha \simeq 1.20191$ is reached for large masses, while deviations for small sizes still remain very close to shattering. In order to analyze carefully the slow convergence to scaling, and to sample the widest possible range, we have run simulations to reach up to $N = 10^8$ fragments. In performing these simulations the scaled distribution functions span five orders of magnitude in rescaled sizes (data not shown).

2.4.2 Asymmetric Stochastic Fragmentation

The asymmetric fragmentation model with stochastic breaking has also been analyzed analytically for the simplest uniform fragmentation kernel, *i.e.* $K(x, y) = \theta(x - y)$ for L-Breakage and $K(x, y) = \theta(y - x)$ for S-Breakage. Using the same theoretical approach as explained in the previous sections, it has been

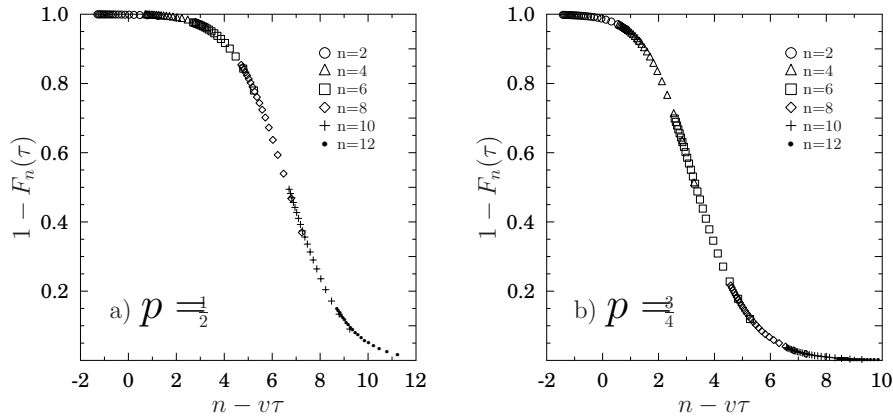


Figure 2.7: Evolution of the normalized cumulative size density, $F_n(n - v\tau)$, for stochastic fragmentation, using the asymmetric product kernel $K(x, y) = \theta(x - y)x^p y^p$. Results shown for a) $p = 1/2$ and b) $p = 3/4$, respectively

shown that both for large and small particle breakage the evolution of the normalized cumulative densities relaxes asymptotically to a front wave solution, $F_n(\tau) \rightarrow f(n - v\tau)$. For large particle fragmentation, $v = 1$, and hence the characteristic and mean size coincide, while for small particle fragmentation $v = 9$, which is larger than the deterministic fragmentation counterpart.

In Figure (2.6) we display $F_n(\tau)$ in both cases to show the convergence to the wave front solution using the theoretical predictions for v . As it was the case for asymmetric deterministic fragmentation, the convergence to the scaling asymptotic regime is slower for small particle breakage, while for large breakage it seems faster than in the deterministic case. One may speculate that the deviation between the mean and the typical masses induces additional kinetic heterogeneity which slows the relaxation to the asymptotic regime. We have also verified that the scaled mass distribution is also reached (data not shown) and that the distributions observed are consistent with theoretical predictions. Again, in accordance with the results obtained for $F_n(\tau)$, the convergence to the scaling distribution $c(x, 1) \sim x^{-\alpha}$ with $\alpha = 10/9$ for $x \gg x^*$ for small breakage is slower and more heterogeneous than for *L-Breakage* (data not shown).

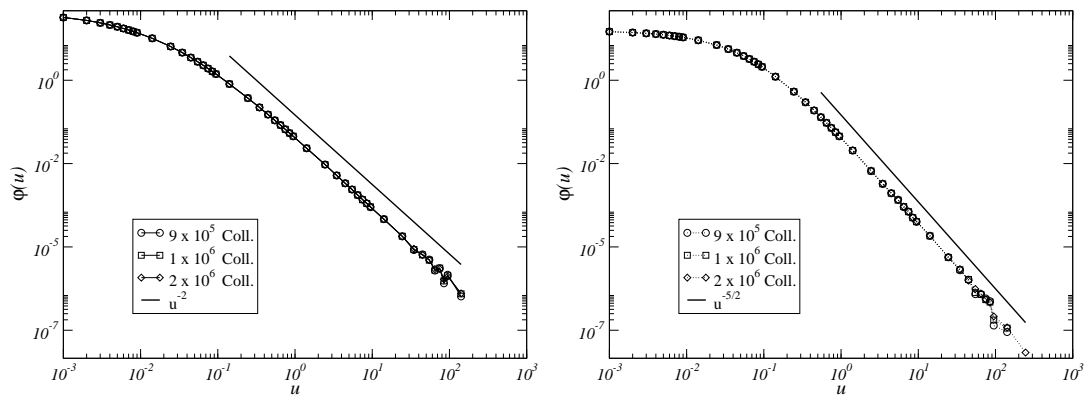


Figure 2.8: Scaled fragment size distribution, $\varphi(u)$, with $u = x/x^*$ for a stochastic fragmentation with an asymmetric product kernel $K(x, y) = \theta(x - y)x^p y^p$. The density distributions for a) $p = 1/2$ and b) $p = 3/4$ are shown.

We have analyzed more general kernels where fragmentation is asymmetric and stochastic to discern to what extent the concepts developed for the simplest fragmentation kernels can be extended to describe the kinetics of other families of fragmentation kernel. Specifically, in Figure 2.7 we show the normalized cumulative densities for small breakage for the product kernel, $K(x, y) = \theta(y - x)x^p y^p$. In this case we lack a theoretical prediction for the wave propagation. Hence, we have tuned it and chosen the speed of the wave front, v , for which we obtain the best fit. Specifically, we have obtained the front velocities $v = 1.05$ and $v = 1.15$ for $p = 1/2$ and $p = 3/4$, respectively. The convergence to the traveling front shape indicates that we can expect a scaling regime for the fragment size distribution where the shape size distribution function collapses in terms of the characteristic size $x^* = e^{-v\tau}$. Figure 2.8 shows the corresponding scaled mass distribution functions at different times to confirm that they do collapse to a scaling form with an algebraic tail. In both case the power law exponent is consistent with theoretical expectations for the scaling regime.

2.5 Discussion

We have introduced a numerical scheme to simulate the kinetics of non-linear fragmentation equations. The method is based on the Direct Simulation Monte Carlo (DSMC) technique, developed to solve the Boltzmann equation. The approach is easily generalized to other type of kinetic equations where the number of particles can vary during the kinetic evolution of the system.

We have performed careful comparisons for the simplest fragmentation kernels, where exact solutions exist. We have shown that the proposed approach can recover the detailed time evolution accurately, and have also validated the emergence of the asymptotic dynamic scaling regime. Such a comparison has shown the ability of the scheme to cover a significant number of decades in order to capture the broad size distributions characterizing fragmenting systems, thus making it possible to carry out quantitative, detailed comparisons. We have analyzed how to assess numerically the evolution of an advancing front in normalized cumulative size densities. The development of such a front is consistent with the relaxation to a dynamic scaling regime in the size distribution function, and hence constitutes an interesting alternative in situations where the convergence to the scaling regime is slow. Moreover, this alternative approach provides additional information, since the extremal velocity which characterizes the front evolution is related to the exponents characterizing the algebraic decay of the fragment distribution functions.

We have extended and made use of these concepts to analyze general fragmentation kernels, where exact analytic predictions for the kinetics of fragmenting systems are lacking. Furthermore, we have shown that with the good statistics achieved with the numerical technique proposed, it is possible to follow the development of an advancing front for generic asymmetric fragmentation kernels. Such an understanding promotes confidence in the development of scaling distribution functions, which we have also followed in time and whose development we have verified. By comparing different fragmentation kernels, we have seen that relaxation toward a dynamic scaling regime, which seems generic in the cases considered, is faster the closer the advancing front velocity is to 1, which means that the mean and characteristic

fragment sizes remain close to each other. It is reasonable to argue that the development of two well-separated and characteristic length scales hinder the temporal evolution of these systems.

Chapter 3

Cooling dynamics of a granular gas of elongated particles

Granular gases are dilute systems of macroscopic particles, which usually move randomly losing energy, due to their inelastic collisions. Starting from an equilibrium homogeneous state and in the absence of any external driving, these systems evolve into a homogeneous cooling state (HCS). In such a state, the kinetic energy, $E(t)$, decreases homogeneously and the time evolution of all variables occurs only through its global temperature [147–149]. Haff showed that the total energy of an inelastic gas of spherical grains, characterized by a constant restitution coefficient, evolves in time as a power law, $E(t) = \frac{1}{(1+t/\tau)^2}$, where τ is a characteristic time [150]. Very recently, Haff's law has been experimentally corroborated in systems of magnetized latex particles [151].

For any given inelasticity and above a certain system size, HCS becomes unstable and the system subsequently evolves into an inhomogeneous state where the cooling process slows down and decays as $E(t) = \frac{1}{1+t/\tau_h}$ independently of inelasticity [47, 152]. In this regime the collective motions of particles and vorticity determine the cooling of the gas, and large inhomogeneities in density are observed [47, 153, 154]. Hence, large cluster of particles develop, grow and interact due to the energy lost in collisions [47, 153, 154]. While for an infinite system this regime has been argued to correspond to the asymptotic free cooling evolution of a fluid of inelastic hard spheres, for any

finite system clusters eventually become of the order of the system size; in this regime the kinetic energy decays as the one in the HCS [45, 47, 54, 151]. These dynamical regimes, predicted theoretically, have also been validated numerically for hard disks and spheres with constant restitution coefficient [43, 155]; in particular Haff's law in the HCS [47], the algebraic decay in the hydrodynamic regime [152] and the regime where cluster sizes become of the order of the system size [47] have been validated.

There is experimental evidence that in some materials the restitution coefficient is not constant and that it rather depends on the relative velocity of the colliding grains. Moreover, there have been a number of theoretical studies which have analyzed in more detail the particle-particle interaction during the collision and how inelasticity emerges from such interactions [46, 68, 156]. For soft grains in which the repulsion force depends linearly on deformation, a constant restitution coefficient can be recovered [70, 157]. A more realistic account of particle deformation implements a Hertzian contact [64, 157], where the nonlinear elastic repulsive force leads to an algebraic decay of the kinetic energy during HCS which deviates from Haff's law, $\frac{E(t)}{E_0} = \frac{1}{(1+t/t_0)^{5/3}}$ [46, 158]. The implications of variable restitution coefficients in the instability of HCS and the subsequent inhomogeneous cooling regime have been addressed for viscoelastic spheres, where homogeneous cooling becomes the asymptotic state after a long transient controlled by inhomogeneous large clusters [159].

In the past, it was also shown that particle roughness leads to correlations between translational and rotational degrees of freedom and their corresponding kinetic energies [50, 54, 160, 161]. In general, both translational and rotational kinetic energies decay following Haff's law but differ from each other due to the breakdown of energy equipartition leading to correlations between translational and rotational kinetic energies; such correlations have been quantified for agitated spherical rough spheres [52, 55]. However, less is known about the freely cooling evolution of anisotropic particles [56, 162], although recently there has been an increasing interest in the dynamics of rod shape grains [163–167]. For example, in vibrated systems the particle anisotropy leads to net displacements and propulsion [168]. Such types of

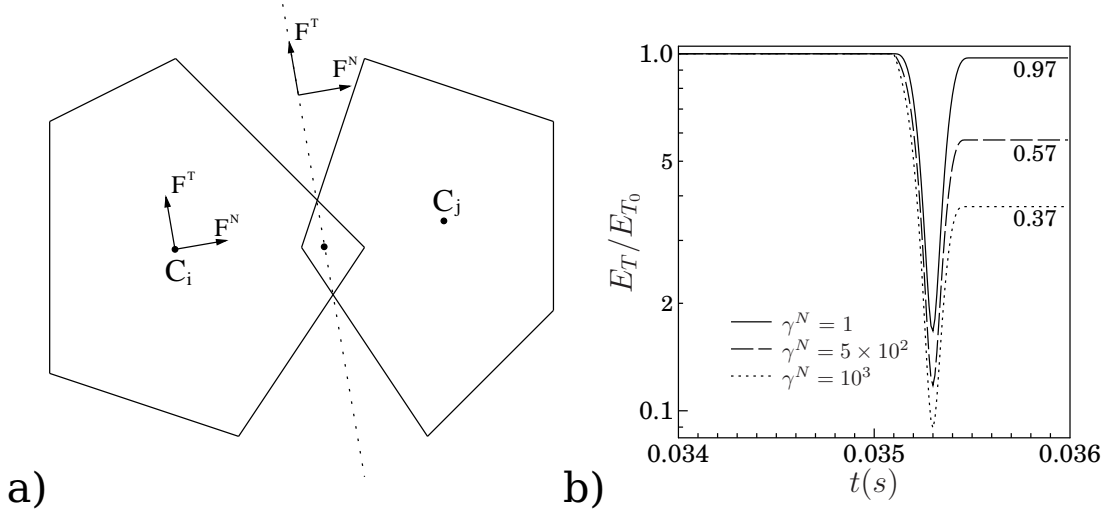


Figure 3.1: In a) A sketch of two interacting particles is presented. The force between two particles is proportional to the overlap area. The force is applied in the middle point of the line connecting the intersection points of the particles. In b) we show the total kinetic energy loss due to the collision of two particles, expressed as the ratio of the total energy after and before the collision (E_T/E_{T_0}). The total energy is computed as the sum of kinetic and rotational energies. The values shown here correspond to the maximum velocity experimented by the particles.

collective features favors clusters and other types of patterns, reminiscent of those observed in system of self-propelled elongated particle in model systems [169] motivated from biological materials [170, 171].

3.1 2D granular gas of irregular convex polygons

We consider a system of $2D$ irregular convex polygons, which are generated by a random Voronoi tessellation. The later allows to generate particles with variable degree of irregularity systematically [74]. Accordingly, the particle shape distribution is characterized by a single parameter $0 < a < 1$. The extreme value $a = 0$ corresponds to a regular distribution of rectangles with sides $S_1 = 1$ and $S_2 = d$, where $d > 1$ defines the grain aspect ratio.

Following our description, a system composed by N particles, of mass m_i

and moment of inertia M_i ,

When two particles come in contact they deform inelastically. Rather than describing the actual grain deformations, we keep the shape of the particles and allow them to overlap and determine the particle forces in terms of the overlapping area [71, 72, 74, 75, 77]. Accordingly, the total force between the two grains, can be decomposed $\vec{F}_{ij} = F_{ij}^N \cdot \vec{n} + F_{ij}^T \cdot \vec{t}$ in components, normal F_{ij}^N , and tangential F_{ij}^T , to the interface defined by the contact points of the two particles when they overlap. We introduce the normal, \vec{n} , and tangential, \vec{t} , vectors to the common interface, which is depicted in Figure 3.1a. The force is applied at the middle point of the common interface. Although the center of mass of the overlapping area could have been chosen as the relevant position [77], no qualitative changes have been appreciated in tests performed as far as the results described subsequently are concerned.

The normal component contains an elastic contribution, proportional to the pair overlap area, A_{ij} , and a dissipative contribution

$$F_{ij}^N = -k_n A_{ij} - m_{ij}^{eff} \cdot \gamma^N \cdot v_{ij,rel}^N, \quad (3.1)$$

where k_n is the Young modulus, γ^N is the damping coefficient in the normal direction, $m_{ij}^{eff} = \frac{m_i \cdot m_j}{m_i + m_j}$ is the relative mass of the colliding pair and $\vec{v}_{ij,rel}^N = (\vec{v}_j - \vec{v}_i) \cdot \hat{n}$ stands for the normal component of their relative velocity. In general, for regular particles it is possible to derive analytic expressions for the overlap area as a function of the separation between the particle center of mass. For particles of irregular shape, however, it is computed numerically [71, 72, 74, 75, 77].

The tangential component of the interaction force is characterized also by an elastic and a dissipative contribution, and obeys the Coulomb constraint, $F_{ij}^T \leq \mu |F_{ij}^N|$, where μ stands for the static friction coefficient. Accordingly, we write

$$F_{ij}^T = -\min(-k_t \xi_{ij} - m_{ij}^{eff} \cdot \gamma^T \cdot |v_{ij,rel}^T|, \mu |F_{ij}^N|), \quad (3.2)$$

where γ^T is the damping coefficient in the tangential direction and $\vec{v}_{ij,rel}^T = (\vec{v}_j - \vec{v}_i) \cdot \hat{t}$ corresponds to the tangential component of their relative velocity. The elastic force is now characterized by ξ_{ij} , the elastic elongation associated

to the overlapping pair. It behaves as an Cundall spring [76]

$$\frac{d\xi_{ij}(t)}{dt} = v_{ij,rel}^T, \quad (3.3)$$

which evolves as long as there is an overlap between the two particles.

The equations of motion, Equations (1.5-), are integrated using a fifth order predictor-corrector algorithm with a numerical error proportional to $(\Delta t)^6$ [44], while the kinematic tangential relative displacement, Equation (3.3), is updated using and Euler's algorithm. In the simulations, we have used the parameters $\frac{k_t}{k_n} = 0.1$, $\frac{\gamma^N}{\gamma^T} = 3$, $k_n = 4 \times 10^2 Nm$, $\mu = 0.25$, introduced in previous works [72, 77]. For this range of parameters we have set a time step $dt = 10^{-6}s$. The damping coefficients γ^N and γ^T quantify the inelasticity of the collision. In order to address their impact in the evolution of anisotropic grains, we have varied them. To understand their relationship with the energy lost in a collision, we have analyzed the interaction between a pair of rectangles. In Figure 3.1b we display the behavior of the total kinetic energy, E_T , during one collision. For convenience, the values are rescaled to the total kinetic energy just before the collision starts, E_{T_0} . The data correspond to several damping coefficients γ^N , which quantifies the variation and the relevant range of dissipation. The numerical values of the corresponding effective restitution coefficients are also shown. In general the total energy lost strongly depends on the initial particles' relative velocity. Consequently, to identify the effective velocity depended restitution coefficient is not very obvious. The values of the damping coefficient displayed range from particles which loose a rather small amount of kinetic energy up to particles where around the 70% of the pair incoming relative kinetic energy is lost in one collision. The data shown correspond to particles with a relative impact velocity of 1 m/s, which is the highest value experimented by the particles in the present numerical studies.

In the next sections, we focus on rectangles with variable aspect ratio, d . For the rectangles, when two vertices overlap with the same side, no special care is necessary as long as the used parameters always warrant that the maximum overlap is much smaller than the particle size. In the very unlikely situation where two vertices of one particle overlap with a pair of vertices of

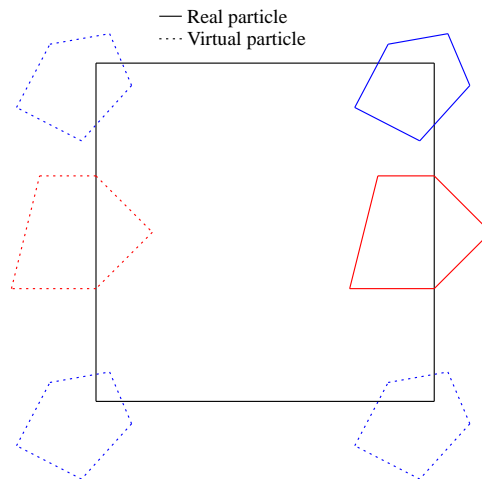


Figure 3.2: When a particle starts to leaves the system, a virtual particle is *created* on the opposite side (Red particles). For the particular case that the particle leaves the box from a corner then a virtual particles is *created* at all the other corners (Blue particles).

a second particle, leading to full face to face interaction, the contact surface is defined by the two middle points between the corresponding closest pair of vertices. The other steps of the procedure remain unchanged. Systems of irregular particles characterized by a parameter ($1/4 \leq a \leq 1/2$) (data not shown) were also explored, without observing any relevant differences with the results we will analyze below.

3.1.1 Boundary conditions

The simulations are carried out in a square box of size L and a fixed number of grains, N , at a prescribed area fraction, ν . In order to minimize finite size effects, we have used periodic boundary conditions. Due to the general shape of the grains, whenever a particle leaves one side of the box, we need to replicate it in the opposite side. Accordingly, we generate a list of *virtual particles* which include all particles that have at least one vertex out of the system. As soon as a particle starts leaving the system, it is added to the list of *virtual particles*. When the center of mass of the particle crosses one of the system's boundaries, then the position of the reference particle is updated following the standard procedure. Such a change alters the status of the reference particle and the virtual ones, which is updated appropriately in the *virtual particle* list.

For consistency in case the particle goes out through a corner three virtual particles are created, as illustrated in Figure 3.2. The virtual particles are regarded as standard particles when computing inter-particle forces. Note that the force computed for a virtual particle is applied to the corresponding *real* particle the *virtual* particle is linked to. Also the change in position of the real particle leads to the corresponding change of the virtual particles linked to it.

3.2 Freely evolving anisotropic grains

We have numerically studied the free cooling kinetics of a dilute system of $N = 3000$ polygons at area fraction $\nu = 0.07$ confined within a square box. Initially, the particles are homogeneously distributed and their translational and rotational velocities follow Gaussian distributions. In order to avoid memory effects from the initial conditions, we allow the system to execute a few collisions before starting to analyze the particles' temporal evolution, which we follow until the total mean translational and rotational kinetic energies have decayed several orders of magnitude. All data shown correspond to averages over at least five different initial configurations.

In Figures 3.3 and 3.4 we display snapshots of the density and velocity fields for rectangular grains with aspect ratio $d = 5$. We have explored the system's behavior for two extreme damping coefficients (used in Figure 3.1b) to quantify the inelasticity of typical collisions. In both cases we can distinguish an initial homogeneous decay, which corresponds to HCS. This state is unstable and the granular gas develops density inhomogeneities leading to cluster formation. Since eventually the decay in the grains' velocity will decrease the inelasticity lost in the collisions, we expect a homogeneous asymptotic behavior analogous to the one put forward for viscoelastic isotropic grains [46, 159].

The behavior of the granular gas in the inhomogeneous regime shows a clear dependence on the damping coefficient, γ^N . For weakly dissipative particles, $\gamma^N = 1s^{-1}$ (see Figure 3.3), one can appreciate the smooth development of a velocity field leading to the formation of clusters which coalesce and merge into large structures (see Figure 3.3b). At longer times, however, these big clusters show a tendency to break, avoiding the development of the

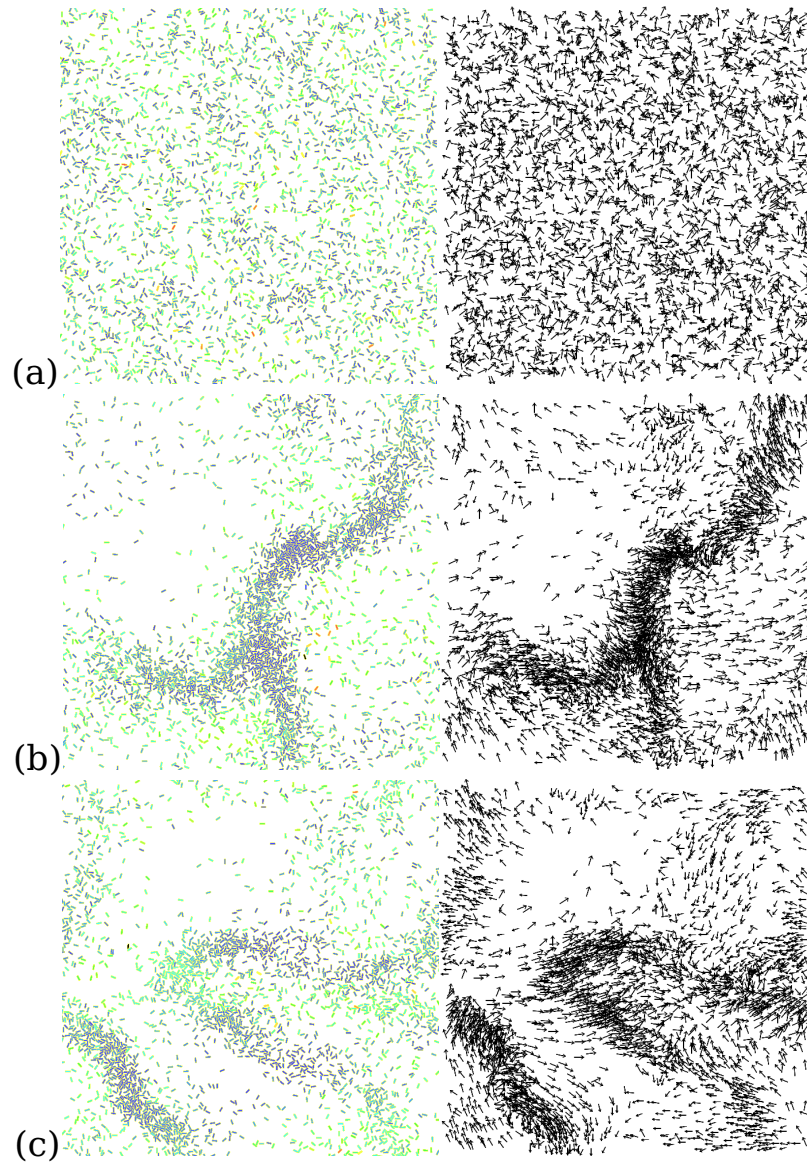


Figure 3.3: Spatial evolution of a system with elongated particles $d = 5$ and a damping coefficient of $\gamma^N = 1 \text{ s}^{-1}$. The first column shows the screenshots of the system, the second illustrates the velocity fields. The lighter the particles the faster they are. Pictures at $t = 10 \text{ s}$ (a) , $t = 100 \text{ s}$ (b) and $t = 200 \text{ s}$ (c) are presented.

clustering instability (see Figure 3.3c), in agreement with the predictions for viscoelastic grains [159, 172]. On the contrary, highly dissipative grains, with $\gamma^N = 10^3 \text{ s}^{-1}$, develop marked clusters of smaller sizes much faster, as can be appreciated in Figure 3.4. Such clusters are correlated with the quick devel-

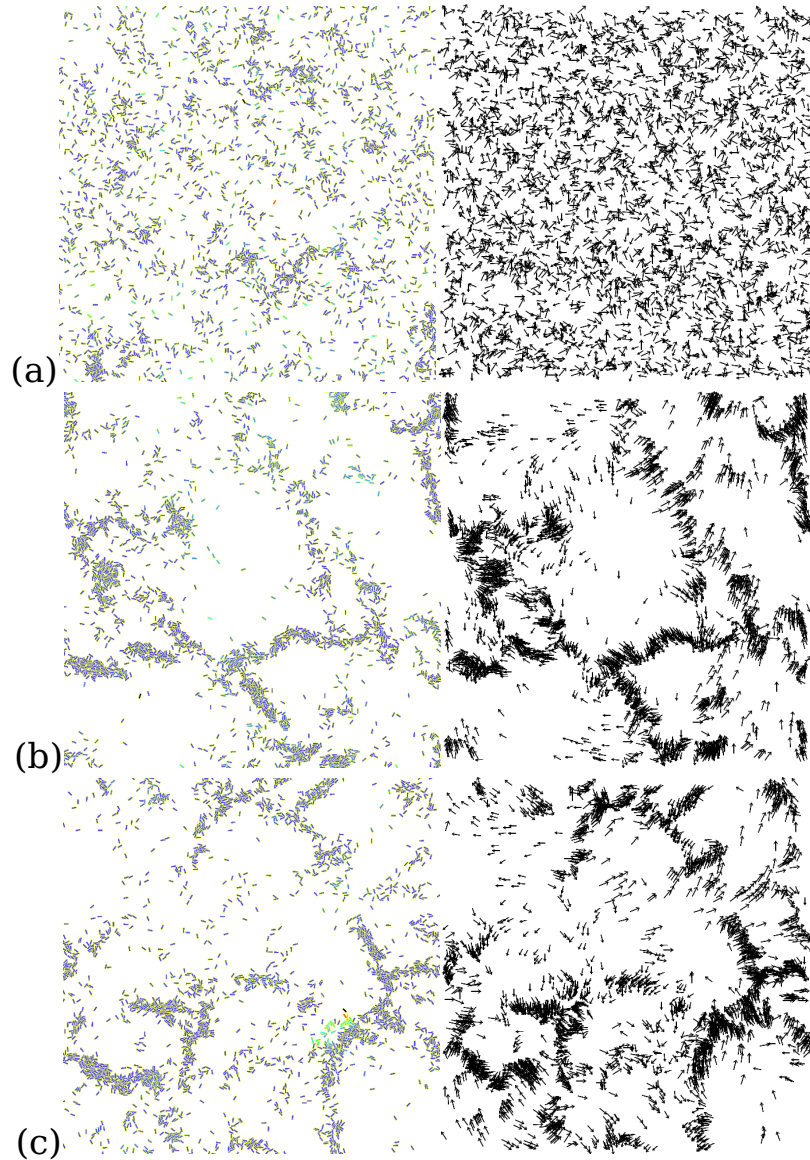


Figure 3.4: (Color online) Spatial evolution a system with elongated particles $d = 5$ and a damping coefficient of $\gamma^N = 10^3 s^{-1}$. The first column shows the screenshots of the system, the second illustrates the velocity fields. The lighter the particles the faster they are. Pictures at $t = 10 s$ (a), $t = 100 s$ (b) and $t = 200 s$ (c) are presented.

opment of complex vortex structures in the grains' velocity field. These well defined, small clusters, tend to coalesce at larger times, although the overall process of large cluster development is severely slowed down when compared to the evolution of weakly dissipative clusters. Increasing the particle

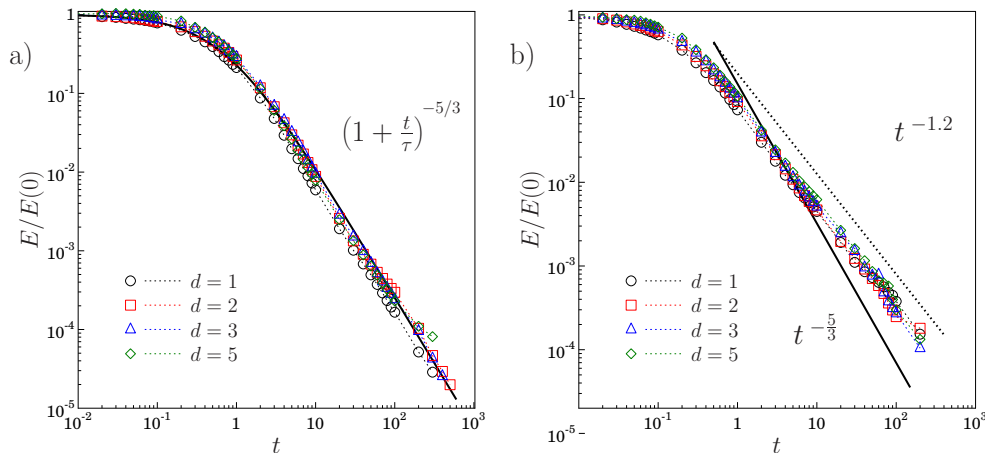


Figure 3.5: Evolution of the translational kinetic energy of the system in time. Particles with several aspect ratios from $d = 1$ to $d = 5$ are studied. Results for two very extreme damping values are shown, a) $\gamma^N = 1 \text{ s}^{-1}$ and b) $\gamma^N = 10^3 \text{ s}^{-1}$. For comparison the analytical prediction for a system of viscoelastic circles as well as our best fit for the inhomogeneous cooling process are shown as lines.

anisotropy (data not shown) enhances this distinct evolution with the particle energy dissipation. In the past, a similar trend has been observed for rough spheres, where it has been shown that energy transferred into rotational degree of freedoms delays cluster development [52].

We have quantified the temporal evolution of freely evolving gases of rectangular grains by monitoring the mean translational and rotational kinetic energy of the system, usually referred to as granular temperatures. Figure 3.5 displays the decay of the translational kinetic energy, $E(t)$, of a granular gas for weak and strong dissipative rectangular grains with aspect ratio $d = 5$. After a short transient, $t > 0.1 \text{ s}$ the decay is algebraic in agreement with the analytic predictions for the homogeneous cooling state of hard and viscoelastic grains.

Since the dissipation in these systems is proportional to the relative velocity difference and the restitution force is a nonlinear function of the overlapping area (see Equation 3.1), one can expect the system evolves analogously to a gas of hard viscoelastic grains [46]. We have verified that this is consistent with the results obtained for weakly dissipative grains. The algebraic

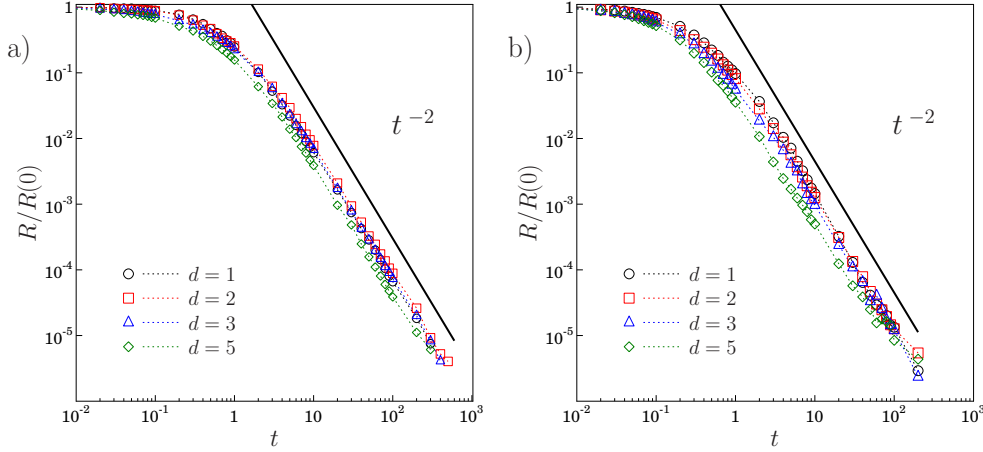


Figure 3.6: Evolution of the rotational energy of the system in time. Particles with several aspect ratios from $d = 1$ upto $d = 5$ are studied. Results for two very extreme damping values are shown, a) $\gamma^N = 1 \text{ s}^{-1}$ and b) $\gamma^N = 10^3 \text{ s}^{-1}$. For comparison the Haff's analytical prediction t^{-2} is also shown.

decay depicted in Figure 3.5a is characterized by the same exponent, $\beta = -\frac{5}{3}$, analytically predicted for viscoelastic grains [46]. However, this is not the case for highly dissipative grains, which cool down slower, with a characteristic smaller exponent, $\beta \approx -1.2$, in the algebraically decaying regime. It is important to remark that the limitations of the used numerical scheme prevented us to perform calculation with higher dissipative systems, for reaching the hydrodynamic algebraic decay, $E(t) \sim t^{-1}$ limit [152].

On the other hand, for weakly dissipative systems, the decay of the translation kinetic energy also slows down at longer times. This can be attributed to the development of stronger velocity correlations. Nevertheless, the narrow time regime (system size effects) does not allow us to quantify the algebraic dependence characteristic of the hydrodynamic regime, $E(t) \sim t^{-1}$ [152]. Contrary, the faster decay ($t^{-\frac{5}{3}}$), which can be attributed to the dominance of big clusters is quickly recovered. Larger system sizes will be required to identify the relevance of the intermediate regimes before reaching the asymptotic state. For highly dissipative grains the smaller exponent, observed from very short times, may suggest an earlier departure from HCS. In this case, the interplay of cluster formation and break up with the development of large clus-

ters and their impact in the overall kinetic energy decay also remains to be clarified. Nevertheless, Figure 3.5a and Figure 3.5b clearly indicate that neither the dissipation nor the shape does significantly modify the functional dependence and the characteristic time scales in which the systems cool-down. Moreover, analogous results (data not shown) are obtained for irregular particles with $(1/4 \leq a \leq 1/2)$.

Figure 3.6 shows the decay of the rotational kinetic energy. After a short transient, for $t > 1$ s, we observe an algebraic decay characterized by an exponent -2 regardless of particle shape and inelasticity. This exponent, in agreement with Haff's law, can be understood assuming weak rotational-translational correlations. The latter can be traced back to the fact that above the Coulomb threshold, both the elastic and dissipative contributions of the tangential force are linear functions of the lateral displacement and relative velocity, respectively (see Equation 3.2). The deviations observed in $E(t)$ at longer times are much weaker for rotational kinetic energy, suggesting that rotations are much less sensitive to the development of spatial inhomogeneities. The different behavior in the decay of rotational and translational kinetic energy indicates a lack of energy equipartition during the whole cooling process of the anisotropic grains, both in the homogeneous and inhomogeneous regimes.

During the cooling process the velocity statistics was also examined (see Figure 3.7a and Figure 3.7b). Starting from a Maxwellian speed distribution, the particle velocity distribution evolves with a scale characterized by the mean translational kinetic energy. For weakly dissipative particles, which cool down more uniformly over a wide range of times, it is reasonable to expect that all the temporal dependence enters through the translational temperature and we can then identify a dynamic scaling regime where the scaled velocity distribution becomes stationary. Such a picture is consistent with the results shown in Figure 3.7a, where we show the scaled speed distribution, $P(c)$ ($c = \frac{v}{\bar{v}}$), at the initial and final times. Regardless of the particle anisotropy, the distribution shape remains close to a Maxwellian. For highly dissipative grains, larger fluctuations are observed, although the shape remains also close to a Maxwellian. In this case, one can argue that such a behavior arises as a result

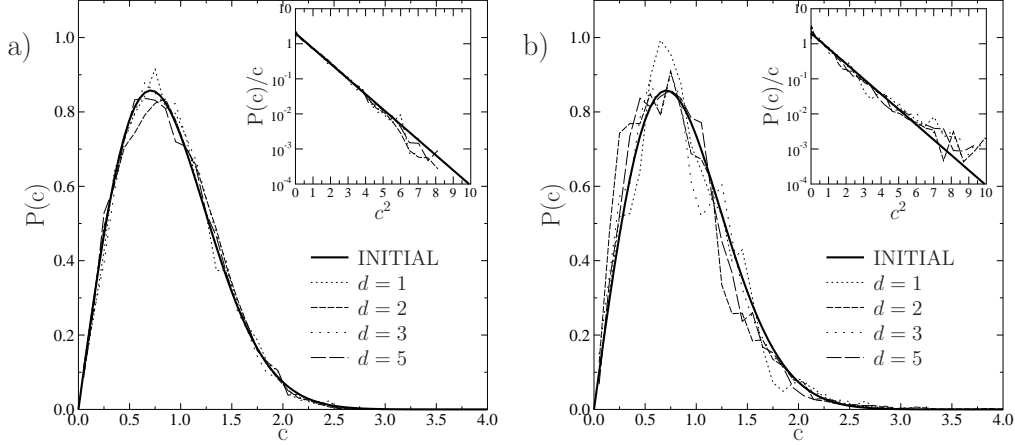


Figure 3.7: Scaled speed distribution several particle shapes, ranging from $d = 1$ to $d = 5$. In all cases, the data correspond to very late times; for comparison the initial speed distribution is also shown. a) Weak dissipative particles, $\gamma = 1$ and b) strong dissipative particles, $\gamma = 10^3$. The insets show the tails of the velocity distribution functions.

of the presence of independently evolving clusters. Finite size limitations prevents us from analyzing the tails of the distributions, where deviations from the Maxwellian behavior may develop and become good indicators of the different features of weak and strong dissipative granular gases.

To gain insight into the role of particle anisotropy on the collective features of freely evolving granular gases, we have analyzed the structure of the clusters which the system spontaneously develops. In the simulations, two particles are regarded as part of the same cluster if there is any contact between them, *i. e.* when the inter-particle overlap area is larger than 10^{-6} . We have first considered the radial distribution function of connected particles $G(r)$ within a given cluster

$$G(r) = \left\langle \frac{N(r + \delta r)}{2\pi r \delta r \rho} \right\rangle, \quad (3.4)$$

where $\rho = N_T/A$ is the average number of rods per unit of area measured by counting the total number of rods N_T whose center of mass lies in the analyzed area A . $N(r + \delta r)$ accounts for the number of particles, within the cluster, with their center of mass at a distance r within a differential of area $\delta S = 2\pi r \delta r$. The value of $G(r)$ correspond to a mean value obtained over the whole system.

In Figure 3.8, the radial distribution function of connected particles, $G(r)$ is illustrated for particles with different damping coefficients and variety of aspect ratios. At short distances, weakly dissipative grains display weak, short range correlations characterized by the particle's longest side, clearly visible in Figure 3.8a. One can appreciate a correlation hole close to contact and subsequently the radial distribution function develops a smooth peak whose relative height decreases as the particle anisotropy increases. For strongly dissipative particles the short range structure is markedly different, as shown in Figure 3.8b. The inelasticity induces strong short range structures which correspond to the different structures in which the particles can pack locally, depending on their aspect ratio. The drawings in the figure indicate some of the structures where one can find particles either perfectly aligned parallel to each other along their long faces, or perpendicular to each other alternating long and short faces. This packing gives rise to clearly marked peaks, whose positions change with the aspect ratio, d . The relative height of the peaks also decrease with particle anisotropy, but in all cases their height are larger than the corresponding particle anisotropies with smaller damping coefficient. This tendency to more marked close packed structures arise as a combined effect of dissipation and alignment induced packing associated to the particles shape. The insets of Figure 3.8 display the long distance decay of the radial distribution function. The particle dissipation gives rise to larger values of the radial distribution function at contact, but in both cases, and for all the aspect ratios analyzed, we observe a long range decay, characteristic of the development of long range clusters and structures. Such long range structures have been observed in agitated isotropic grains as a result of long range hydrodynamic correlations due to the lack of detailed balance in these out of equilibrium systems [173].

Further information on the local structure of rod alignment is obtained from the radial orientational distribution of connected particles within a given cluster, $Q(r)$, which can be defined as

$$Q(r) = \langle Q_{ij} \rangle \quad Q_{ij} = \cos(2(\theta_i - \theta_j))\delta(\mathbf{r}_{ij} - r) \quad (3.5)$$

where θ_i and θ_j are the angular orientation of particles i and its connected neighbor j , at a distance r_{ij} . This distribution function provides quantita-

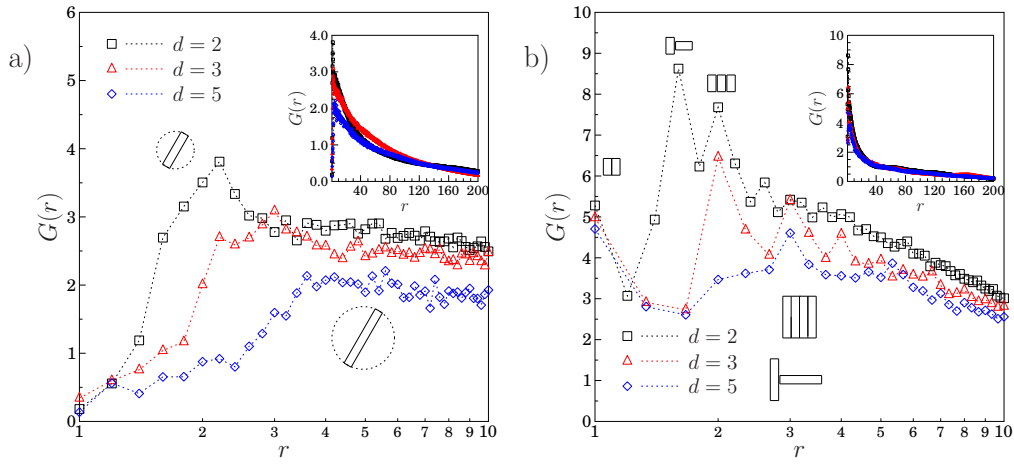


Figure 3.8: Radial distribution function of connected particles obtained for system of particles with aspect ratios from $d = 2$ to $d = 5$. Results for two very extreme damping values are shown, a) $\gamma^N = 1 \text{ s}^{-1}$ and b) $\gamma^N = 10^3 \text{ s}^{-1}$. In both cases the particle alignment corresponding to a few relevant peaks in the radial distribution function are drawn.

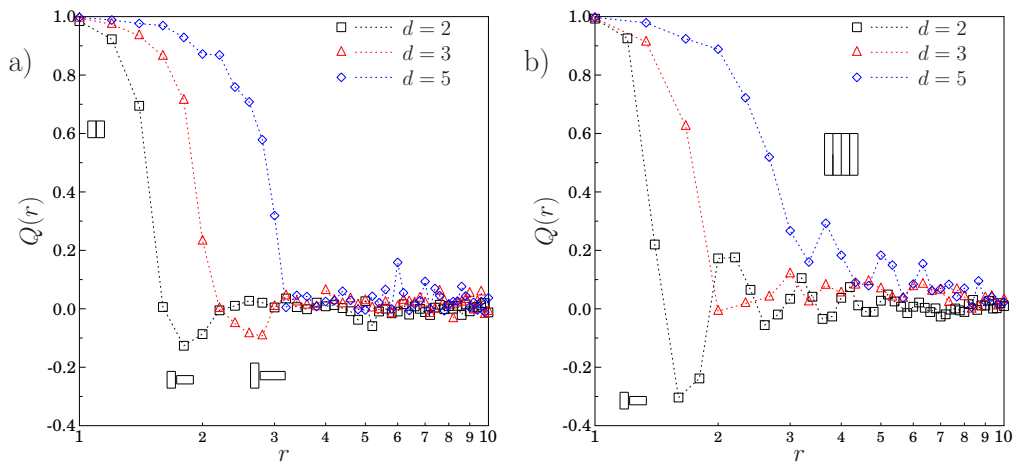


Figure 3.9: (Color online) Radial orientation distribution functions of connected particles, $Q(r)$, as defined in Equation 3.5 for system of particles with aspect ratios from $d = 2$ to $d = 5$. Results for two very extreme damping values are shown, a) $\gamma^N = 1 \text{ s}^{-1}$ and b) $\gamma^N = 10^3 \text{ s}^{-1}$. In both cases the particle alignment corresponding to a few relevant peaks in the radial orientation distribution function are drawn.

tive information on the local structure of the clusters because configurations where the two particles are perpendicular to each other contribute -1 , while particles aligned along their long faces or along their short faces contribute 1 .

On Figure 3.9a, the $Q(r)$ numerical data clearly indicates that weakly dissipative systems do not show significant structure. There is a peak at contact ($r = 1$), because at this shortest distance only perfectly aligned particles along their long faces can contribute. At larger distances a small deep indicates a small preference at these intermediate distances to observed perpendicularly aligned particles. But overall, it is the relaxation from the completely aligned structure at contact which dominates $Q(r)$. On the contrary, Figure 3.9b shows that after the decay of the compact structure at contact, a series of maxima (parallel alignment) and minima (perpendicular alignment) develop at intermediate distances corresponding to the high tendency of these dissipative particles to align in close packed structures. The radial orientation distribution function shows a faster decay than the radial distribution function, suggesting that angular correlations are short range.

Finally, in Figure 3.10 we show the local nematic order parameter for the freely evolving gas, $S(t)$, defined as

$$S(t) = \frac{1}{N} \sum_i^N \frac{1}{N_c} \sum_j^{N_c} Q_{ij} \quad (3.6)$$

We restrict the sum of the orientational function, introduced in Equation (3.5), to the particles which are in contact with a reference particle i , N_c is the amount of particles that are in contact with i . $S(t)$ naturally captures the local angular correlation, and it runs from $S(t) = 1$, representing the maximum local correlation to $S(t) = 0$, which corresponds to a locally disordered system. Figure 3.10 clearly indicate that particle anisotropy induces local nematicity in the clusters of particles, even at even at very early stages for highly dissipative articles. The local ordering into a nematic structure grows with particle anisotropy. For weakly dissipative particles, however, no local angular correlation is found as shown in the inset of Figure 3.10. For these particles the clusters gather particles which avoid overlapping each other but without any significant local angular correlation.

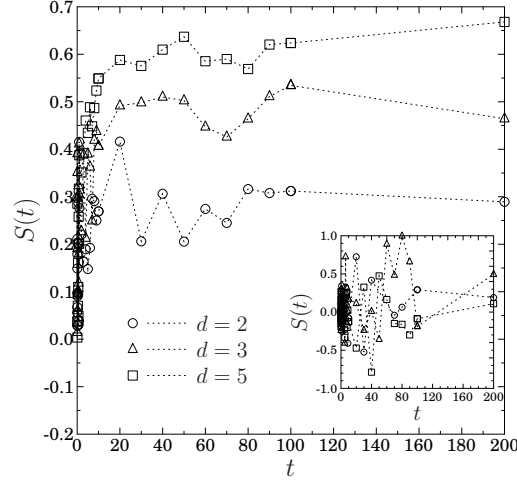


Figure 3.10: Nematic parameter at contact, $S(t)$. Results for $\gamma = 10^3 s^{-1}$ and three different anisotropies are depicted. The inset shows the corresponding behavior for weakly dissipative particles, $\gamma = 1 s^{-1}$.

3.3 Discussion

In summary, we have examined the cooling dynamics of a 2D granular gas of elongated grains. For weakly dissipative particles, we have found that the mean kinetic energy decreases asymptotically as $\frac{E(t)}{E_0} = \frac{1}{(1+t/t_0)^{5/3}}$, in agreement with Brilliantov and Pöschel predictions for the homogeneous cooling state regimen (HCS) of viscoelastic particles [46, 158]. A higher dissipation induces an inhomogeneous cooling process and the energy vanishes as $\frac{E(t)}{E_0} \sim t^{-1.2}$. The rotational energy, however, always decays as $\frac{R(t)}{R_0} \sim t^{-2}$, which is agreement with Haff's prediction for the HCS of inelastic particles. The lack of energy equipartition is kept even during the inhomogeneous cooling process where strong inhomogeneities in the velocity field are presented.

We also have observed a strong influence of the particle shape and inelasticity on the structure of the clusters which develop in the inhomogeneous cooling regimes. The combined analysis of the radial distribution function, $G(r)$, the angular correlation, $Q(r)$, and the local nematic order parameter, $S(t)$, clarify the cluster structure. Highly dissipative grains show a marked tendency to form ordered clusters with strong local angular correlations. There-

fore, the system is nematogenic in this cooling process, and one can expect that the observed clusters display a significant nematic order. The latter, which increases with particle elongation, is very closely related to the typical face to face interaction. The relevance of the interplay between particle shape and inelasticity has been clearly appreciated by analyzing the structures of weakly dissipative grains, where the local nematicity is essentially absent and the density inhomogeneities are statistically much more isotropic. Our numerical outcomes suggest that the strong dissipation and the particle anisotropy induce the formation of ordered cluster structures and velocity vortices, which notably slow down the cooling process and retard the appearance of large clusters which break and reform. Increasing the particle anisotropy enhances this distinct evolution as a function of the particle energy dissipation. This behavior can be attributed to the detailed interaction between ordered clusters of particles, where rotational degrees of freedom play a relevant role. The breakup of big clusters of elongated particles as a results of their collisions leads to the formation of smaller clusters, promoting a faster decay of the rotational kinetic energy. Such smaller clusters of ordered particles in turn delay the development of the inhomogeneous cooling regime. Understanding the impact of these strong correlations in agitated systems where energy is supplied continuously constitutes an interesting venue in the fundamental understanding of the physics of anisotropic granulates and the subtle interplays between particle shape and inelasticity.

Chapter 4

Stress distribution of faceted particles in a silo after its partial discharge

The design and exploitation of granular silos benefits from a detailed knowledge of the mechanical properties of particle storages. In fact, a poor understanding of the impact that the grain properties has on granular deposits necessary leads to a poor performance of the silo, both in terms of its storage capabilities as well as its overall structural stability. Since the collective behavior of such systems is not always easy to measure and control experimentally, numerical modeling usually provides a very useful complementary approach for understanding very complex processes like silo filling and discharging [174–178].

In previous works, it was found the remarkable role that flat faces play in the stress propagation of granular deposits [166, 179]. Elongation favors rods' alignment transverse to gravity, hindering stress transmission to the lateral walls of the container. Then, as the particles increase their length, force saturation becomes strongly reduced. On the contrary, squares tend to orient with a diagonal parallel to gravity, transmitting the stress at $\pi/4$ with respect to the gravity. This results in a clear saturation of the pressure with depth, similar to what is observed in granular silos and known as Janssen's effect.

In this chapter, we present a systematic theoretical and experimental co-

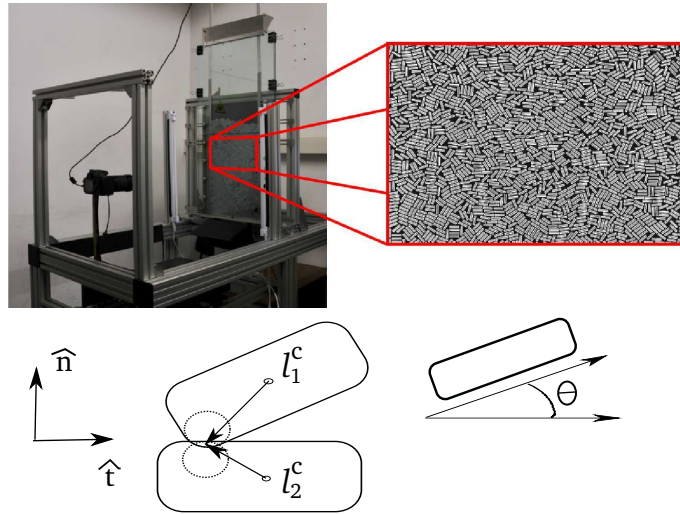


Figure 4.1: Photograph of the experimental setup of the two dimensional silo. On the right, as example, there is a zoom of the $d = 5.4$ rods deposited in the bulk of the granular layer.

ordinated study of the structural and mechanical properties of packings of faceted particles after their partial discharge from a silo. We show that particle shape and elongation has a profound effect on the process of silo discharge and consequently, on the stress profiles developed. Hence, grain aspect ratio becomes a key parameter which controls the properties of packings of faceted particles within a silo. The simulations have been developed by T. Kanzaki and R.C. Hidalgo in the framework of the project Estabilidad y dinámica de medios granulares anisótopos (FIS2008-06034-C02-02). The experiment have been conducted by researchers at University of Navarra in the framework of the project *Interacciones entre partículas y emergencia de propiedades macroscópicas en medios granulares*. (FIS2008-06034-C02-01)

4.1 Experiment

The experimental setup consists on a smooth, two dimensional silo filled either with rods or square nuts (Figure 4.1). Two types of rods of 1.0mm diameter have been used in this work. Both are monodisperse stainless steel rods with different lengths: 2.4 and 5.4 mm . Hence, the aspect ratio of the rods is $d = 2.4$ and $d = 5.4$. It is important to note that the borders of the rods are truncated

cones as explained in [179]. The square particles, $d = 1$, are DIN 557 nuts 3.16 mm wide and 6.9 mm side.

The container is built with two glass plates separated by two stainless-steel strips 0.1 mm thicker than the particles so that the granular material is confined in a mono-layer between the plates. The bottom of the silo is flat and formed by two facing metal pieces whose edges touch each other. Since rods and squares have different sizes, we have modified the container dimensions correspondingly to generate analogous deposits. For rods (squares) the silo is 180 mm (260 mm) wide and 790 mm (950 mm) high. The number of rods necessary to fill the silo is larger than 5×10^4 and 2×10^4 for $d = 2.4$ and $d = 5.4$ mm, respectively; while the number of required squares is around 5×10^3 .

The granular sample is introduced through a hopper at the top of the silo by pouring the grains homogeneously along the whole silo width. The feed rate is measured to be around 200 particles per second for 2.4 mm rods, around 80 particles per second for 5.4 mm rods, and 70 particles per second for squares. Once the deposit is generated, an orifice is opened at the silo bottom by separating the two metal pieces that conform it. After a layer of rods (squares) of around 250 mm (300 mm) has flowed out of the silo, the outlet is closed and the flow is arrested. Then, the silo is completely emptied before a new realization is performed. The outlet size is chosen to be small enough to stay away from the silo lateral walls but big enough in order to guarantee the particle flow. At this point, we remark that the flat faces of the particles provoke jams much more frequently than in the case of the spheres [180]. Hence, the outlet sizes selected have been 80 mm, 30 mm and 80 mm for square nuts, $d = 2.4$ rods and $d = 5.4$ rods, respectively. In any case, it should be noted that, although these dimensions may slightly affect some of the quantitative values obtained in this work, the qualitative behavior remains unaltered.

A standard 10.2 megapixel camera is used to take pictures of the grains inside the silo both after the filling and after the partial discharge. The region recorded covers the whole width of the silo and a height going from 290 mm to 410 mm for the case of the rods. For the case of the squares, the height covered goes from 270 mm to 440 mm. In both cases we make sure that this

region is high enough to avoid the influence of the silo bottom. From the images, the particles are detected and their position and orientation determined. In order to obtain good statistics we have performed 100 realizations for each sample.

4.2 Model of 2D Spheropolygons

We have performed a Molecular Dynamics simulation of a two-dimensional granular system composed of non-deformable dissipative particles, confined within a rectangular box of width W . We have simulated 2×10^4 rods of $d = 2.4$ and $d = 5.4$, even so 4×10^3 squares. In order to generate deposits analogous to the experimental ones, the system width is set to $W = 180 \text{ mm}$ ($W = 172.8 \text{ mm}$) for $d = 2.4$ ($d = 5.4$) and $W = 276 \text{ mm}$ for $d = 1$. The container boundaries are composed of rigid particles, using one layer for each lateral wall, and two particle layers at the bottom.

The particles are continuously added at the top of the box with a low feed rate with random initial velocity and orientation. The granular media is deposited under the effect of gravity and it is let cool down until the particles' mean kinetic energy is several orders of magnitude smaller than its initial value. At this point, a hole of 80 mm , 36 mm and 80 mm for $d = 1$, $d = 2.4$ and $d = 5.4$ respectively, is opened at the middle-bottom of the container. The orifice is closed when a grain located at the top-middle position of the hill, marked as a reference, descends a prescribed vertical distance, s . The distance s takes the value of 300 mm for $d = 1$, 150 mm for $d = 2.4$, and 250 mm for $d = 5.4$. After closing the container we let the system to cool down again and the simulation finishes. To get good statistics, the results presented constitute averages over at least twenty-four different repetitions for each case.

For calculating the particles interaction \vec{F}_{ij} we use a very efficient algorithm proposed recently by Alonso-Marroquín et al [167, 181], allowing for simulating a large number of particles. This numerical method is based on the concept of spheropolygons, where the interaction between two contacting particles only is governed by the overlap distance between them (see details in [167, 181]). For defining the normal interaction F_{ij}^N , we use a nonlinear

Hertzian elastic force [182], proportional to the overlap distance of the particles. Moreover, to introduce dissipation, a velocity dependent viscous damping is assumed. Hence, the total normal force reads as

$$F_{ij}^N = -k^N \cdot \delta^{3/2} - \gamma^N \cdot v_{rel}^N, \quad (4.1)$$

where k^N is the spring constant in the normal direction, γ^N is the damping coefficient in the normal direction and \vec{v}_{rel}^N is the normal relative velocity between i and j . The tangential force F_{ij}^T also contains an elastic term and the tangential frictional term. Taking into account the Coulomb's constraint it reads as

$$F_{ij}^T = \min\{-k^T \cdot \xi - \gamma^T \cdot |v_{rel}^T|, \mu F_{ij}^N\}, \quad (4.2)$$

where γ^T is the damping coefficient on the tangential direction, v_{rel}^T is the tangential component of the relative contact velocity of the overlapping pair. ξ represents the elastic elongation of an imaginary spring at the contact [76], which increases as $d\xi(t)/dt = v_{rel}^T$ as long as there is an overlap between the interacting particles [76, 183]. μ accounts for the static friction coefficient of the particles.

The equations of motion are integrated using a fifth order predictor-corrector algorithm with a numerical error proportional to $(\Delta t)^6$ [44], while the kinematic tangential displacement, is updated using an Euler's method. In order to model hard particles, the maximum overlap must always be much smaller than the particle size. This is ensured by introducing appropriate values for the normal and tangential elastic constants, which are set to $\frac{k_t}{k_n} = 0.1$, $k_n = 10^6 N/m^{3/2}$. together with the gravitational acceleration $10m/s^2$. For these parameters, the time step should be around $\Delta t = 5 \times 10^{-5} s$. Although the results we will describe are generic for hard particles, to achieve quantitative comparison with experimental data we have carried out numerical simulations in which we change both the normal damping coefficient and the static friction coefficient, choosing the best fitting parameters. The damping coefficients are taken as $\frac{\nu_n}{\nu_t} = 3$, $\nu_t = 1 \times 10^2 s^{-1}$ and $\mu = 0.5$. Thus, we have ensured that the kinetic energy loss and the dynamics of sediment formation are analogous to those observed experimentally. It is important to remark that in all the simulations reported below we do not change the particle's material properties; only the

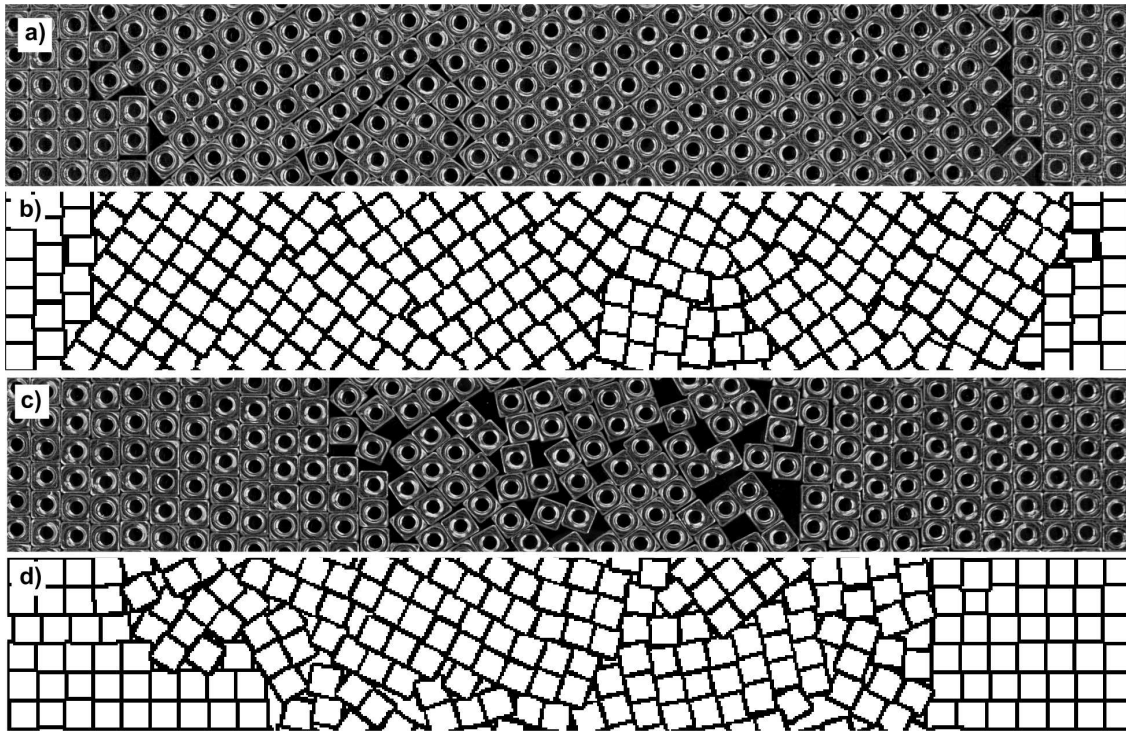


Figure 4.2: Packings of square nuts and simulated particles with $d=1$. Pictures of the experiment (a) after the silo filling and (c) after the partial discharge. Numerical graphs (b) and (d) on the same order.

particle aspect ratio has been varied.

4.3 Results

4.3.1 Packing Morphology

In [166, 179] we studied systematically the influence that the particle aspect ratio has on the micro-mechanical properties of granular packing. Figure 4.2 shows the packings obtained for square particles, $d = 1$, both experimentally and numerically. The granular columns resulting from the silo filling process are presented in Figure 4.2a (exp) and Figure 4.2c (simul). Figure 4.2a confirms experimentally the tendency of square particles to align one of their diagonals with gravity, as it was numerically predicted earlier [166].

We also describe in details the morphological and micro-mechanical changes,

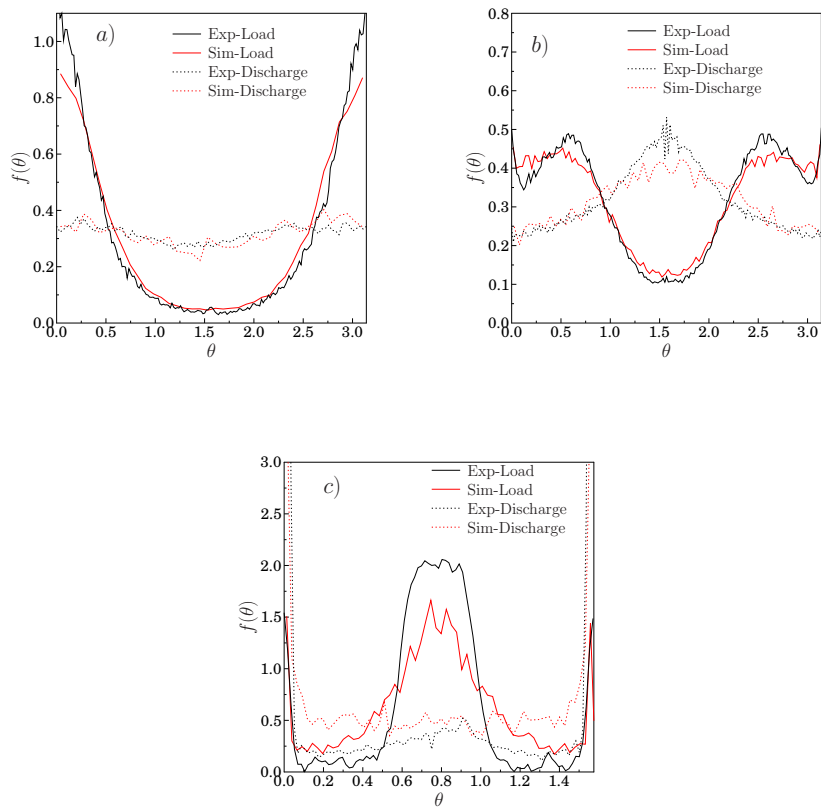


Figure 4.3: Experimental and numerical orientation distributions of particles, obtained at the end of the silo filling and after its partial discharge. We illustrate results for different aspect ratios, a) $d = 5.4$, b) $d = 2.4$ and c) $d = 1$.

which are induced by partial discharges in granular columns. The packing morphology that results at the end of the partial discharge of the silo is illustrated in Figure 4.2b (exp) and Figure 4.2d (simul). It is noticeable that during the discharge, the shear between grains induces their rotation and their settlement in more stable mechanical states. Hence, the discharge induces an alignment of the squares sides with gravity which minimizes the friction and favors their vertical displacement.

The distributions, $f(\theta)$, of the particle orientation with respect to the direction transverse to gravity are analyzed. Figure 4.3 shows the particle distributions obtained experimentally and numerically at the end of the silo filling and after the silo partial discharge for three aspect ratios, $d = 5.4, 2.4,$ and 1 (squares). The good agreement between the experimental and numerical results demonstrates the accuracy of our numerical simulation scheme. At the end of the silo filling, elongated particles have a strong preference to align horizontally (Figure 4.3a), in good agreement with previous results [184]. As the rods become less asymmetric, particles develop a most probable orientation which decreases towards $\pi/4$ for the limiting case of squares. In this case, it also becomes evident an important effect of the lateral walls which compete with gravity and lead to a strong preference for parallel ordering of squares in their vicinity. As a result, a distinct peak around $\theta = 0$ and $\theta = \pi/2$ can be also identified in Figure 4.3.c. In sphere packings an analogous wall-induced particle ordering, which can be significant in stress transmission, has been previously reported [185, 186].

The packing morphology drastically changes at the end of the partial discharge of the silo. For the case of rods (Figure 4.3a-b) the discharge induces a decrease of the number of particles oriented horizontally and an increase of the number of particles oriented vertically. This result may be a consequence of the alignment of elongated particles with the flow streamlines. The case of squares is completely different as it has been observed that they flow more easily when one of their sides is aligned with gravity. This change in the squares orientation, favored due to shearing forces with grains at rest, leads to a distribution where a single peak is clearly observed at $\theta = 0$ and $\theta = \pi/2$ (Figure 4.3c). We clarify below that this configuration minimizes the

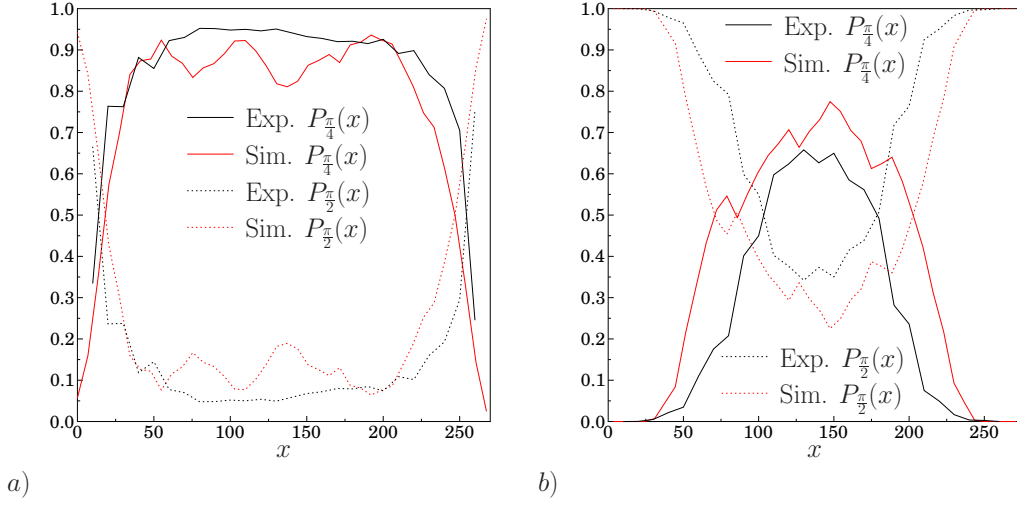


Figure 4.4: Experimental and numerical orientation of the squares for different sectors of the silo a) at the end of the silo filling and b) after the silo partial discharge. $P_{\frac{\pi}{2}}(x)$ accounts for the fraction of particles aligned mostly transversally to gravity, while $P_{\frac{\pi}{4}}(x)$ accounts for the fraction of particles mostly aligned with gravity.

friction with the lateral neighboring particles and, consequently, the stress transmission on the up-down direction is favored.

Although in the previous paragraphs we have analyzed the particle orientation distribution by considering all the particles along the whole silo width, it should be remarked that the partial silo discharge induces a spatial inhomogeneity in the horizontal direction. This effect is observed for all the aspect ratios but it is specially dramatic for the case of squares. In Figure 4.4 we quantify the internal structure analyzing the fraction of square particles which align their side (diagonal) with gravity, at angles $0 < \theta < \pi/8$ and $\theta > \pi - \pi/8$ ($\pi/4 - \pi/8 < \theta < \pi/4 + \pi/8$), as a function to the distance to the left parallel wall of the silo, $P_{\frac{\pi}{2}}(x)$ ($P_{\frac{\pi}{4}}(x)$). At the end of the filling process, most particles align their diagonals with gravity, except for a narrow region close to the walls. After the partial discharge, it is evident that the fraction of squares with a diagonal parallel to gravity is strongly depleted from the wall region, while in the center, both groups of orientations are present with similar probability. This result reflects what is observed by visual inspection of the discharge process: a column of particles, limited by the orifice size, flows out the central part of the silo. In the regions closer to the lateral walls the strong friction

between the moving particles and those at rest favors the growth of clusters of squares with their sides aligned with the walls. This kind of flow is known as ratholing, a characteristic and undesirable effect in silo discharge, where stagnant zones are developed near the walls as only the particles above the silo outlet are able to flow out [185].

4.3.2 Micromechanics

The study of the micromechanical properties of the granular packings will provide more insight in the correlation between the deposit microstructure and stress transmission. We can define the stress acting on a single particle i in terms of \mathbf{F}_i^c , the force it experiences due to its contact c . The local stress tensor can be calculated as

$$\sigma_{\alpha\beta}^i = \sum_{c=1}^{C_i} l_{i,\alpha}^c F_{i,\beta}^c, \quad (4.3)$$

where l_i^c is the branch vector related to the contact c . The sum runs over all contacts of particle i .

Figure 4.5 displays polar distributions of the stress tensor principal directions obtained for single particles (see Equation 4.3). We present results corresponding to columns of rods with $d = 5.4$ (a and b), and squares (c and d), after loading (a and c) and after partial discharging (b and c). The data shown correspond to an area of 100 mm wide at the center of the silo. In each plot, the discontinuous arrows represent the largest (σ_{11}) and smallest (σ_{22}) eigenvalue of the mean stress tensor, within the whole studied area. The size of the arrows is normalized with the size of the smallest eigenvalue. Note that at the end of the silo filling process, the polar distribution for rods $d = 5.4$ displays a strong preference for the transmission parallel to gravity (Figure 4.5a). On the contrary, for squares, a clear symmetry is found in the distributions of the two stress eigenvalues, evidencing that forces are mainly transmitted along the $\pi/4$ and $3\pi/4$ directions (Figure 4.5c). At the end of the partial discharge, elongated rods keep the preference for vertical stress transmission, although the stronger disorder in rod alignment favors a more isotropic stress distribution, leading to broader distributions of the stress eigenvalues (Figure 4.5b).

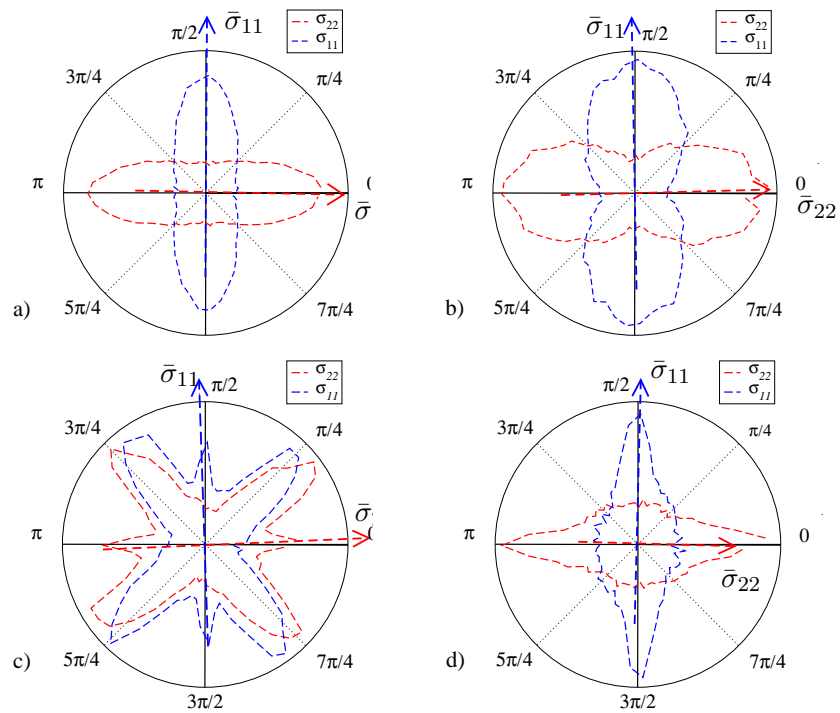


Figure 4.5: Polar distribution of the principal directions of the *local stress* for elongated particles with aspect ratio $d = 5.4$ (a) after the silo load and (b) after the partial discharge. The same results for squares (c) after the load and (d) after the partial discharge.

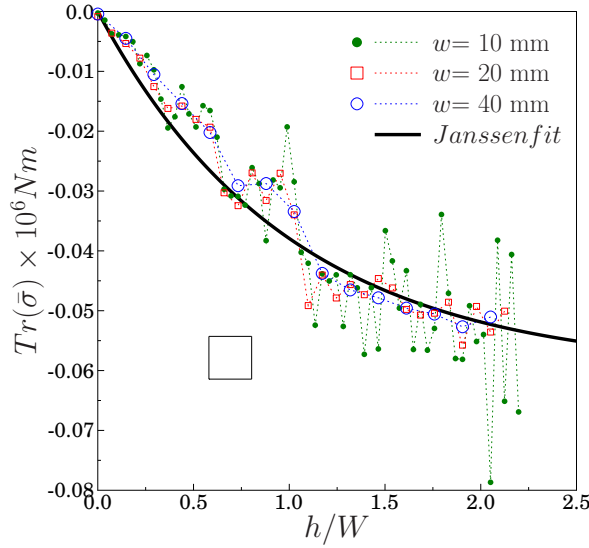


Figure 4.6: Profiles of the trace of the mean stress tensor, defined following Equation 4.4, after the silo loading. The results have been obtained using a Gaussian coarse grained function, $\phi(\mathbf{r}) = \frac{1}{\pi w^2} e^{-(|\mathbf{r}|/w)^2}$ and several values of w . In all cases the depth h is expressed in units of the silo width. We also show the Janssen type fitting to the equation $\sigma = \sigma_m(1 - \exp(-x/h_s))$, we have used $[\sigma_m = -0.06 \times 10^6 Nm; h_s = 1.0]$.

For the case of the squares, the changes in the stress transmission induced by the particle flow are more important. Indeed, after the partial discharge, the stress changes dramatically and becomes mainly transmitted vertically (Figure 4.5d). This effect correlates with the formation of big clusters of square particles aligned with the walls. Hence, changes in the particle orientation induced by the shear affect the microstructure and determine the stress transmission among the faceted particles.

The notable changes in the local stress produced by the partial discharge of the silo necessary lead to significant variations in the pressure profiles obtained as a function of the silo depth (h). To properly describe these variations, we examined the mean local stress tensor through the granular column. Professor Isaac Goldhirsch and coworkers [187, 188] have recently introduced a very elaborated definition of mean stress field $\bar{\sigma}_{\alpha\beta}$. Following their approach

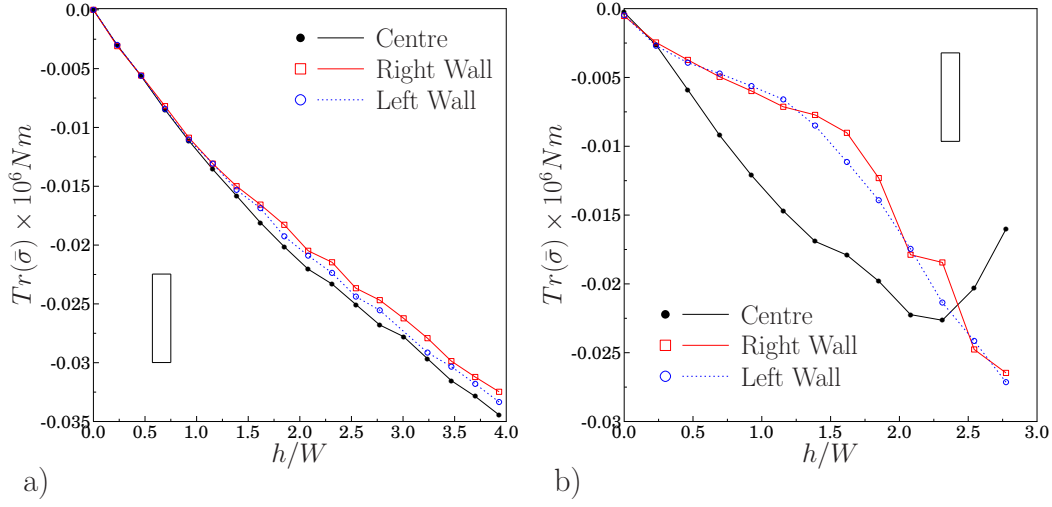


Figure 4.7: Profiles of the trace of the mean stress tensor (pressure) after the load a) and the partial discharge b) for rods with $d = 5.4$. In all cases the depth h is expressed in units of the silo width.

the stress $\sigma_{\alpha\beta}(\mathbf{r})$ at point \mathbf{r} , is given by the expression

$$\bar{\sigma}_{\alpha\beta}(\vec{r}) = \frac{1}{2} \sum_{i,j;i \neq j} f_{ij\alpha} r_{ij\beta} \int_0^1 ds \phi[\vec{r} - \vec{r}_i + s\vec{r}_{ij}], \quad (4.4)$$

where the sum runs over all the contacting particles i, j , whose center of mass are at \vec{r}_i and \vec{r}_j , respectively. Moreover, f_{ij} accounts for the force exerted by particle j on particle i and $\vec{r}_{ij} \equiv \vec{r}_i - \vec{r}_j$. The coarse grained (CG) function, $\phi(\vec{R})$, is positive semidefinite normalized function, with a single maximum at $\mathbf{R} = 0$. In our case, we used a Gaussian coarse function, $\phi(\mathbf{r}) = \frac{1}{\pi w^2} e^{-(|\mathbf{r}|/w)^2}$, where the sign convention is that compressive stress is negative. The value of w defines the coarse grained scale. We note that the data was also evaluated using less sophisticated mean stress definitions [189, 190] and very similar results came out (data not shown).

To clarify the effect of the CG scale w on the results, we evaluate the numerical data for several values of w . The stress tensor components –defined by Equation 4.4– were calculated within specific areas and the contribution of the contacts within the selected area is weighted by the function $\phi(\mathbf{r})$. Hence, the size of the working area is controlled by the size of the CG scale w . Specifically, the trace of stress tensor (pressure) obtained for a silo of squares was

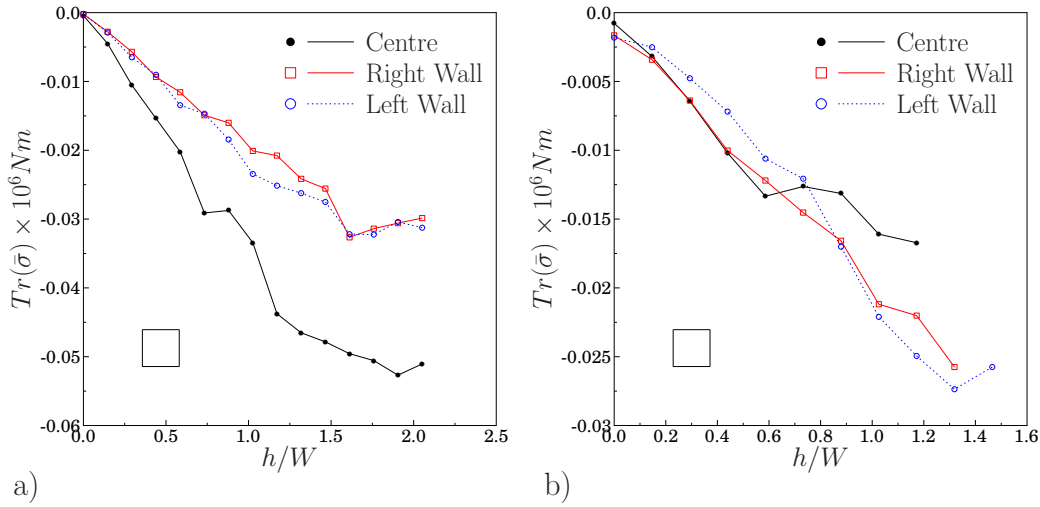


Figure 4.8: Profiles of the trace of the mean stress tensor (pressure) after the load a) and the partial discharge b) for squares. In all cases the depth h is expressed in units of the silo width.

examined in Figure 4.6. Note that the depth of the silo has been normalized with the width of the deposit $x = h/W$. Moreover, for comparison, the numerical fit using a *Janssen-type* formula $\sigma = \sigma_m(1 - \exp(-x/h_s))$, are also shown [191, 192].

Here, the magnitude of σ_m represents the saturation stress and h_s indicates the characteristic value of depth at which the pressure on the column surface stabilizes. The pressure profiles were calculated fixing the horizontal coordinate and varying the vertical one (up-down) in units of w . The results reveal that stress fluctuations at fixed *depth* vanish when increasing the value of w . This indicates the existence of a *CG* scale for which the stress tensor field is resolution independent [187, 188]. The data presented below have been carefully evaluated for different values of w . Provided that the stress profiles are not homogeneous due to the action of the gravity field, we have carefully chosen the value of w to accurately capture the spatial stress variation.

In Figures 4.7 and 4.8, we display the trace of the mean stress tensor for rods $d = 5.4$ and squares, respectively. In all cases, a coarse grained distance of $w = 40\text{mm}$ was used for the calculation of the mean stress tensor. This value is approximately six and seven times larger than particle size of the squares and the rods of $d = 5.4$, respectively. As we pointed out earlier, after the silo

loading with elongated particles, the stress is transmitted preferentially parallel to gravity. As a result, the weak stress transmission on the horizontal direction hinders pressure saturation, which is not completely reached for the system sizes studied here (Figure 4.7a). The pressure profiles are very similar both in the center of the column and in the region close to the walls. After the partial discharge (Figure 4.7b), notable modifications are induced on the trace of the mean stress tensor. On the center of the silo, the larger disorder in particle orientation enhances the stress transmission in the horizontal direction which is typically associated to pressure saturation. Effectively, when we approach to the bottom of the silo the pressure first reaches a maximum and then, it decreases at the very bottom. This pressure reduction denotes arch formation in the region near the outlet. In the region close to the walls the pressure increases with h until the bottom of the silo, probably due to horizontal rod alignment induced by the bottom.

For squares (Figure 4.8a), the opposite scenario holds true. After filling the silo, in the central part of the column the force is transmitted preferentially at $\pi/4$ with respect to gravity, providing an efficient mechanism to channel stresses towards the lateral walls. Accordingly, a saturation in the pressure profile seems to be observed. However, close to the walls the strong face to face interaction induces the particle alignment and, consequently, a linear pressure profile is developed. The scenario is altered by the discharge of the square nuts which become preferentially aligned with the silo walls even in the center part of the column. This vertical alignment results in a stress transfer to the bottom of the silo which makes pressure saturation hardly visible.

4.4 Conclusions

In this work we have shown that the partial discharge of a silo filled with faceted grains has a profound effect on the deposit morphology and its stress distribution. During the discharge, the shear between grains induces their rotation and their settlement in more disordered arrangements. For elongated particles, the preferred horizontal orientation displayed after the silo filling disappears. For square particles, the discharge provokes an alignment

of their sides with gravity which minimizes the friction and favors their vertical displacement. Such a structure leads to ratholing, a flow pattern which is typically associated to cohesive effects, but that here, we show that it can also be induced by the geometrical properties of the particles.

As a result of the changes in particle orientation, the pressure distribution in the silo changes qualitatively; while for elongated rods lateral stress transmission is promoted by the enhanced disorder leading to a faster pressure saturation, the opposite holds for squares. In this latter case the alignment of squares induced by the flow destroys the initial force chain network which is replaced by a mainly vertical stress transmission. As a consequence, a significant reduction of the pressure saturation effect is observed.

With the results reported here, we attempt to clarify the performance and stability of silos, which need to support high stresses that become very sensitive to grain shapes and the silo steering history. If we increase the amount of material flowing out of the silo, or induce a second discharge, we expect that the observed effect will be enhanced. Although we have focused on weakly disordered initial deposits, due to the low feeding rates used to fill the silo, the main features discussed here are expected for other silo filling procedures. Perhaps, increasing the disorder of the initial packing will generically decrease the relative magnitude of the changes discussed.

Chapter 5

Granular packings of cohesive elongated particles

Very often, loose and disordered granular structures appear in many technological processes and even everyday life. They can be found in collapsing soils [193–196], fine powders [197–199] or complex fluids [200, 201]. Generally, those fragile grain networks are correlated with the presence of cohesive forces [197, 202–204]. Typical fine powders have in most cases an effective attractive force, e.g. due to a capillary bridge between the particles or van der Waals forces (important when going to very small grains, e.g. nano-particles). This force is known to be of great importance, e.g. for the mechanical behavior and the porosity of the macroscopic material [205–208]. This cohesive force leads also to the formation of loose and fragile granular packings as investigated in detail for structures generated by successive deposition of spherical grains under the effect of gravity [202, 203, 205, 209].

The main objective of this chapter is to clarify the effect that an effective attractive force has on the packing properties of elongated grains. Here we focus on packings generated by deposition under gravity.

5.1 2D spheropolygons with cohesion

We have performed Discrete Element Modeling of a two-dimensional granular system composed of non-deformable oval particles, i.e. spheropolygons

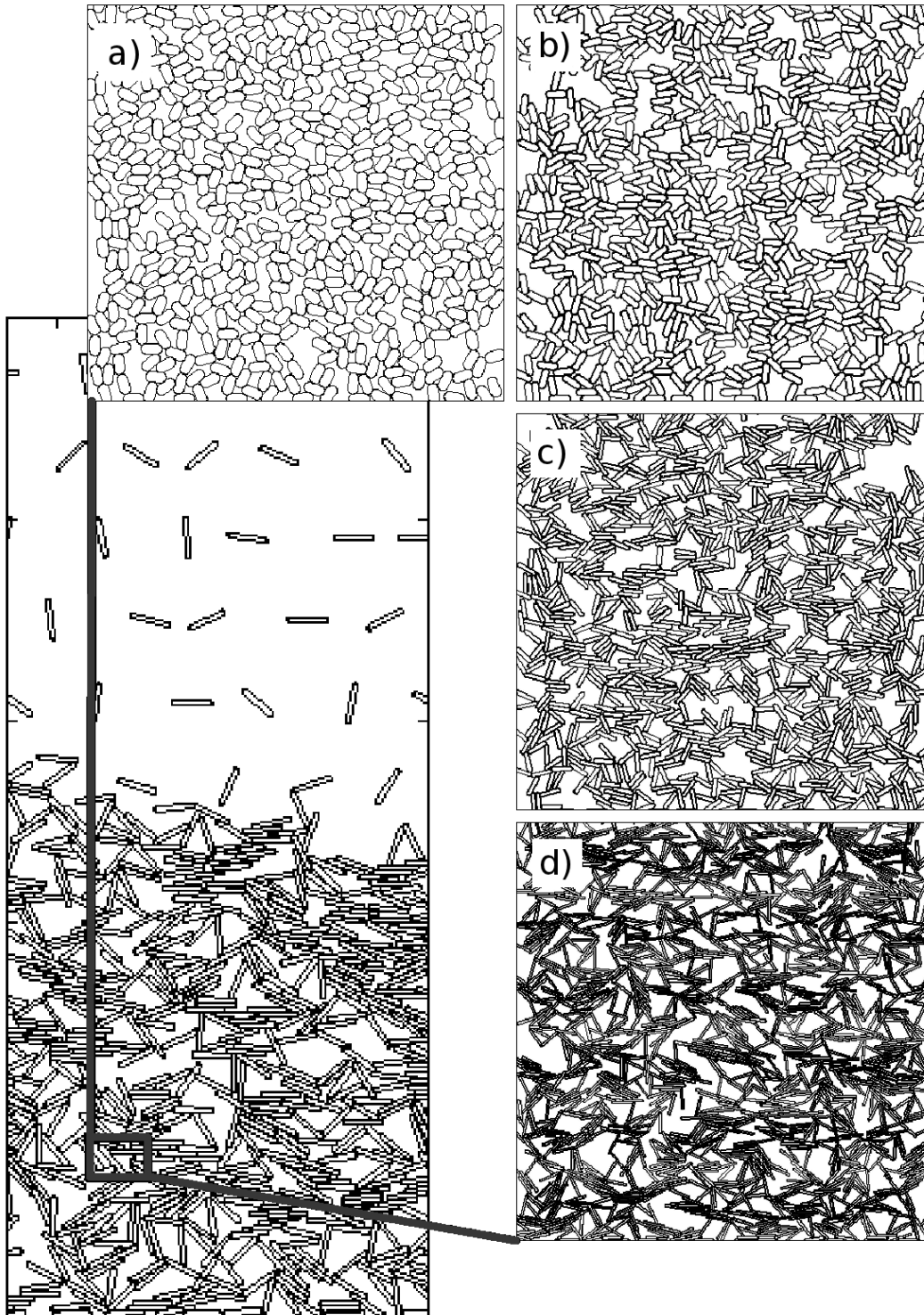


Figure 5.1: Simulated packings of elongated cohesive particles settled by gravity. Final configurations are shown for the same granular bond number $Bo_g = 10^4$ and increasing elongation: (a) $d = 2$, (b) $d = 3$, (c) $d = 5$ and (d) $d = 10$.

[167, 181] composed of two lines of equal length and two half circles of same diameter. The width of a particle is the smaller diameter, given by the distance between the two lines (equals the circle diameter), whereas the length is the maximum extension. The aspect ratio d is defined by the length divided by width. This system is confined within a rectangular box of width W . Its lateral boundaries as well as the bottom are each built of one very long spheropolygonal particle, which is fixed. In order to generate analogous deposits, the system width is always set to $W = 20 \times d$ (in units of particle width). As illustrated in Figure 5.1 the particles are continuously added at the top of the box with very low feed rate and a random initial velocity and orientation. The granular system settles under the effect of gravity and is relaxed until the particles' mean kinetic energy is several orders of magnitude smaller than its initial value.

For calculating the particles' interaction \vec{F}_{ij} we use a very efficient algorithm proposed recently by Alonso-Marroquín et al [167, 181], allowing for simulating a large number of particles. This numerical method is based on the concept of spheropolygons, where the interaction between two contacting particles only is governed by the overlap distance between them (see details in References [167, 181]).

To define the normal interaction F_{ij}^N , we use a nonlinear Hertzian elastic force [182], proportional to the overlap distance δ of the particles. Moreover, to introduce dissipation, a velocity dependent viscous damping is assumed. Hence, the total normal force reads as $F_{ij}^N = -k^N \cdot \delta^{3/2} - \gamma^N \cdot v_{rel}^N$, where k^N is the spring constant in the normal direction, γ^N is the damping coefficient in the normal direction and v_{rel}^N is the normal relative velocity between i and j . The tangential force F_{ij}^T also contains an elastic term and a tangential frictional term accounting also for static friction between the grains. Taking into account Coulomb's friction law it reads as, $F_{ij}^T = \min\{-k^T \cdot \xi - \gamma^T \cdot |v_{rel}^T|, \mu F_{ij}^N\}$, where γ^T is the damping coefficient in tangential direction, v_{rel}^T is the tangential component of the relative contact velocity of the overlapping pair. ξ represents the elastic elongation of an imaginary spring with spring constant k^T at the contact [76], which increases as $d\xi(t)/dt = v_{rel}^T$ as long as there is an overlap between the interacting particles [76, 183]. μ is the friction coefficient

of the particles.

Additionally, here we consider bonding between two particles in terms of a cohesion model with a constant attractive force F_c acting within a finite range d_c . Hence, it is expected that the density and the characteristics of the density profiles are determined by the ratio between the cohesive force F_c and gravity $F_g = mg$, typically defined as the granular Bond number $Bo_g = F_c/F_g$. Thus, the case of $Bo_g = 0$ corresponds to the cohesion-less case whereas for $Bo_g \rightarrow \infty$ gravity is negligible.

The equations of motion, Equations (1.5-3.1) are integrated using a fifth order predictor-corrector algorithm with a numerical error proportional to $(\Delta t)^6$ [44], while the kinematic tangential displacement, is updated using an Euler's method. In order to model hard particles, the maximum overlap must always be much smaller than the particle size; this is ensured by introducing values for normal and tangential elastic constants, $k^T/k^N = 0.1$, $k^N = 10^3 N/m^{3/2}$. The ratio between normal and tangential damping coefficients is taken as $\gamma^N/\gamma^T = 3$, $\gamma^T = 1 \times 10^2 s^{-1}$ while gravity is set to $g = 10 m/s^2$ and the cohesion range to $d_c = 0.0001$ (in units of particle width) to account for a very short range attraction, as mediated, e.g. by capillary bridges or van der Waals force. For these parameters, the time step should be around $\Delta t = 5 \times 10^{-6} s$.

In all the simulations reported here, we have kept the previous set of parameters and only the particle aspect ratio and the Bond number Bo_g have been modified. We have also carried out additional runs (data not shown) using other particles' parameters, and we have verified that the trends and properties of the quantities we subsequently analyze are robust to such changes.

5.2 Results and discussion

We systematically study granular deposits of particles with aspect ratio from $d = 2$ to $d = 10$ and different Bond numbers. In all simulations presented here we have used 6×10^3 rods. In Figure 5.1 we illustrate the granular packings obtained for several particle shapes and constant Bond number $Bo_g = 10^4$. Despite of the presence of a gravity field acting downwards, the formation of very loose and disordered granular structures is very noticeable. Moreover, as the

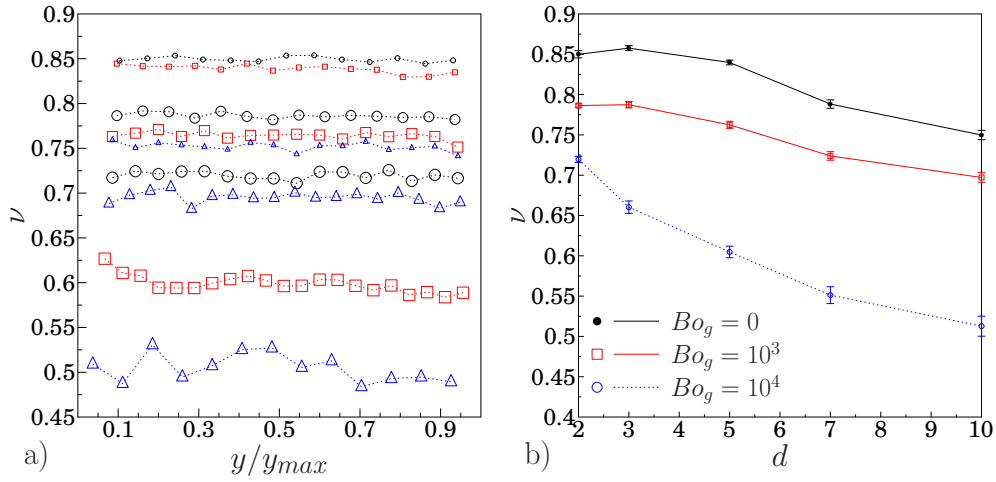


Figure 5.2: Density profiles of different granular deposits. In a) the circles represent particles with $d = 2$, the squares $d = 5$ and the triangles $d = 10$. The larger the symbols the stronger is the attractive force (small: $Bo_g = 0$; medium: $Bo_g = 10^3$; large: $Bo_g = 10^4$). In b) the evolution of the average volume fraction as a function of d is shown.

aspect ratio of the particles increases, the volume fraction of the column decreases, showing a tendency to the formation of more disordered structures. This result contrasts with what was obtained for non-cohesive elongated particles. In that case, the topology of the packing is dominated by the face to face interaction and the formation of ordered structures of aligned rods is detected [166, 210].

For better describing the packing structure, in Figure 5.2a we present the density profiles depending on depth y/y_{max} obtained for several deposits of elongated particles. We plot for each particle aspect ratio density profiles with increasing strength of the attractive force illustrated in Figure 5.2a by increasing symbol size. In systems composed by elongated particles with strong attractive forces the formation of extremely loose structures is observed, which are stabilized by the cohesive forces [209]. Moreover, in all cases the density profiles are quite uniform as function of depth. Typically, for the non-cohesive case a close packing is expected. For cohesive particles, smaller volume fraction values are found and the density profiles remain constant with depth. These density profiles have been studied and analyzed extensively for spherical particles [209] where constant density has been found only for fast deposi-

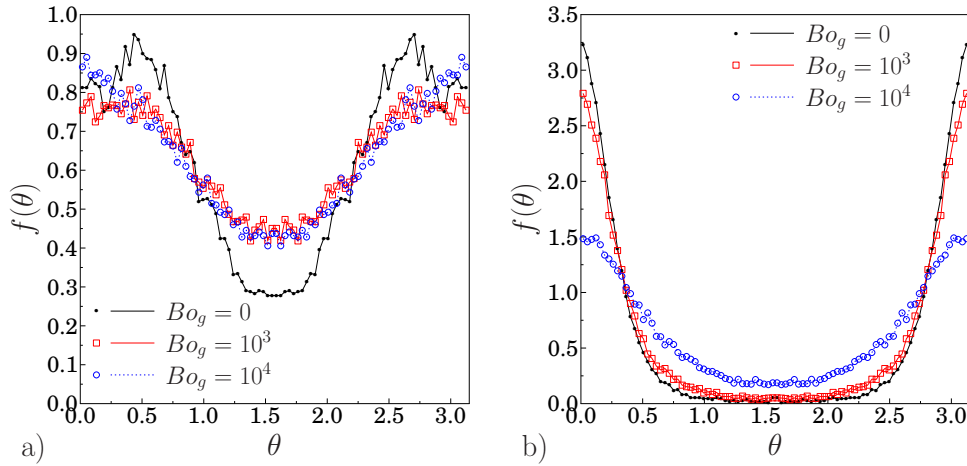


Figure 5.3: Orientation distributions of particles for two aspect ratios, a) $d = 2$ and b) $d = 10$. In each case, results for several bond numbers are presented.

tion as strongly influenced by inertia. However, an extremely slow and gentle deposition process, allowing for relaxation of the deposit due to its own weight after each deposition, leads to a decreasing density with vertical position. Obviously, here the feed rate is not sufficiently slow. Additionally, as particles are added at the top they are accelerated before, thus reaching the deposit with a non negligible impact velocity.

Complementary, in Figure 5.2b a systematic study of the global volume fraction depending on the particle aspect ratio is presented for different bond numbers. All curves show the overall trend of decreasing density with increasing aspect ratio d . For packings of non-cohesive particles disordered and thus substantially looser structures can only be found with very large aspect ratio as found earlier numerically and experimentally [166, 179]. For very cohesive particles (see Figure 5.1), however, loose and disordered granular structures can be easily stabilized, leading to much lower densities independent on shape/elongation. This is notably enhanced as the aspect ratio of the particles increases and, consequently, the volume fraction of the packings quickly decreases.

In order to characterize the packing morphology, we examine the orientations of the particles. In Figure 5.3, the distributions of particle's orientation

$f(\theta)$, with respect to the horizontal direction, for rods with aspect ratio $d = 2$ and $d = 10$ are illustrated. We present results for several bond numbers. First, for the non-cohesive case, the geometry of the particle dominates the final structures of the compacted piles. Note that at the end of the deposition process, long particles ($d = 10$) most probably lie parallel to the substrate ($\theta = 0$ and $\theta = \pi$), while the most unlikely position corresponds to standing rods ($\theta = \frac{\pi}{2}$). Nevertheless, as the aspect ratio decreases, there is a shift in the most probable orientation, leading to a peaked distribution at an intermediate orientation [166, 179]. Furthermore, this shift of the maximum is not observed for highly cohesive particles. In general, as the strength of the attractive force gets stronger, the final packing tends to a flatter distribution. As we pointed out earlier, very elongated particles with strong attractive forces form extremely loose structures. As the aspect ratio gets higher, the rods form highly jammed and disordered networks because during the deposition local particle rearrangements are constrained by the attractive force. The latter, is corroborated by the distribution of the angular orientation, where now the probability for standing rods which was zero in the non-cohesive case is enhanced with increasing bond number (Figure 5.3b). It seems that, for sufficiently large aspect ratio d , there is a threshold bond number needed to have a non-zero probability for standing rods.

The packing morphology is also examined through a radial orientation function $Q(r)$, defined as

$$Q(r) = \langle \cos(2(\theta_i - \theta_j))\delta(\mathbf{r}_{ij} - r) \rangle \quad (5.1)$$

where θ_i and θ_j are the angular orientations of particles i and j , respectively. $Q(r)$ accounts for the mean value of the angular correlation between a given particle i and a particle j with their center of mass at a distance r_{ij} . Note that, this distribution function provides useful quantitative information on the local morphology of the rod packings. Configurations where the two rods are perpendicular to each other contribute -1 to $Q(r)$, while rods aligned along their long faces or along their short faces contribute with 1 [166, 179].

In Figure 5.4a and Figure 5.4b the numerical data for packing of cohesive particles with aspect ratio $d = 2$ and $d = 5$ are shown for comparison. Both figures show a series of maxima (parallel alignment) and minima (perpendicular

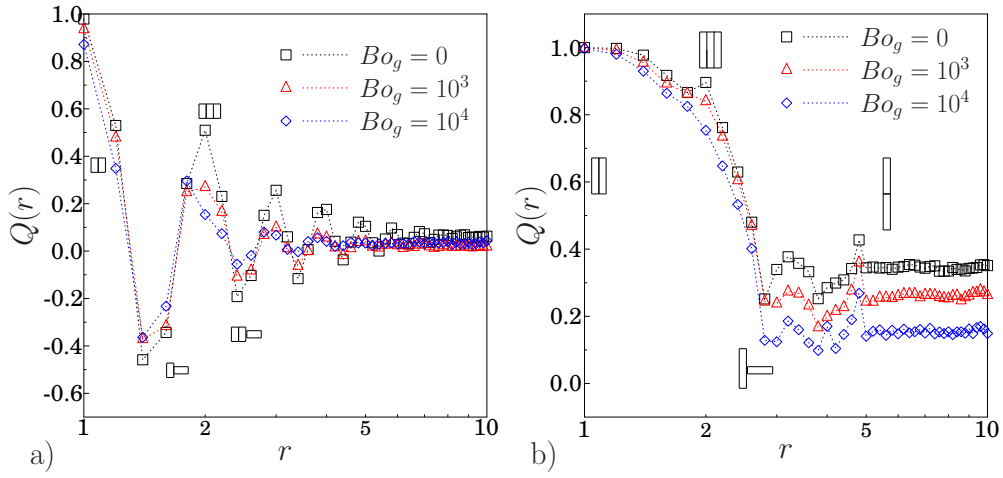


Figure 5.4: Radial orientation distribution functions, $Q(r)$, as defined in Equation 5.1 for rod deposits with two different aspect ratios, a) $d = 2$ and b) $d = 5$. In each case, results for several Bond numbers are presented. At specific maxima/minima the corresponding particle configurations are illustrated.

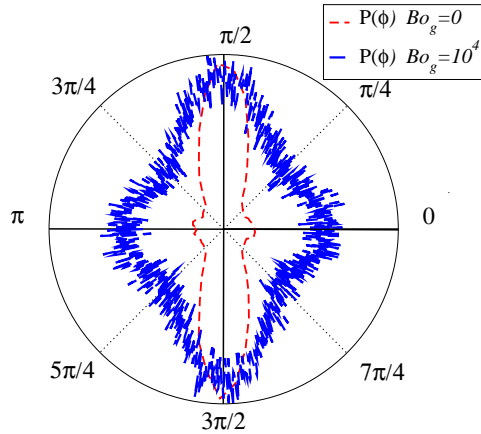


Figure 5.5: Polar distribution of the principal direction (larger eigenvalue of the stress tensor for each particle $\sigma_{\alpha\beta}$), obtained for particles with $d = 10$. For comparison, the data for $Bo_g = 0$ and $Bo_g = 10^4$ is presented.

alignment), which develop at several distances. This correlates with the high tendency of the particles to align in closely packed structures, in particular for low attractive force strengths and the limiting case of non-cohesive particles [166, 179]. As the strength of the interaction force gets larger looser structures are formed and consequently the intensity of the maxima and minima decreases. On the other hand, for very elongated particles (see Figure 5.4.b) $Q(r)$ clearly indicates that the system does not show significant order. There is a maximum at contact, which simply indicates that at this shortest distance only perfectly aligned particles along their long faces can contribute. At larger distances a deep plateau seems to indicate a small preference at these intermediate distances to observed parallel aligned particles. Only a characteristic peak corresponding to the contact through the particle length $r = d$ seems to remain even for very strong attractive strengths. This picture suggests the lack of significant order and presence of strong density inhomogeneities, in granular deposits of very cohesive particles. As aspect ratio gets higher, this effect is notably enhanced.

Furthermore, we can correlate the microstructure with stress transmission by studying the micro-mechanical properties of the granular deposits. To this end, we introduce the stress tensor of a single particle i ,

$$\sigma_{\alpha\beta}^i = \sum_{c=1}^{C_i} l_{i,\alpha}^c F_{i,\beta}^c, \quad (5.2)$$

which is defined in terms of the total contact force \vec{F}_i^c that particle i experiences at contact c and the branch vector \vec{l}_i^c related to the contact c . The sum runs over all the contacts C_i of particle i , α, β are the vectorial components.

In Figure 5.5, the polar distribution $P(\phi)$ of the principal direction ϕ related to the larger eigenvalue of $\sigma_{\alpha\beta}$, obtained for particles with aspect ratio $d = 10$ is illustrated. For the non-cohesive case ($Bo_g = 0$), Figure 5.5 indicates that forces are preferentially transmitted in the vertical direction, displaying a high degree of alignment with the external gravity field. Note, that the stress is dominated by the contribution parallel to gravity (σ_{11}) whose mean value (data not shown) is also much higher than the stress in the horizontal direction (σ_{22}). For very cohesive particles (see Figure 5.5), however, the polar distribution of the principal direction is more uniform, denoting the establishment of a more

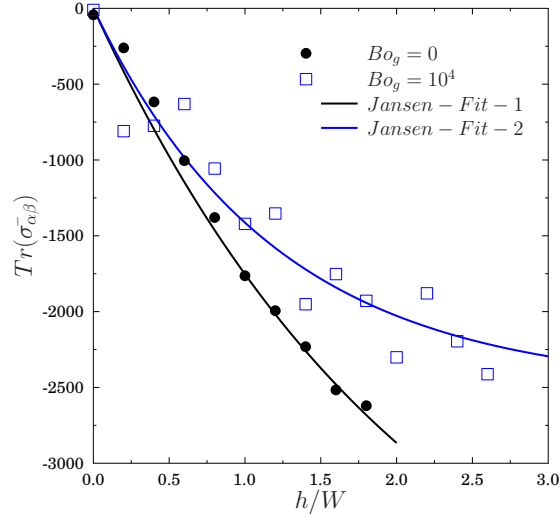


Figure 5.6: Profiles of the trace of the mean stress tensor, obtained for particles with $d = 10$ and two different bond numbers. The depth is normalized with the width W of the system. We also show the fitting to the equation $\sigma = \sigma_m(1 - \exp(-x/h_s))$, where we used $[\sigma_m = 2500N/m; h_s/W = 1.2]$ and $[\sigma_m = 4800N/m; h_s/W = 2.2]$ for case 1 and 2, respectively.

spherical stress state. Hence, in this case the stress is more isotropically transmitted while the alignment with the external gravity field diminishes. This effect correlates with the formation of very loose packings and the lack of significant order and the presence of strong density inhomogeneities.

Finally, we show that the changes in microstructure induced both by particle geometry and the attractive force lead to significant modifications in the pressure (trace of the mean stress tensor) profiles as a function of the silo depth h . The mean stress tensor, $\bar{\sigma}_{\alpha\beta}$, can be calculated for a given representative volume element (RVE) with area A_{RVE} resulting in

$$\bar{\sigma}_{\alpha\beta} = \frac{1}{A_{\text{RVE}}} \sum_{i=1}^N w_v \sigma_{\alpha\beta}^i. \quad (5.3)$$

The sum runs over the representative volume element while w_v is an appropriate average weight. Although recently Professor Isaac Goldhirsch and coworkers have developed a very accurate procedure for calculating w_v and $\bar{\sigma}_{\alpha\beta}$ [188, 211], for simplicity's sake we use particle-center averaging and choose the simplest weighting: $w_v = 1$ if the center of the particle lies inside the

averaging area A_{RVE} and $w_v = 0$ otherwise [189, 190].

In Figure 5.6, we display the trace of the mean stress tensor, defined following Equation 5.3, for elongated particles with $d = 10$. For the calculation of the mean stress tensor we have used a representative volume element with a size equivalent to five particle lengths $A_{\text{RVE}} = 5d \times 5d$. The depth has been normalized with the width of the deposit $x = h/W$. Moreover, for comparison, the numerical fit using a *Janssen-type* formula $\sigma = \sigma_m(1 - \exp(-x/h_s))$, are also shown. Here, the magnitude of σ_m represents the saturation stress and h_s indicates the characteristic value of depth at which the pressure in the deposit stabilizes.

As we have mentioned earlier, non-cohesive elongated particles transmit stress preferentially parallel to gravity. As a result, the weak transmission to the lateral walls weakens pressure saturation (Figure 5.6), which is reflected by the large saturation depth h_s and stress σ_m . The latter is consequence of the horizontal alignment of the flat faces of the rods, which induces an anisotropic stress transmission, from top to bottom. However, the scenario changes drastically for very cohesive particles. As we also pointed out earlier, when the attractive force is increased, particle orientations deviate from the horizontal and a larger disorder in the particle orientation distribution shows up. As a result, the spherical component of the local stress is notably enhanced with respect to the deviatoric part, which is related to the gravity direction. Hence, for very cohesive particles $B_o = 10^4$ of $d = 10$ we found notably smaller values of saturation depth h_s and stress σ_m . In this respect, introducing an attractive force has a very similar effect as reducing the particle elongation.

5.3 Conclusions

We have shown that introducing an attractive force in deposits of elongated grains has a profound effect on the deposit morphology and its stress profiles. In deposits of non-cohesive particles the topology is dominated by the formation of ordered structures of aligned rods. Elongated particles tend to align horizontally and the stress is mainly transmitted from top to bottom, revealing an asymmetric distribution of the local stress. Lateral force transmission

becomes less favored compared to vertical transfer, thus hindering pressure saturation with depth. For deposits of cohesive particles, the preferred horizontal orientation is less pronounced with increasing cohesion. Very elongated particles with strong attractive forces form extremely loose structures, characterized by orientation distributions, which tend to a uniform behavior when increasing the Bond number. As a result of these changes, the pressure distribution in the deposits changes qualitatively. The spherical component of the local stress is notably enhanced with respect to the deviatoric part. Hence, the lateral stress transmission is promoted by the enhanced disorder and it leads to a faster pressure saturation with depth.

Chapter 6

CUDA

Nowadays, molecular dynamics is widely accepted as an effective method for addressing physical and engineering issues concerning dense granular media. This method is generally distinguished by the inclusion of several degrees-of-freedom as well as state-full contact. Moreover, it is also suitable for describing complicated particle shapes (non-sphericity) and polydisperse systems.

Nevertheless, the main disadvantages of molecular dynamics algorithms, implemented on computing processing units (CPU), are the maximum number of particles and the computing time of a virtual simulation. Those factors are usually limited by the *CPU* speeds and memory capacities. Thus, the contemporary molecular dynamics simulations on large cluster of CPU computing resources are still not able to handle typical technological process where flows contain billions of particles.

On the other hand, the main disadvantages of the parallel computing reside in the cost of the hardware required to implement it. In today's scenario, with the introduction of multicores processors, it is possible to run applications in parallel on personal computers (PC). However, the processor of a PC is a general-purpose processor (CPU), and even when it is able to perform millions of operations per second, it is not that good working with large volumes of data. Graphics processing unit (GPU), however, are designed to rapidly manipulate and alter memory. Moreover, their highly parallel structure makes them more effective than general-purpose CPUs for algorithms where processing of large blocks of data is done in parallel. Thus, general-purpose computa-

tion on graphics hardware (GPGPU) [97–99] has currently become a serious alternative for parallel computing on desktop computers.

The NVIDIA GPU Computing SDK provides hundreds of code samples, white papers, to help you get started on the path of writing software with CUDA C/C++, OpenCL or DirectCompute [212]. Specifically, the example called *particles-CUDA* is a simple system, which includes discrete elements that move and collide within an uniform grid data structure [213]. However, as they say *"The accompanying code is intended to provide a framework to which more complicated particle interactions such as smoothed particle hydrodynamics or soft body simulation can be added (...) The code included in this sample is by no means optimal and there are many possible further optimizations to this algorithm"* [212]. Given our previous experience programming on NVIDIA's parallel computing architecture, this chapter concerns CUDA-NVIDIA programming. We present below some results in molecular dynamics simulation of granular media on Graphics Processing Units (GPUs).

6.1 GPGPU vs CPU benchmark

First, in order to compare the runtime difference between typical MD-algorithms and hybrid CPU-GPU MD-algorithms, two versions of a simple MD-algorithm have been implemented. A 3D dimensional mono-disperse granular gas was used as model example. The first version of the code is a hybrid CPU-GPU algorithm, which uses the GPU to calculate the interaction between particles (*particles-CUDA* with periodic boundary conditions), whilst the second version fully runs on the CPU. The performance of a particle simulation code is measured by the Cundall number defined as

$$C = N_T N / T_{CPU} \quad (6.1)$$

where N_T is the number of time steps, N is the number of particles and T_{CPU} is the length in time of the simulation.

The CPU version benchmark was performed in a personal computer running Debian GNU/Linux 6.0.2 (squeeze), with a processor Intel® Core™ 2 Quad Q6600 at 2.40 GHz. In the case of the GPU version, the benchmark

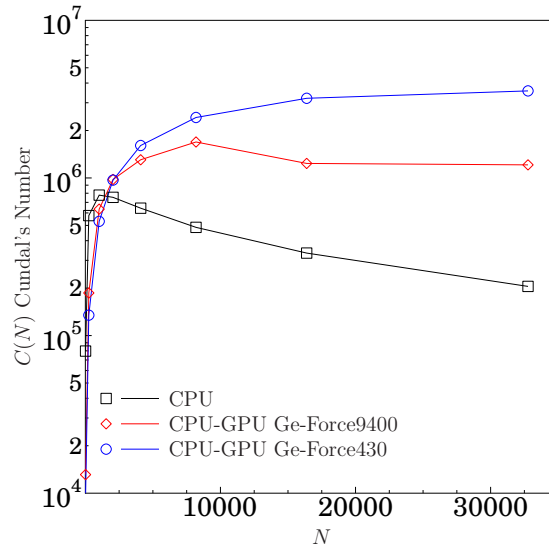


Figure 6.1: Cundall number against N for different simulations. In black color a version that run only on the CPU. In red and blue hybrids versions. When the number of particles is relatively small the Cundall number is approximately constant. However, as the system size gets larger the hybrid version notable enhanced respect to the ones only runs on CPU.

was performed in the same PC with an NVIDIA® GeForce® GT 430 graphic card, and in an Apple MacBook Pro® with a processor Intel® Core™ 2 Duo at $2.53GHz$ and a graphic card NVIDIA® GeForce® 9400M. In all cases the mean value for 10 different executions –1000000 iterations each one– are presented. The results obtained are shown in Figure 6.1.

Note that when the number of particles is relatively small (from $N = 4$ to $N = 2048$) the Cundall Number is approximately constant, denoting a very similar performance for all cases. As the system size gets larger, however, the performances of the hybrid CPU-GPU algorithm are notable enhanced respect to the ones only runs on CPU. Furthermore, using and NVIDIA GeForce GT 430 graphic card the simulations executed with the hybrid CPU-GPU algorithm run faster by one and sometimes practically two orders of magnitude than on the CPUs. It is important to remark, that today there is a new generation of NVIDIA products (GeForce, Quatro and Tesla), which are based on Fermi and Kepler architecture, *i.e.* the latest CUDA architectures. Fermi and Kepler are optimized for scientific applications with key features such as 500+ gigaflops

of IEEE standard double precision floating point hardware support.

6.1.1 Realistic molecular dynamics implementation of spheres on GPUs

The results of the benchmark confirm us that to develop an accurate hybrid MD-algorithm is a valid alternative to reduce the computing time in this framework. Moreover, it leads us to a promising new prospect of real-time simulations in dense granular media.

Starting from the CUDA *particles* example we have developed a realistic molecular dynamics model for spheres with rotation. The first step was to replace the Euler's integrator by a Velocity Verlet integration method. This modification notably improved the numerical output of the algorithm. First, the global error of the Euler methods is of order one, whereas the global error of the Velocity Verlet method is of order two. Additionally, this method guarantees that the total mechanical energy of the system always oscillates around a constant value, which corresponds to the exactly solved system. The same goes for others conservative quantities like linear or angular momentum, that are always preserved or nearly preserved using this *symplectic integrator*.

On the other hand, the collision rules were changed to a generalized contact law which is proved to be more realistic than the linear contact. Furthermore, new parameters for the energy dissipation due to collision were added. The last upgrade, and the most important, was the incorporation of rotational movement to the particles.

To define the normal interaction F_{ij}^N , we use a nonlinear elastic force, depending on the overlap distance δ of the particles. Moreover, to introduce dissipation, a velocity dependent viscous damping is assumed. Hence, the total normal force reads as $F_{ij}^N = -k^N \cdot \delta^\alpha - \gamma^N \cdot v_{rel}^N$ where k^N is the spring constant in the normal direction, γ^N is the damping coefficient in the normal direction and v_{rel}^N is the normal relative velocity between i and j .

The tangential force F_{ij}^T also contains an elastic term and a tangential frictional term accounting also for static friction between the grains. Taking into account Coulomb's friction law it reads as $F_{ij}^T = \min\{-k^T \cdot \xi - \gamma^T \cdot |v_{rel}^T|, \mu F_{ij}^N\}$

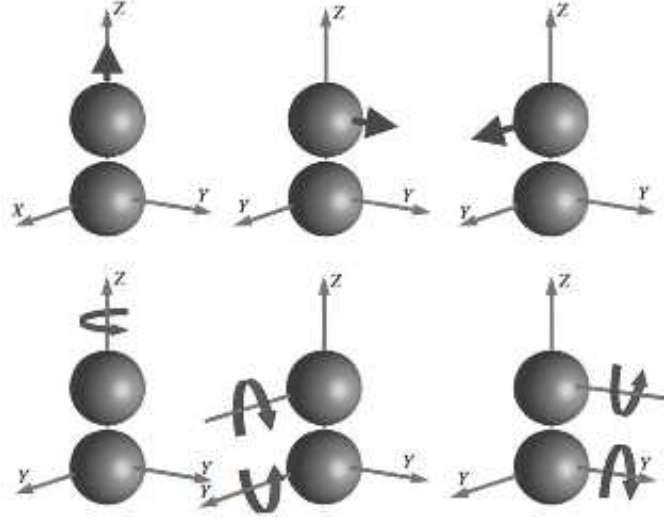


Figure 6.2: Six kinds of interactions between bonded particles: Pulling or pressing in radial direction (left, above), shearing in two tangential directions (middle and right, above), twisting (left, bottom) and bending around two axes (middle and right, bottom).

where γ^T is the damping coefficient in tangential direction, v_{rel}^T is the tangential component of the relative contact velocity of the overlapping pair. ξ represents the elastic elongation of an imaginary spring with spring constant k^T at the contact [76], which increases as $d\xi(t)/dt = v_{rel}^T$ as long as there is an overlap between the interacting particles [76, 183]. μ is the friction coefficient of the particles.

Finally we solve the Newton's equation of motion (1.5-3.1) for all particles i ($i = 1, \dots, N$)

6.1.2 Sphere Rotation on GPUs

Here, we focus our attention on the rotational part of the Newton's equation system

$$\tau_i^b = \sum_{j=1}^N L_{ij} = I_i \ddot{\theta}_i = I_{ii} \dot{\omega}_i \quad (6.2)$$

$$\dot{\omega}_i = \frac{\tau_i}{I_{ii}} \quad (i = 1, 2, 3) \quad (6.3)$$

where $\dot{\omega}_i$, τ_i and I_{ii} are angular velocities, resultant torques and principal moment of inertia measured in the body-fixed frame.

There are different ways to represent orientation of a solid body, such as Euler angles or quaternions representation. However, it has been demonstrated that quaternions can offer fundamental computational, operational and/or implementation and data handling advantages over conventional rotational methods [214]. The unit quaternion $q = (q_0, q_1, q_2, q_3) = q_0 + q_1i + q_2j + q_3k$ is often used to describe the particle orientation [215, 216] where

$$\begin{aligned} i^2 = j^2 = k^2 = ijk = -1 \\ ij = -ji = k \\ jk = -kj = i \\ ki = -ik = j \end{aligned} \quad (6.4)$$

and

$$\sum_{i=0}^3 q_i^2 = 1 \quad (6.5)$$

The physical meaning of a quaternion is that it represents a one-step rotation around the vector $q_1\hat{i} + q_2\hat{j} + q_3\hat{k}$ with a rotation angle of $2 \cdot \arccos(q_0)$ [214]. It is a very convenient tool due to some of its interesting features, such as the fact that sequences of rotations can be conveniently represented as quaternion product [214].

Quaternion for each particle satisfy the following equations of motion [215, 216]

$$\dot{q} = \frac{1}{2}Q(q)\omega \quad (6.6)$$

where

$$\dot{q} = \begin{pmatrix} \dot{q}_0 \\ \dot{q}_1 \\ \dot{q}_2 \\ \dot{q}_3 \end{pmatrix}, \quad Q(q) = \begin{pmatrix} q_0 & -q_1 & -q_2 & -q_3 \\ q_1 & q_0 & -q_3 & q_2 \\ q_2 & q_3 & q_0 & -q_1 \\ q_3 & -q_2 & q_1 & q_0 \end{pmatrix}, \quad \omega = \begin{pmatrix} 0 \\ \omega_x \\ \omega_y \\ \omega_z \end{pmatrix}.$$

Equations (6.3) and (6.6) govern the rotation of a particle and can be integrated using Fincham's leap-frog algorithm step by step [217], which is simple and proved to be accurate enough. The approach obtains $q(t + dt)$ from $q(t)$

using

$$q(t + dt) = q(t) + dt \dot{q}(t) + \frac{dt^2}{2} \ddot{q}(t) + O(dt^3) = q(t) + dt \dot{q}(t + dt/2) + O(dt^3) \quad (6.7)$$

Hence, quaternion derivative at mid-step $\dot{q}(t + dt/2)$ is required. Equation (6.6) indicates that $q(t + dt/2)$ and $\omega(t + dt/2)$ are required, the former can be easily calculated using

$$q(t + dt/2) = q(t) + \dot{q}(t)dt/2 \quad (6.8)$$

where $\dot{q}(t)$ is again delivered by (6.6), prior to which $\omega(t)$ can be calculated using

$$\omega(t) = \omega(t - dt/2) + I^{-1}\tau^b(t)dt/2 \quad (6.9)$$

and the later, $\omega(t + dt/2)$, can be determined using

$$\omega(t + dt/2) = \omega(t - dt/2) + I^{-1}dt \tau^b(t) \quad (6.10)$$

I is the inertia tensor expressed in the body-fixed frame. Hence, in this algorithm, only $\omega(t - dt/2)$, $q(t)$ need to be stored, the other quantities, such as $q(t + dt/2)$, $\omega(t)$, $\dot{q}(t)$, $\dot{q}(t + dt/2)$ are treated as temporary and auxiliary values. To avoid the buildup errors, it is a common practice to renormalize quaternions at frequent intervals (usually done every step). The entire algorithm is as follows

- step 1: calculate torque $\tau(t)$ at time t .
- step 2: using the stored $\omega(t - dt/2)$, update $\omega(t)$ using (6.9)
- step 3: determine $\dot{q}(t)$ using (6.6)
- step 4: using the stored $\omega(t - dt/2)$, calculate $\omega(t + dt/2)$ using (6.10)
- step 5: compute $q(t + dt/2)$ using (6.8)
- step 6: evaluate $\dot{q}(t + dt/2)$ using (6.6)
- step 7: calculate $q(t + dt)$ using (6.7)
- step 8: renormalize the quaternion $q(t + dt)$.

6.2 Flowchart of the granular gas simulation

The application developed, as most of the GPGPU software, has an heterogeneous architecture. This means that some pieces of code run in the CPU

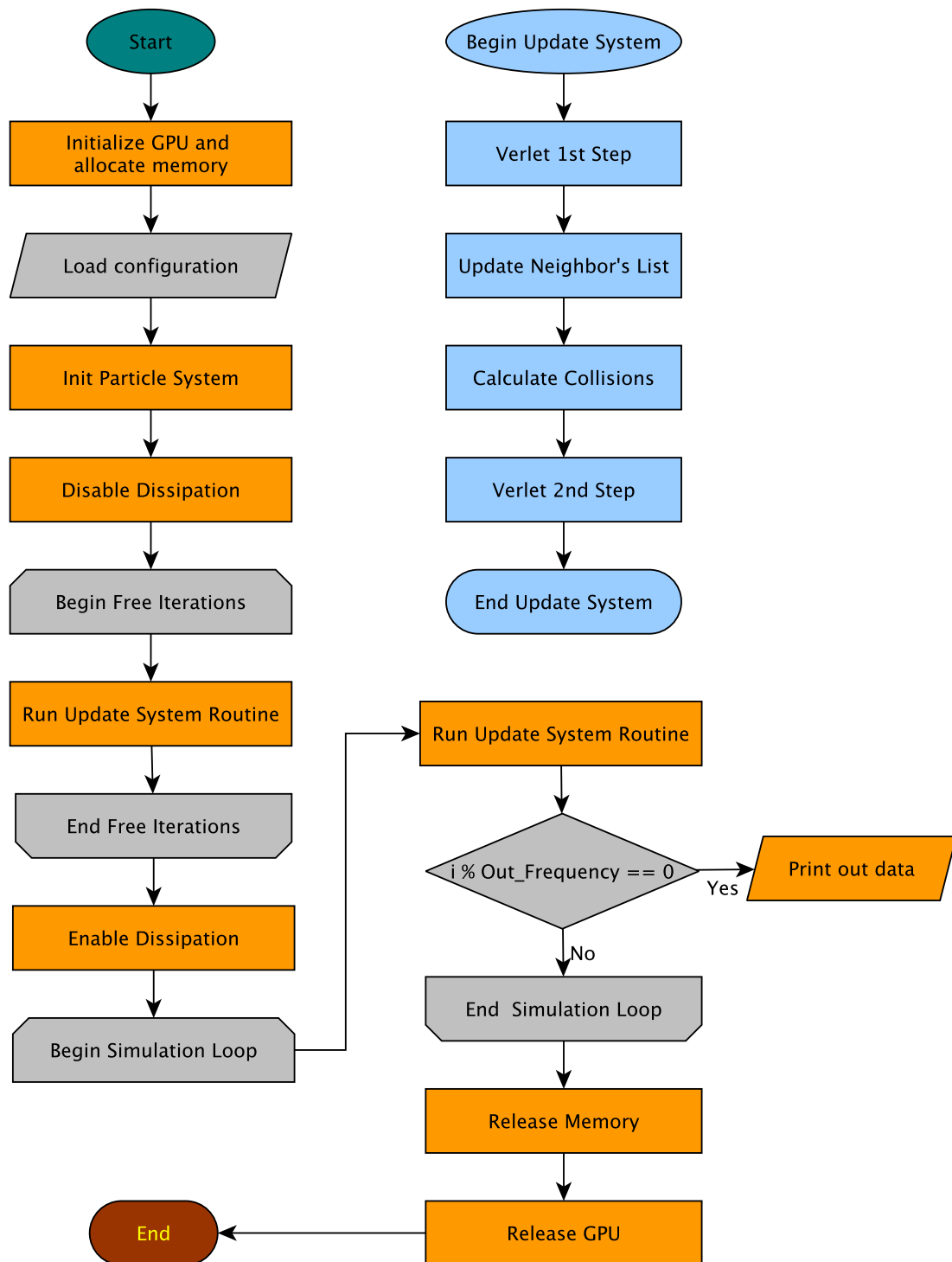


Figure 6.3: Flowchart of the granular gas simulation. Operations in gray run on the CPU, subroutines in blue run on the GPU and the ones in oranges run partially in CPU and GPU.

and others in the GPU. The flowchart of the discrete element method (DEM) simulation program developed is presented in Figure 6.3. Procedures in gray run in the CPU and the ones in blue in the GPU. The functions in orange are executed partially in the CPU and partially in the GPU, and, in most cases, they require data-interchange between CPU and GPU.

The first steps of the program consist in the initialization of the CUDA-enabled device, the allocation of the necessary memory –in both CPU and GPU– and loading configuration parameters of the granular gas. Initially, the particles are homogeneously distributed in the simulation space with a random velocity for translational and rotational movements (this is done on the host and afterwards the particles' information is sent to the device). With the objective of avoiding the initial configuration effect, the dissipation due to particle-particle interaction is disabled, and a number of *free iterations* is performed. After that, the energy loss is enabled again and the main loop of the program starts, calling in each iteration the *Update System* subroutine, and with a periodic frequency printing out the particles information. Finally the resources reserved are released and the program ends.

The DEM process takes place in the *Update System* routine. Initially, following the Velocity Verlet integration method, the particles' velocity in the mid-point is calculated and with it the positions are updated. Then, with the aim of minimizing the time used by the collisions method, the list with the particles that are neighbors to each other is updated. For details about the implementation of the neighbor function see the documentation given by NVIDIA Corporation together with the CUDA *particles* example [212]. Next, the collisions between particles are computed by calculation of the forces and torques that a particle experiences. Finally, the last step of the Verlet integrator is performed, obtaining the new velocities from the forces and using the algorithm described in Section 6.1.2 to calculate angular velocities and positions.

6.3 Validation

The numerical accuracy of our model has been validated comparing it to the mean field analytical solution of the homogeneous cooling of a gas of rough

and dissipative spherical particles. Luding *et al* [54] have found that translational and rotational kinetic energy of granular gas of rough and dissipative particles in homogeneous cooling is governed by the following system of equations

$$\begin{aligned}\frac{d}{d\tau}T &= -AT^{3/2} + BT^{1/2}R \\ \frac{d}{d\tau}R &= BT^{3/2} - CT^{1/2}R\end{aligned}\quad (6.11)$$

with the constants A , B and C , whose values depend on space dimensionality D (for details see [54]).

$$\begin{aligned}A &= \frac{1-e_n^2}{4} + \eta(1-\eta) \\ B &= \frac{\eta^2}{q} \\ C &= \frac{\eta}{q} \left(1 - \frac{\eta}{q}\right)\end{aligned}\quad (6.12)$$

where $\eta = q(1 + e_t)/(2q + 2)$ (in 3D $q = 2/5$) and e_n and e_t are the restitution coefficients on the normal and tangential direction respectively. Moreover, the mean time between collisions $G = 8(2a)^2 \frac{N}{V} \sqrt{\frac{\pi}{m}} g(2a)$, is used to rescale real time scale accordingly to $\tau = \frac{2}{3}GT_{tr}^{1/2}(0)t$. Moreover, the strength of the dissipation can also be included into the characteristic time $\tau = \frac{2}{3}(1 - e_n^2)GT_{tr}^{1/2}(0)t$ [47].

To compare the numerical output of our code with the theoretical predictions (Equations 6.11), we have to find equivalent dissipation parameters (γ_n , γ_t and k_t) that correspond to specific values of the normal e_n and tangential e_t restitution coefficients.

6.3.1 Equivalent dissipative parameters

In the simplest approximation, the normal interaction force between two contacting particles is a linear spring $f_{el}^n = k^N \delta$ ($\alpha = 1$ in Equation ??) and a velocity dependent viscous damping $f_{diss}^n = \gamma_n \dot{\delta}$ [70]. Examining the contact evolution one gets the well known differential equation of the damped harmonic oscillator [70]

$$\ddot{\delta} + 2\eta\dot{\delta} + w_0^2\delta = 0 \quad (6.13)$$

Here $w_0 = \sqrt{k/m_{12}}$ is the oscillation frequency of an elastic oscillator and η is the effective viscosity, obtained as

$$\gamma_n = 2 \eta m_{12} \quad (6.14)$$

where $m_{12} = m_1 m_2 / (m_1 + m_2)$ is the reduced mass. Solving Eq.(6.13) one can find the effective restitution coefficient,

$$e_n = \exp(-\pi\eta/\omega) \quad (6.15)$$

where

$$\omega = \sqrt{\omega_0^2 - \eta^2} \quad (6.16)$$

is the oscillation frequency of the damped oscillator. Combining Equations (6.15) and (6.16) and substituting in Equation (6.14) one obtains,

$$\gamma_n = \sqrt{\frac{4 k_n m_{12}}{\left(\frac{\pi}{\ln \frac{1}{e_n}}\right)^2 + 1}} \quad (6.17)$$

On the other hand, describing the tangential force between to contacting particles, one can also consider a tangential spring $f_{el}^t = k^t \delta$ and a velocity dependent viscous damping $f_{diss}^t = \gamma_t \dot{\delta}$ [70]. For the sake of simplicity, here we examined the case $\gamma_t = 0$; for which an analytic expression, relating k_t and k_n , can be derived,

$$k_t = \frac{k_n q}{1 + q} \left(\frac{\arccos(-e_t)}{\pi} \right)^2 \quad (6.18)$$

where $q = 2/5$ stands for the 3D case [70].

6.3.2 Numerical Results

We have numerically studied the free cooling kinetics of a dilute system of $N = 4096$ spheres confined within a square box with $l = 2$, resulting a volume fraction of $V_f = 0.008$. Initially, the particles are homogeneously distributed in the space and their translational and rotational velocities follow a Gaussian distribution. In order to avoid memory effects from the initial conditions, we

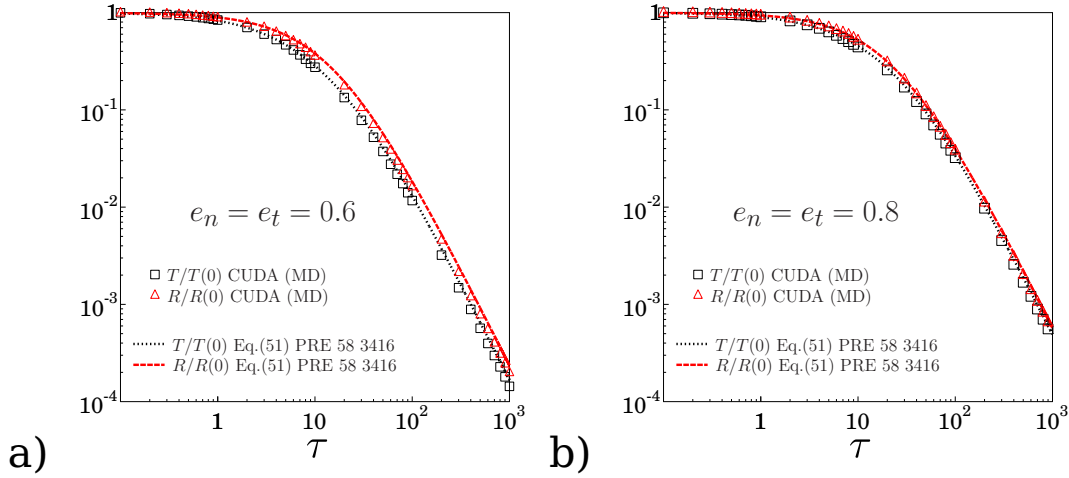


Figure 6.4: Comparison of numerical (shapes) with theoretical results (lines). Black for translational and red for the rotational movement. **It can be seen** it that a good agreement between the theory and the numerical method is achieved for both restitution coefficients. a) $e_n = e_t = 0.6$ b) $e_n = e_t = 0.8$

allow the system to execute a few collisions before starting to analyze the particles' temporal evolution. The system is examined until the total mean translational and rotational kinetic energies have decayed several orders of magnitude. To model hard particles, the maximum overlap must always be much smaller than the particle size; this is ensured by introducing values for normal elastic constant, $k_n = 10^8 Nm$ and a particle's density of $\rho = 2000 kg/m^3$. To compare the algorithm performance with the mean field model [54], systems of particles with two different restitution coefficient were studied, $e_n = e_t = 0.6$ and $e_n = e_t = 0.8$. The corresponding dissipative parameters have been calculated using the equations (6.17) for the normal damping coefficient γ_n and (6.18) for the stiffness of the tangential spring k_t . For this range of parameters we have set a time step $dt = 10^{-6} s$, thus, the equations of motion, Eqs. (??-??), are integrated using a Verlet-velocity algorithm with a numerical error proportional to $(\Delta t)^6$.

In Figure 6.4, the evolution of the translational T and rotational R kinetic energies are illustrated. Note that in every case the time scale has been rescaled using the corresponding characteristic time, resulting in $\tau = \frac{2}{3}(1 - e_n^2)GT_{tr}^{1/2}(0)t$. As we start from an equilibrium state and the dissipation is

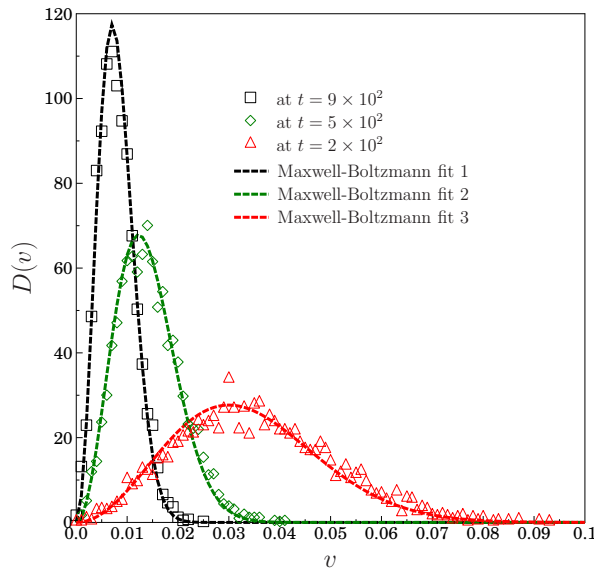


Figure 6.5: Speed distribution for $e_n = e_t = 0.8$ at $t = 2 \times 10^2$ (red), $t = 5 \times 10^2$ (green) and $t = 9 \times 10^2$ (black). The velocity distributions follow Maxwell-Boltzmann statistics, indicating that the system remains in the homogeneous cooling state.

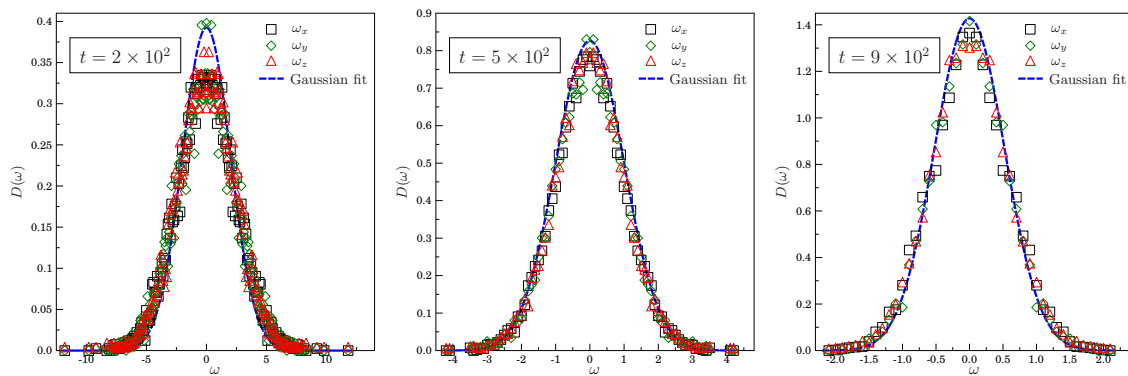


Figure 6.6: Angular velocity distribution for $e_n = e_t = 0.8$. left) at $t = 2 \times 10^2$. center) $t = 5 \times 10^2$. right) $t = 9 \times 10^2$. In all cases, the angular velocity distributions are in agreement with a Gaussian behavior, denoting the homogeneous cooling process at the rotational level.

low, the system evolves into a homogeneous cooling state. In such a state, the kinetic energy, decreases homogeneously and the time evolution of all variables occurs only through its global temperature. For comparison we also show the corresponding analytic result of Eq. 6.11 for the same restitution coefficients. The excellent agreement archived for both cases validates the numerical performance of the new algorithm.

During the cooling process the velocity statistics was also examined. As we mentioned earlier, the simulations begin from a Gaussian velocity distribution for both, the translational and angular degree of freedom. Low dissipative particles cool down uniformly over a wide range of time. Thus, all the temporal dependences enter through the mean values of the translational and rotational temperature. Such a picture is consistent with the results shown in Fig. 6.5 ($e_n = e_t = 0.8$) where the speed distribution, $D(c)$ and ($c = \sqrt{v_x^2 + v_y^2 + v_z^2}$) is presented at several times. In all cases, the speed distribution remains close to a Maxwell-Boltzmann speed distribution $D(c) = 4\pi \left(\frac{1}{\pi v_{mp}^2}\right)^{3/2} c^2 e^{-c^2/v_{mp}^2}$, where $v_{mp}(t)$ is the most probable velocity. For the rotational degree of freedom, in Fig. 6.6 we plot the angular velocity distribution for each angular component obtained at different times. The data proves that cooling process at the rotational level also occurs homogeneously. Thus, the three components of the angular velocity behave equivalently and with the same characteristic values. In all cases the distribution follows a Gaussian behavior $f(w_i) = \frac{1}{\sigma\sqrt{2\pi}} e^{-w_i^2/2\sigma^2}$ featuring the expected homogeneous cooling process. The same procedure was applied for $e_n = e_t = 0.6$ and similar results have been obtained (data not show).

6.3.3 Optimal number of GPU

In any program that runs in parallel the execution time depends, in conjunction with the hardware, on the number of tasks running simultaneously. However, there is no an established way to define the optimal number of processors to use within the hardware configuration. In programs that manipulate a big volume of data this number depends, among other things, on the amount of memory used per thread; the data interchanged between tasks may become a

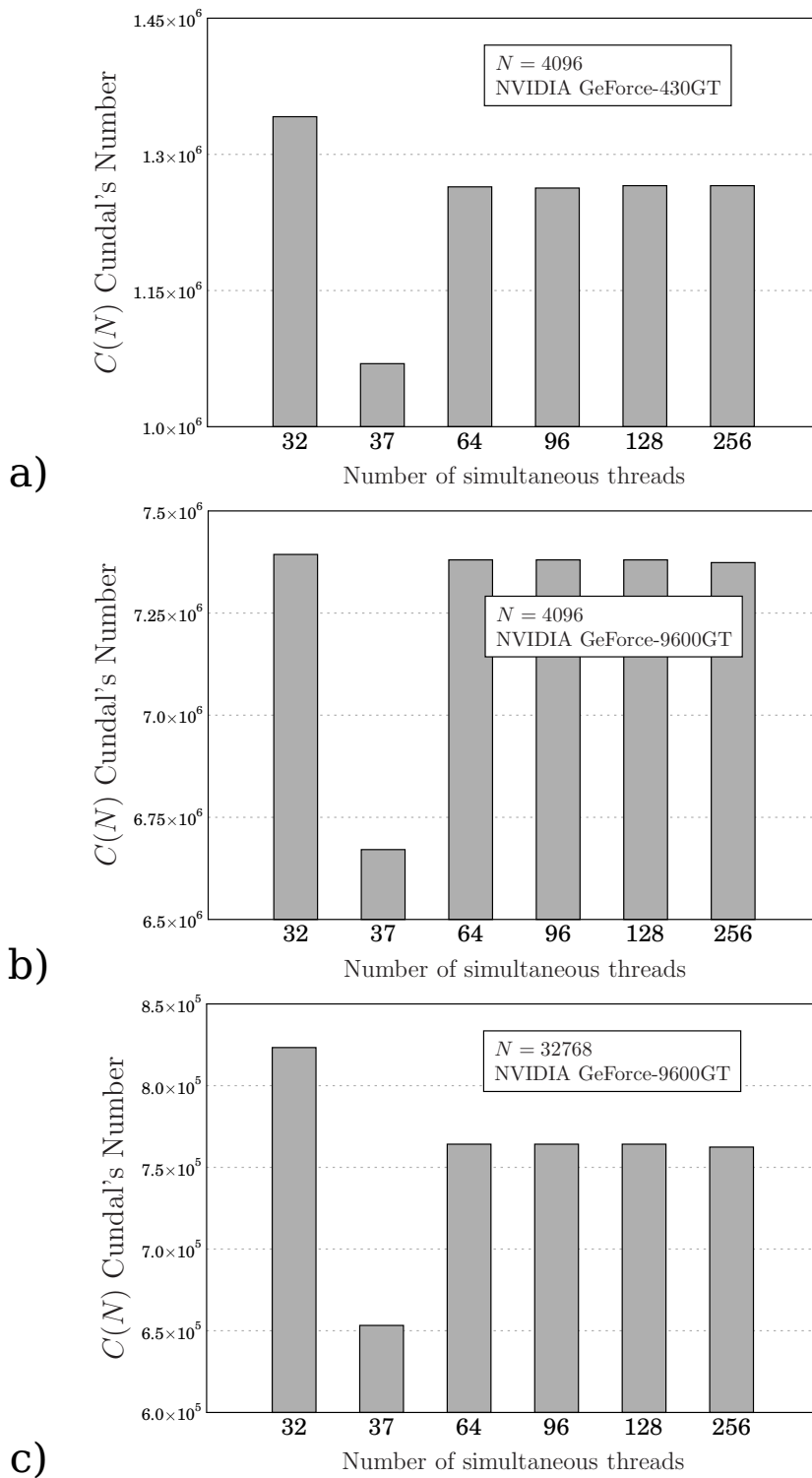


Figure 6.7: Cundall's number (Equation 6.1) of a granular gas or rough particles simulated with the DEM developed for different number of simultaneous threads. a) 4096 particles simulated on a graphic card GeForce GT 430. b) 4096 particles simulated on a graphic card GeForce 9600 GT. c) 32768 particles simulated on a graphic card GeForce 9600 GT.

bottleneck.

To find the optimal value for the DEM created, a benchmark of a granular gas of rough particles was performed. The comparison was made in two different NVIDIA graphic cards, in an NVIDIA® GeForce® GT 430 and in an NVIDIA® GeForce® 9600 GT. In all cases the mean value for 10 different executions –1000000 iterations each one– are presented. In the first GPU the simulation was of 4096 particles and in the second one the test was done for 4096 and 32768 particles. The result of the benchmark is shown in Figure 6.7.

For our hardware, 32 simultaneous threads seems to be the optimum value. Furthermore, the results suggest that using a number that is not a power of two –37 was used during the tests– is a bad decision. This can be inflicted by taking a look to the architecture of the NVIDIA's GPUs. The number of CUDA Cores present in all their graphics cards is a power of two. Therefore, using a value that is not power of two result in wasting part of the processor each time.

6.4 Conclusions

In typical technological process the flows contain billions of particles and the main disadvantages of molecular dynamics algorithms implemented on computing processing units (CPU) are the maximum number of particles and the duration of a virtual simulation. In this chapter we have described the implementation of an accurate molecular dynamic algorithm for mono-disperse systems of spheres with rotation, using graphical processing units (GPUs). The employment of this technique saves a huge computational time versus the traditional CPU method. Moreover, we have proved that the algorithm complies with the statistical mechanical laws and the results agree with established mean field theories for low dense granular systems. Our results are in excellent agreement with a previous mean field analytical model, which describes the cooling dynamics of a system composed by dissipative and rough spheres. All this leads us to a promising new prospect of real-time simulations in many different technological scenarios concerning dense granular media.

Chapter 7

General conclusions

A novel numerical scheme to simulate the kinetics of non-linear fragmentation equations have been introduced. The method is based on the Direct Simulation Monte Carlo (DSMC) technique for solving the Boltzmann equation. This approach have been generalized for solving kinetic equations where the number of particles vary changes in time. Hence, we have validated the algorithm examining simplest fragmentation kernels, where exact solutions exist. The proposed approach recover the detailed time evolution accurately, as well as the emergence of asymptotic scaling regimes. Such a comparison has shown the ability of the scheme to cover a significant number of decades in order to capture the broad size distributions characterizing fragmenting systems, thus making it possible to carry out quantitative, detailed comparisons. We have extended and made use of the algorithm to analyze general fragmentation kernels, where exact analytic predictions for the kinetics of fragmenting systems are lacking. Furthermore, we have shown that with the good statistics achieved with the numerical technique proposed, it is possible to follow the development of an advancing front for generic asymmetric fragmentation kernels. Such an understanding promotes confidence in the development of scaling distribution functions.

The cooling dynamics of a 2D granular gas of elongated grains have been examined. For weakly dissipative particles, we have found that the mean kinetic energy decreases asymptotically as $\frac{E(t)}{E_0} = \frac{1}{(1+t/t_0)^{5/3}}$, in agreement with Brilliantov and Pöschel predictions for the homogeneous cooling state

regimen (HCS) of viscoelastic particles [46, 158]. A higher dissipation induces an inhomogeneous cooling process and the energy vanishes as $\frac{E(t)}{E_0} \sim t^{-1.2}$. The rotational energy, however, always decays as $\frac{R(t)}{R_0} \sim t^{-2}$, which is agreement with Haff's prediction for the HCS of inelastic particles. The lack of energy equipartition is kept even during the inhomogeneous cooling process where strong inhomogeneities in the velocity field are presented. A strong influence of the particle shape and inelasticity on the structure of the clusters have been observed. Our numerical outcomes suggest that the strong dissipation and the particle anisotropy induce the formation of ordered cluster structures and velocity vortices, which notably slow down the cooling process and retard the appearance of large clusters which break and reform. Increasing the particle anisotropy enhances this distinct evolution as a function of the particle energy dissipation. This behavior can be attributed to the detailed interaction between ordered clusters of particles, where rotational degrees of freedom play a relevant role. The breakup of big clusters of elongated particles as a results of their collisions leads to the formation of smaller clusters, promoting a faster decay of the rotational kinetic energy. Such smaller clusters of ordered particles in turn delay the development of the inhomogeneous cooling regime. Understanding the impact of these strong correlations in agitated systems where energy is supplied continuously constitutes an interesting venue in the fundamental understanding of the physics of anisotropic granulates and the subtle interplays between particle shape and inelasticity.

The micro-mechanical properties of deposits of faceted particles have been examined, in details. For instance, the partial discharge of a silo filled with faceted grains has a profound effect on the deposit morphology and its stress distribution. During the discharge, the shear between grains induces their rotation and their settlement in more disordered arrangements. For elongated particles, the preferred horizontal orientation displayed after the silo filling disappears. For square particles, the discharge provokes an alignment of their sides with gravity which minimizes the friction and favors their vertical displacement. As a result of the changes in particle orientation, the pressure distribution in the silo changes qualitatively; while for elongated rods lateral stress transmission is promoted by the enhanced disorder leading

to a faster pressure saturation, the opposite holds for squares. In this latter case the alignment of squares induced by the flow destroys the initial force chain network which is replaced by a mainly vertical stress transmission. As a consequence, a significant reduction of the pressure saturation effect is observed. With this results, we clarified the performance and stability of silos, which need to support high stresses that become very sensitive to grain shapes and the silo steering history. If we increase the amount of material flowing out of the silo, or induce a second discharge, we expect that the observed effect will be enhanced. Although we have focused on weakly disordered initial deposits, due to the low feeding rates used to fill the silo, the main features discussed here are expected for other silo filling procedures. Perhaps, increasing the disorder of the initial packing will generically decrease the relative magnitude of the changes discussed.

To introduce an attractive force in deposits of elongated grains has a profound effect on the deposit morphology and its stress profiles.

In deposits of non-cohesive particles the topology is dominated by the formation of ordered structures of aligned rods. Elongated particles tend to align horizontally and the stress is mainly transmitted from top to bottom, revealing an asymmetric distribution of the local stress. Lateral force transmission becomes less favored compared to vertical transfer, thus hindering pressure saturation with depth. For deposits of cohesive particles, the preferred horizontal orientation is less pronounced with increasing cohesion. Very elongated particles with strong attractive forces form extremely loose structures, characterized by orientation distributions, which tend to a uniform behavior when increasing the Bond number. As a result of these changes, the pressure distribution in the deposits changes qualitatively. The spherical component of the local stress is notably enhanced with respect to the deviatoric part. Hence, the lateral stress transmission is promoted by the enhanced disorder and it leads to a faster pressure saturation with depth.

The implementation of an accurate molecular dynamic algorithm for mono-disperse systems of spheres with rotation, using graphical processing units (GPUs) was described in details. The employment of this technique saves a huge computational time versus the traditional CPU

method. Moreover, we have proved that the algorithm complies with the statistical mechanical laws and the results agree with established mean field theories for low dense granular systems. Our results are in excellent agreement with a previous mean field analytical model, which describes the cooling dynamics of a system composed by dissipative and rough spheres. All this leads us to a promising new prospect of real-time simulations in many different technological scenarios concerning dense granular media.

Bibliography

- [1] J. Duran, *Sands, Powders, and Grains: An Introduction to the Physics of Granular Materials*. Springer, 1 ed., 1999.
- [2] G. E. Moore, "Cramming more components onto integrated circuits," *Electronics*, vol. 38, p. 114, April 1965.
- [3] G. E. Moore, "Progress in digital integrated electronics," in *Electron Devices Meeting, 1975 International*, vol. 21, pp. 11–13, 1975.
- [4] N. Metropolis and S. Ulam, "The monte carlo method," *Journal of the American Statistical Association*, vol. 44, p. 247, 1949.
- [5] B. Alder and T. Wainwright, "Phase transition for a hard sphere system," *J. Chem. Phys.*, vol. 24, no. 5, p. 1208, 1957.
- [6] B. Alder and T. Wainwright, "Studies in molecular dynamics. i. general method," *J. Chem. Phys.*, vol. 31, no. 2, p. 459, 1959.
- [7] N. Metropolis, "The beginning of the monte carlo method," *Los Alamos Science, Special Issue*, vol. 15, pp. 125–130, 1987.
- [8] J. Hammersley, "Monte carlo methods for solving multivariable problems," *Annals of the New York Academy of Sciences*, vol. 86, no. 3, pp. 844–874, 1960.
- [9] W. Press, B. Flannery, S. Teukolsky, and W. Vetterling, *Numerical Recipes in FORTRAN: The Art of Scientific Computing.*, ch. 7.6 Simple Monte Carlo Integration, pp. 295–299. Cambridge University Press, 2nd ed., 1992.

- [10] W. Press, B. Flannery, S. Teukolsky, and W. Vetterling, *Numerical Recipes in FORTRAN: The Art of Scientific Computing.*, ch. 7.8 Adaptive and Recursive Monte Carlo Methods, pp. 306–319. Cambridge University Press, 2nd ed., 1992.
- [11] K. Binder, ed., *The Monte Carlo Method in Condensed Matter Physics*. New York: Springer, 2nd ed., December 1995.
- [12] P. Mackeown, *Stochastic Simulation in Physics*. Secaucus, NJ, USA: Springer Verlag, Singapore, 2001.
- [13] W. C. H. Gould, J. Tobochnik, *An Introduction to Computer Simulation Methods: Applications to Physical Systems*. Pearson Addison Wesley, 3rd ed., 2007.
- [14] D. Landau and K. Binder, *A Guide to Monte Carlo Simulations in Statistical Physics*. Cambridge University Press, 3 ed., October 2009.
- [15] I. Pagonabarraga, T. Kanzaki, and R. Hidalgo, “Collision induced fragmentation: A simplenumerical algorithm,” *Eur. Phys. J. Special Topics*, vol. 179, pp. 43–53, 2009.
- [16] K. Binder and D. Heermann, *Monte Carlo Simulation in Statistical Physics: An Introduction*. New York: Springer, 5th ed., August 2010.
- [17] J. Farjas and P. Roura, “Numerical model of solid phase transformations governed by nucleation and growth: Microstructure development during isothermal crystallization,” *Phys. Rev. B*, vol. 75, no. 18, p. 184112, 2007.
- [18] F. Dellaert, D. Fox, W. Burgard, and S. Thrun, “Monte carlo localization for mobile robots,” in *IEEE International Conference on Robotics and Automation (ICRA99)*, pp. 1322–1328, May 1999.
- [19] S. Thrun., D. Fox, W. Burgard, and F. Dellaert, “Robust monte carlo localization for mobile robots,” *Artificial Intelligence*, vol. 128, no. 1-2, pp. 99–141, 2001.

- [20] T. Li, S. Sun, and J. Duan, "Monte carlo localization for mobile robot using adaptive particle merging and splitting technique," in *Proceedings of the 2010 IEEE International Conference on Information and Automation*, (Harbin), pp. 1913–1918, June 2010.
- [21] G. Drusano, D. D'Argenio, S. Preston, C. Barone, W. Symonds, S. LaFon, M. Rogers, W. Prince, A. Bye, and J. A. Bilello, "Use of drug effect interaction modeling with monte carlo simulation to examine the impact of dosing interval on the projected antiviral activity of the combination of abacavir and amprenavir," *Antimicrobial Agents and Chemotherapy*, vol. 44, no. 6, pp. 1655–1659, 2000.
- [22] H. Paganetti, "Monte carlo calculations for absolute dosimetry to determine machine outputs for proton therapy fields," *Phys. Med. Biol.*, vol. 51, no. 11, p. 2801, 2006.
- [23] S. Kim, "Characteristics of elliptical sources in beamnrc monte carlo system: Implementation and application," *Med. Phys.*, vol. 36, no. 4, p. 1046, 2009.
- [24] D. Merl, L. Johnson, R. Gramacy, and M. Mangel, "A statistical framework for the adaptive management of epidemiological interventions," *PLoS ONE*, vol. 4, no. 6, p. e5807, 2009.
- [25] C. Forastero, L. Zamora, D. Guirado, and A. Lallena, "A monte carlo tool to simulate breast cancer screening programmes," *Physics in Medicine and Biology*, vol. 55, no. 17, p. 5213, 2010.
- [26] C. Mode, ed., *Applications of Monte Carlo Methods in Biology, Medicine and Other Fields of Science*. Rijeka, Croatia: InTech, February 2011.
- [27] P. Boyle, M. Broadie, and P. Glasserman, "Monte carlo methods for security pricing," *Journal of Economic Dynamics and Control*, vol. 21, pp. 1267–1321, June 1997.
- [28] D. Vose, *Risk analysis: a quantitative guide*. John Wiley & Sons, 2nd ed., 2000.

- [29] J. Charnes and P. Shenoy, "Multistage monte carlo method for solving influence diagrams using local computation," *Management Science*, vol. 50, pp. 405–418, March 2004.
- [30] C. Beveridge and M. Joshi, "Monte carlo bounds for game options including convertible bonds," *Management Science*, vol. 57, pp. 960–974, April 2011.
- [31] C. Grinstead and J. Snell, *Introduction to Probability*, ch. 9. Central Limit Theorem, pp. 325–360. American Mathematical Soc., 2nd ed., 1997.
- [32] G. Fishman, *Monte Carlo: concepts, algorithms, and applications*. Springer series in operations research, New York, USA: New York: Springer, 1996.
- [33] N. Metropolis, A. Rosenbluth, M. Rosenbluth, A. Teller, and E. Teller, "Equation of state calculations by fast computing machines," *J. Chem. Phys*, vol. 21, p. 1087, 1953.
- [34] W. Hastings, "Monte carlo sampling methods using markov chains and their applications," *Boimetrika*, vol. 57, pp. 97–109, July 1970.
- [35] G. Birkhoff, "Proof of the ergodic theorem," *Proc Natl Acad Sci USA*, vol. 17, no. 12, pp. 656–660, 1931.
- [36] J. von Neumann, "Physical applications of the ergodic hypothesis," *Proceedings of the National Academy of Sciences of the United States of America*, vol. 18, no. 3, pp. 263–266, 1932.
- [37] G. Birkhoff, "What is the ergodic theorem?," *Mathematical Association of America*, vol. 49, no. 4, pp. 222–226, 1942.
- [38] P. Walters, *An Introduction to Ergodic Theory (Graduate Texts in Mathematics)*. Springer, October 2000.
- [39] G. Bird, "Approach to translational equilibrium in a rigid sphere gas," *Phys. Fluids*, vol. 6, p. 1518, 1963.

- [40] A. Rahman, "Correlations in the motion of atoms in liquid argon," *Phys. Rev.*, vol. 136, no. 2A, pp. A405–A411, 1964.
- [41] L. Verlet, "Computer "experiments" on classical fluids. i. thermodynamical properties of lennard-jones molecules," *Phys. Rev.*, vol. 159, no. 1, pp. 98–103, 1967.
- [42] L. Verlet, "Computer "experiments" on classical fluids. ii. equilibrium correlation functions," *Phys. Rev.*, vol. 165, no. 1, pp. 201–214, 1968.
- [43] T. Pöschel and T. Schwager, *Computational Granular Dynamics*. Springer-Verlag Berlin Heidelberg New York, 2005.
- [44] M. Allen and D. Tildesley, *Computer Simulation of Liquids*. Clarendon Press, Oxford, 1987.
- [45] I. Goldhirsch and G. Zanetti, "Clustering instability in dissipative gases," *Phys. Rev. Lett.*, vol. 70, no. 11, pp. 1619–1622, 1993.
- [46] N. Brilliantov and T. Pöschel, "Velocity distribution in granular gases of viscoelastic particles," *Phys. Rev. E*, vol. 61, p. 5573, 2000.
- [47] S. Miller and S. Luding, "Cluster growth in two- and three-dimensional granular gases," *Phys. Rev. E*, vol. 69, p. 031305, 2004.
- [48] S. Miller and S. Luding, "Event-driven molecular dynamics in parallel," *Journal of Computational Physics*, vol. 193, no. 1, pp. 306–316, 2004.
- [49] J. Jenkins and M. Richman, "Kinetic theory for plane flows of a dense gas of identical, rough, inelastic, circular disks," *Physics of Fluids*, vol. 28, no. 12, p. 3485, 1985.
- [50] M. Huthmann and A. Zippelius, "Dynamics of inelastically colliding rough spheres: Relaxation of translational and rotational energy," *Phys. Rev. E*, vol. 56, pp. R6275–R6278, 1997.
- [51] S. McNamara and S. Luding, "Energy nonequipartition in systems of inelastic, rough spheres," *Phys. Rev. E*, vol. 58, no. 2, pp. 2247–2250, 1998.

- [52] R. Caferio, S. Luding, and H. Herrmann, "Rotationally driven gas of inelastic rough spheres," *EPL (Europhysics Letters)*, vol. 60, p. 854, 2002.
- [53] E. Ben-Naim, S. Chen, G. Doolen, and S. Redner, "Shocklike dynamics of inelastic gases," *Phys. Rev. Lett.*, vol. 83, p. 4069, 1999.
- [54] S. Luding, M. Huthmann, S. McNamara, and A. Zippelius, "Homogeneous cooling of rough dissipative particles: Theory and simulations," *Phys. Rev. E*, vol. 58, pp. 3416–3425, 1998.
- [55] R. Caferio, S. Luding, and H. Herrmann, "Two-dimensional granular gas of inelastic spheres with multiplicative driving," *Phys. Rev. Lett.*, vol. 84, pp. 6014–6017, 2000.
- [56] T. Aspelmeier, G. Giese, and A. Zippelius, "Cooling dynamics of a dilute gas of inelastic rods: A many particle simulation," *Phys. Rev. E*, vol. 57, p. 857, 1998.
- [57] A. Donev, S. Torquato, and F. Stillinger, "Neighbor list collision-driven molecular dynamics simulation for nonspherical hard particles. i. algorithmic details," *Journal of Computational Physics*, vol. 202, no. 2, pp. 737–764, 2005.
- [58] A. Donev, S. Torquato, and F. Stillinger, "Neighbor list collision-driven molecular dynamics simulation for nonspherical hard particles.: ii. applications to ellipses and ellipsoids," *Journal of Computational Physics*, vol. 202, no. 2, pp. 765–793, 2005.
- [59] M. Bannerman and L. Lue, "Transport properties of highly asymmetric hard-sphere mixtures," *Journal of Chemical Physics*, vol. 130, no. 16, p. 164507, 2009.
- [60] S. González, A. Thornton, and S. Luding, "An event-driven algorithm for fractal cluster formation," *Computer Physics Communications*, vol. 182, no. 9, pp. 1842–1845, 2011.

- [61] Y. Taguchi, "Powder turbulence: direct onset of turbulent flow," *J. Phys. II France*, vol. 2, no. 12, pp. 2103–2114, 1992.
- [62] R. Ramírez, T. Pöschel, N. Brilliantov, and T. Schwager, "Coefficient of restitution of colliding viscoelastic spheres," *Phys. Rev. E*, vol. 60, no. 4, pp. 4465–4472, 1999.
- [63] F. Bridges, A. Hatzes, and D. Lin, "Structure, stability and evolution of saturn's rings," *Nature*, vol. 309, pp. 333–335, 1984.
- [64] S. Luding, E. Clément, A. Blumen, J. Rajchenbach, and J. Duran, "Anomalous energy dissipation in molecular dynamics simulations of grains: The "detachment effect"," *Phys. Rev. E*, vol. 50, p. 4113, 1994.
- [65] S. Foerster, M. Louge, H. Chang, and K. Allia, "Measurements of the collision properties of small spheres," *Physics of Fluids*, vol. 6, no. 3, p. 1108, 1993.
- [66] E. Falcon, C. Laroche, S. Fauve, and C. Coste, "Behavior of one inelastic ball bouncing repeatedly off the ground," *The European Physical Journal B*, vol. 3, no. 1, pp. 45–57, 1998.
- [67] F. Gerl and A. Zippelius, "Coefficient of restitution for elastic disks," *Phys. Rev. E*, vol. 59, no. 2, pp. 2361–2372, 1999.
- [68] T. Schwager, "Coefficient of restitution for viscoelastic disks," *Phys. Rev. E*, vol. 75, p. 051305, 2007.
- [69] P. Müller and T. Pöschel, "Collision of viscoelastic spheres: Compact expressions for the coefficient of normal restitution," *Phys. Rev. E*, vol. 84, no. 2, p. 021302, 2011.
- [70] S. Luding, "Collisions & contacts between two particles," in *Physics of dry granular media - NATO ASI Series E350* (H. J. Herrmann, J.-P. Hovi, and S. Luding, eds.), (Dordrecht), pp. 285–304, Kluwer Academic Publishers, 1998.
- [71] F. Kun and H. Herrmann, "Transition from damage to fragmentation in collision of solids," *Phys. Rev. E*, vol. 59, pp. 2623–2632, 1999.

- [72] F. Alonso-Marroquín, I. Vardoulakis, H. Herrmann, D. Weatherley, and P. Mora, "Effect of rolling on dissipation in fault gouges," *Phys. Rev. E*, vol. 74, p. 031306, 2006.
- [73] A. Pena, P. Lind, and H. Herrmann, "Modeling slow deformation of polygonal particles using dem," *Particuology*, vol. 6, no. 6, pp. 506–514, 2008.
- [74] H.-J. Tillemans and H. Herrmann, "Simulating deformations of granular solids under shear," *Physica A*, vol. 217, pp. 261–288, 1995.
- [75] F. Kun and H. Herrmann, "A study of fragmentation processes using a discrete element method," *Computer Methods in Applied Mechanics and Engineering*, vol. 138, pp. 3–18, 1996.
- [76] P. Cundall and O. Strack, "A discrete numerical model for granular assemblies," *Geotechnique*, vol. 29, pp. 47–65, 1979.
- [77] A. Pena, P. Lind, S. McNamara, and H. Herrmann, "Numerical improvement of the discrete element method applied to shear of granular media." *Condensed matter*, 2007.
- [78] A. Pena, R. García-Rojo, and H. Herrmann, "Influence of particle shape on sheared dense granular media," *Granular Matter*, vol. 9, pp. 279–291, 2007.
- [79] A. Iserles, *A first course in the numerical analysis of differential equations*. Cambridge texts in applied mathematics. Issue 15 of Texts in Applied Mathematics, Cambridge, England: Cambridge University Press, 1996.
- [80] M. Alvarez, A. Guerra, and R. Lau, *Matemática Numérica*. La Habana, Cuba: Editorial Félix Varela, 2nd ed., 2004.
- [81] J. Lambert, *Numerical methods for ordinary differential systems: the initial value problem*. New York, NY, USA: John Wiley & Sons, 1991.
- [82] J. Butcher, *Numerical methods for ordinary differential equations*. New York, NY, USA: John Wiley and Sons, 2nd ed., 2008.

- [83] K. New, K. Watt, C. Misner, and J. Centrella, "Stable 3-level leapfrog integration in numerical relativity," *Phys. Rev. D*, vol. 58, no. 6, p. 064022, 1998.
- [84] E. Hairer, C. Lubich, and G. Wanner, "Geometric numerical integration illustrated by the störmer-verlet methods," *Acta Numerica*, vol. 12, pp. 399–450, 2003.
- [85] G. Forsythe, M. Malcolm, and C. Moler, *Computer methods for mathematical computations*. Prentice-Hall, 1977.
- [86] E. Hairer, S. Nørsett, and G. Wanner, *Solving ordinary differential equations: Nonstiff problems*, vol. Volume 1 of Solving Ordinary Differential Equations, Gerhard Wanner of *Springer series in computational mathematics*. Springer, 2nd ed., 1993.
- [87] C. Gear, *Numerical Initial Value Problems in Ordinary Differential Equations*. NJ, USA: Prentice Hall, 1st ed., September 1971.
- [88] W. Press, S. Teukolsky, W. Vetterling, and B. Flannery, *Numerical Recipes 3rd Edition: The Art of Scientific Computing*, ch. 17.6. Multistep, Multivalued, and Predictor-Corrector Methods, pp. 942–946. Cambridge University Press, 3rd ed., September 2007.
- [89] K. Schoen, "Fifth and sixth order pece algorithms with improved stability properties," *SIAM Journal on Numerical Analysis*, vol. 8, no. 2, pp. 244–248, 1971.
- [90] M. Greenberg, *Advanced engineering mathematics*. Michigan, USA: Prentice Hall, November 1988.
- [91] W. Press, S. Teukolsky, W. Vetterling, and B. Flannery, *Numerical Recipes 3rd Edition: The Art of Scientific Computing*. Cambridge University Press, 3rd ed., 2007.
- [92] W. Swope, H. Andersen, P. Berens, and K. Wilson, "A computer simulation method for the calculation of equilibrium constants for the for-

- mation of physical clusters of molecules: Application to small water clusters," *J. Chem. Phys.*, vol. 76, no. 1, pp. 637–649, 1982.
- [93] R. Arévalo, *Dinámica microscópica en la descarga de silos y redes de fuerza en un medio granular rígido*. PhD thesis, Universidad de Navarra, 2009.
- [94] T. Sterling, "An introduction to pc clusters for high performance computing," *International Journal of High Performance Computing Applications*, vol. 15, pp. 92–101, May 2001.
- [95] D. Bader and R. Pennington, "Cluster computing: Applications," *International Journal of High Performance Computing Applications*, vol. 15, pp. 181–185, May 2001.
- [96] T. Rauber and G. Rünger, *Parallel Programming: for Multicore and Cluster Systems*. Springer, 2010.
- [97] J. Owens, D. Luebke, N. Govindaraju, M. Harris, J. Krüger, A. Lefohn, and T. Purcell, "A survey of general-purpose computation on graphics hardware," *Computer Graphics Forum*, vol. 26, pp. 80–113, March 2007.
- [98] J. Owens, M. Houston, D. Luebke, S. Green, J. Stone, and J. Phillips, "Gpu computing," *Proceedings of the IEEE*, vol. 96, pp. 879–899, May 2008.
- [99] J. Sanders and E. Kandrot, *CUDA by Example: An Introduction to General-Purpose GPU Programming*. Addison-Wesley Professional, 2010.
- [100] A. Grama, G. Karypis, V. Kumar, and A. Gupta, *Introduction to Parallel Computing*. Addison Wesley, 2nd ed., 2003.
- [101] J. England, "A system for interactive modeling of physical curved surface objects," *SIGGRAPH Comput. Graph.*, vol. 12, pp. 336–340, August 1978.
- [102] M. Potmesil and E. Hoffert, "The pixel machine: a parallel image computer," *SIGGRAPH Comput. Graph.*, vol. 23, pp. 69–78, July 1989.

- [103] J. Lengyel, M. Reichert, B. Donald, and D. Greenberg, "Real-time robot motion planning using rasterizing computer graphics hardware," *SIGGRAPH Comput. Graph.*, vol. 24, pp. 327–335, September 1990.
- [104] J. Rhoades, G. Turk, A. Bell, A. State, U. Neumann, and A. Varshney, "Real-time procedural textures," in *Proceedings of the 1992 symposium on Interactive 3D graphics, I3D '92*, (New York, NY, USA), pp. 95–100, ACM, 1992.
- [105] C. Trendall and A. Stewart, "General calculations using graphics hardware with applications to interactive caustics," in *Proceedings of the Eurographics Workshop on Rendering Techniques 2000*, (London, UK), pp. 287–298, Springer-Verlag, 2000.
- [106] M. Harris, G. Coombe, T. Scheuermann, and A. Lastra, "Physically-based visual simulation on graphics hardware," in *Proceedings of the ACM SIGGRAPH/EUROGRAPHICS conference on Graphics hardware, HWWS '02*, (Aire-la-Ville, Switzerland, Switzerland), pp. 109–118, Eurographics Association, 2002.
- [107] E. Lindholm, M. Kilgard, and H. Moreton, "A user-programmable vertex engine," in *Proceedings of the 28th annual conference on Computer graphics and interactive techniques, SIGGRAPH '01*, (New York, NY, USA), pp. 149–158, ACM, 2001.
- [108] NVIDIA, "Nvidia developer zone web page." <http://developer.nvidia.com/category/zone/cuda-zone>, September 2011.
- [109] AMD, "Amd accelerated parallel processing sdk." <http://developer.amd.com/sdks/AMDAPPSDK/Pages/default.aspx>, September 2011.
- [110] Khronos, "Opencl - the open standard for parallel programming of heterogeneous systems." <http://www.khronos.org/opencl/>, September 2011.

- [111] NVIDIA, *NVIDIA CUDA C Programming Guide*. NVIDIA Developer Zone, 2011.
- [112] NVIDIA, "Cuda gpus at nvidia developer zone." <http://developer.nvidia.com/cuda-gpus>, September 2011.
- [113] NVIDIA, "Nvidia gpu computing sdk web site." <http://developer.nvidia.com/gpu-computing-sdk>, September 2011.
- [114] C. Chang, Y. Chang, M. Huang, and B. Huang, "Accelerating regular ldpc code decoders on gpus," *IEEE Journal of Selected Topics in Applied Earth Observations and Remote Sensing*, vol. 4, no. 3, pp. 653–659, 2011.
- [115] J. Mielikainen, H. Bormin, and H. Huang, "Gpu-accelerated multi-profile radiative transfer model for the infrared atmospheric sounding interferometer," *IEEE Journal of Selected Topics in Applied Earth Observations and Remote Sensing*, vol. 4, no. 3, pp. 691–700, 2011.
- [116] E. Christophe, L. Michel, and J. Inglada, "Remote sensing processing: From multicore to gpu," *IEEE Journal of Selected Topics in Applied Earth Observations and Remote Sensing*, vol. 4, no. 3, pp. 643–652, 2011.
- [117] S. Changhe, L. Yunsong, and H. Bormin, "A gpu-accelerated wavelet decomposition system with spiht and reed-solomon decoding for satellite images," *IEEE Journal of Selected Topics in Applied Earth Observations and Remote Sensing*, vol. 4, no. 3, pp. 683–690, 2011.
- [118] J. Cui, G. Pratz, S. Prevrhal, and C. Levin, "Fully 3d list-mode time-of-flight pet image reconstruction on gpus using cuda," *Med. Phys.*, vol. 38, no. 12, pp. 6775–6786, 2011.
- [119] E. van Aart, N. S. A. Jalba, and A. Vilanova, "Cuda-accelerated geodesic ray-tracing for fiber tracking," *International Journal of Biomedical Imaging*, vol. 2011, p. 698908, 2011.

- [120] S. Park, B. Kim, L. Lee, J. Goo, and Y. Shin, "Ggo nodule volume-preserving nonrigid lung registration using glcm texture analysis," *IEEE Trans Biomed Eng.*, vol. 58, no. 10, pp. 2885–2894, 2011.
- [121] Z. Grof, J. Kosek, M. Marek, and P. Adler, "Modeling of morphogenesis of polyolefin particles: Catalyst fragmentation," *AIChE*, vol. 49, no. 4, pp. 1002–1013, 2003.
- [122] L. Oddershede, P. Dimon, and J. Bohr, "Self-organized criticality in fragmenting," *Phys. Rev. Lett.*, vol. 71, no. 19, pp. 3107–3110, 1993.
- [123] F. Wittel, F. Kun, H. Herrmann, and B. Kröplin, "Fragmentation of shells," *Phys. Rev. Lett.*, vol. 93, no. 3, p. 035504, 2004.
- [124] F. Kun, F. Wittel, H. Herrmann, B. K. K.J., and Måløy, "Scaling behavior of fragment shapes," *Phys. Rev. Lett.*, vol. 96, no. 2, p. 025504, 2006.
- [125] D. Nesvorny, D. Vokrouhlicky, W. Bottke, and M. Sykes, "Physical properties of asteroid dust bands and their sources," *ICARUS*, vol. 181, no. 1, pp. 107–144, 2006.
- [126] A. Weber, U. Teipel, and H. Nirschl, "Comparison of comminution by impact of particle collectives and other grinding processes," *Chem. Eng. & Tech.*, vol. 29, no. 5, pp. 642–648, 2006.
- [127] O. Sotolongo-Costa, Y. Moreno-Vega, J. Lloveras-González, and J. Antoranz, "Criticality in droplet fragmentation," *Phys. Rev. Lett.*, vol. 76, no. 1, pp. 42–45, 1996.
- [128] T. Jiang and J. Northby, "Fragmentation clusters formed in supercritical expansions of ^4He ," *Phys. Rev. Lett.*, vol. 68, no. 17, pp. 2620–2623, 1992.
- [129] S. Redner, *Statistical Models for the Fracture of Disordered Media*, ch. Fragmentation. Amsterdam: Elsevier Science Pubs, North-Holland, 1990.
- [130] E. McGrady and R. Ziff, "'shattering" transition in fragmentation," *Phys. Rev. Lett.*, vol. 58, no. 9, pp. 892–895, 1987.

- [131] Z. Cheng and S. Redner, "Kinetics of fragmentation," *J. Phys. A*, vol. 23, no. 7, p. 1233, 1990.
- [132] M. Ernst and G. Szamel, "Fragmentation kinetics," *J. Phys. A*, vol. 26, no. 22, p. 6085, 1993.
- [133] P. Krapivsky and E. Ben-Naim, "Shattering transitions in collision-induced fragmentation," *Phys. Rev. E*, vol. 68, no. 2, p. 021102, 2003.
- [134] M. Ernst and I. Pagonabarraga, "The nonlinear fragmentation equation," *J. Phys. A*, vol. 40, no. 17, p. F331, 2007.
- [135] J. Aström, "Statistical models of brittle fragmentation," *Adv. Phys.*, vol. 55, no. 3–4, pp. 247–278, 2006.
- [136] F. Spahn, N. Albers, M. Sremcevic, and C. Thornton, "Kinetic description of coagulation and fragmentation in dilute granular particle ensembles," *Europhys. Lett.*, vol. 67, no. 4, p. 545, 2004.
- [137] I. Pagonabarraga and E. Trizac, *Granular Gas Dynamics*, vol. 624, ch. Kinetics of Fragmenting Freely Evolving Granular Gases, pp. 163–184. Berlin: Springer-Verlag, 2003.
- [138] R. Hidalgo and I. Pagonabarraga, "Fragmenting granular gases," *Europhys. Lett.*, vol. 77, no. 6, p. 64001, 2007.
- [139] R. Hidalgo and I. Pagonabarraga, "Driven fragmentation of granular gases," *Phys. Rev. E*, vol. 77, no. 6, p. 061305, 2008.
- [140] P. van Dongen and M. Ernst, "Dynamic scaling in the kinetics of clustering," *Phys. Rev. Lett.*, vol. 54, no. 13, pp. 1396–1399, 1985.
- [141] P. van Dongen and M. Ernst, "Kinetics of reversible polymerization," *J. Stat. Physics*, vol. 37, no. 3–4, pp. 301–324, 1984.
- [142] P. van Dongen and M. Ernst, "Cluster size distribution in irreversible aggregation at large times," *J. Phys. A*, vol. 18, no. 14, p. 2779, 1985.

- [143] G. Bird, *Molecular Gas Dynamics and the Direct Simulation of Gas Flows*. USA: Oxford University Press, 2nd ed., 1994.
- [144] V. Garzó and A. Santos, *Kinetic Theory of Gases in Shear Flows. Nonlinear Transport*. Springer, September 2003.
- [145] J. Montanero and V. Garzó, "Monte carlo simulation of the homogeneous cooling state for a granular mixture," *Granular Matter*, vol. 4, no. 1, pp. 17–24, 2002.
- [146] G. Hidy and J. Brock, eds., *Topics in current aerosol research, Part II*. Pergamon Press, 1972.
- [147] J. Brey, M. Ruiz-Montero, and D. Cubero, "Homogeneous cooling state of a low-density granular flow," *Phys. Rev. E*, vol. 54, p. 3664, 1996.
- [148] V. Garzó and J. Dufty, "Homogeneous cooling state for a granular mixture," *Phys. Rev. E*, vol. 60, pp. 5706–5713, Nov 1999.
- [149] J. Brey, M. G. de Soria, P. Maynar, and M. Ruiz-Montero, "Energy fluctuations in the homogeneous cooling state of granular gases," *Phys. Rev. E*, vol. 70, p. 011302, 2004.
- [150] P. Haff, "Grain flow as a fluid-mechanical phenomenon," *Journal of Fluid Mechanics*, vol. 134, pp. 401–430, 1983.
- [151] C. C. Maaß, N. Isert, G. Maret, and C. Aegerter, "Experimental investigation of the freely cooling granular gas," *Phys. Rev. Lett.*, vol. 100, p. 248001, 2008.
- [152] X. Nie, E. Ben-Naim, and S. Chen, "Dynamics of freely cooling granular gases," *Phys. Rev. Lett.*, vol. 89, no. 20, p. 204301, 2002. e-print cond-mat/0209412.
- [153] A. Puglisi, V. Loreto, U. M. B. Marconi, A. Petri, and A. Vulpiani, "Clustering and non-gaussian behavior in granular matter," *Phys. Rev. Lett.*, vol. 81, no. 18, pp. 3848–3851, 1998.

- [154] S. Luding and H. Herrmann, "Cluster-growth in freely cooling granular media," *Chaos: An Interdisciplinary Journal of Nonlinear Science*, vol. 9, pp. 673–681, 1999.
- [155] I. Aranson and L. Tsimring, "Patterns and collective behavior in granular media: Theoretical concepts," *Rev. Mod. Phys.*, vol. 78, p. 641, 2006.
- [156] M. Shinde, D. Das, and R. Rajesh, "Equivalence of the freely cooling granular gas to the sticky gas," *Phys. Rev. E*, vol. 79, p. 021303, 2009.
- [157] N. Brilliantov, F. Spahn, J. Hertzsch, and T. Pöschel, "Model for collisions in granular gases," *Phys. Rev. E*, vol. 53, no. 5, p. 5382, 1996.
- [158] A. Bodrova and N. Brilliantov, "Cooling kinetics of a granular gas of viscoelastic particles," *Moscow University Physics Bulletin*, vol. 64, p. 2, 2009.
- [159] N. Brilliantov, C. S. na, T. Schwager, and T. Pöschel, "Transient structures in a granular gas," *Phys. Rev. Lett.*, vol. 93, p. 134301, 2004.
- [160] N. Brilliantov, T. Pöschel, W. Kranz, and A. Zippelius, "Translations and rotations are correlated in granular gases," *Phys. Rev. Lett.*, vol. 98, p. 128001, 2007.
- [161] S. Ulrich, T. Aspelmeier, A. Zippelius, K. Roeller, A. Fingerle, and S. Herminghaus, "Dilute wet granular particles: Nonequilibrium dynamics and structure formation," *Phys. Rev. E*, vol. 80, p. 031306, 2009.
- [162] F. Affouard, M. Kröger, and S. Hess, "Molecular dynamics of model liquid crystals composed of semiflexible molecules," *Phys. Rev. E*, vol. 54, pp. 5178–5186, 1996.
- [163] F. Villarruel, B. Lauderdale, D. Mueth, and H. Jaeger, "Compaction of rods: Relaxation and ordering in vibrated, anisotropic granular material," *Phys. Rev. E*, vol. 61, p. 6914, 2000.
- [164] A. Wouterse, S. Luding, and A. Philipse, "On contact numbers in random rod packings," *Granular Matter*, vol. 11, p. 169, 2009.

- [165] E. Azéma, F. Radjai, and G. Saussine, "Quasistatic rheology, force transmission and fabric properties of a packing of irregular polyhedral particles," *Mechanics of Materials*, vol. 41, p. 729, 2009.
- [166] R. Hidalgo, I. Zuriguel, D. Maza, and I. Pagonabarraga, "Role of particle shape on the stress propagation in granular packings," *Phys. Rev. Lett.*, vol. 103, p. 118001, 2009.
- [167] F. Alonso-Marroquín, "Spheropolygons: A new method to simulate conservative and dissipative interactions between 2d complex-shaped rigid bodies," *Europhys. Lett.*, vol. 83, p. 14001, 2008.
- [168] A. Kudrolli, G. Lumay, D. Volfson, and L. Tsimring, "Swarming and swirling in self-propelled polar granular rods," *Phys. Rev. Lett.*, vol. 100, p. 058001, 2008.
- [169] F. Peruani, A. Deutsch, and M. Bär, "Nonequilibrium clustering of self-propelled rods," *Phys. Rev. E*, vol. 74, p. 030904, 2006.
- [170] D. Helbing, "Traffic and related self-driven many-particle systems," *Rev. Mod. Phys.*, vol. 73, pp. 1067–1141, 2001.
- [171] E. Ben-Jacoba, I. Cohena, and H. Levineb, "Cooperative self-organization of microorganisms," *Advances in Physics*, vol. 49, pp. 395–554, 2000.
- [172] N. Brilliantov, "Hydrodynamics of granular gases of viscoelastic particles," *Phil. Trans.: Math. Phys. Eng. Sci.*, vol. 360, pp. 415–428, 2002.
- [173] T. van Noije, M. Ernst, E. Trizac, and I. Pagonabarraga, "Randomly driven granular fluids: Large-scale structure," *Phys. Rev. E*, vol. 59, no. 4, pp. 4326–4341, 1999.
- [174] P. Cleary and M. Sawley, "Dem modelling of industrial granular flows: 3d case studies and the effect of particle shape on hopper discharge," *Appl. Math. Modell.*, vol. 26, no. 2, pp. 89–111, 2002.
- [175] Z. Zhong, J. Ooi, and J. Rotter, "The sensitivity of silo flow and wall stresses to filling method," *Eng. Struct.*, vol. 23, p. 756, 2001.

- [176] P. Langston, U. Tüzün, and D. Heyes, “Discrete element simulation of granular flow in 2d and 3d hoppers: Dependence of discharge rate and wall stress on particle interactions,” *Chem. Engin. Sci.*, vol. 50, no. 6, pp. 967–987, 1995.
- [177] J. Rotter, J. Holst, J. Ooi, and A. Sanad, “Silo pressure predictions using discrete,Äielement and finite,Äielement analyses,” *Phil. Trans. R. Soc. Lond. A*, vol. 356, no. 1747, pp. 2685–2712, 1998.
- [178] M. Guaita, A. Couto, and F. Ayuga, “Numerical simulation of wall pressure during discharge of granular material from cylindrical silos with eccentric hoppers,” *Biosyst. Engin.*, vol. 85, no. 1, pp. 101–109, 2003.
- [179] R. Hidalgo, I. Zuriguel, D. Maza, and I. Pagonabarraga, “Granular packings of elongated faceted particles deposited under gravity,” *J. Stat. Mech.*, vol. 2010, p. P06025, 2010.
- [180] A. Janda, I. Zuriguel, A. Garcimartín, L. Pugnaloni, and D. Maza, “Jamming and critical outlet size in the discharge of a two-dimensional silo,” *Europhys. Lett.*, vol. 84, p. 44002, 2008.
- [181] F. Alonso-Marroquín and Y. Wang, “An efficient algorithm for granular dynamics simulations with complex-shaped objects,” *Granular Matter*, vol. 11, pp. 317–329, 2009.
- [182] L. Landau and E. Lifshitz, *Theory of Elasticity, Third Edition*. Butterworth-Heinemann, 1986.
- [183] G. Duvaut and J.-L. Lions, *Les Inéquations en Mécanique et en Physique*. Dunod, Paris, 1972.
- [184] K. Stokely, A. Diacou, and S. Franklin, “Two-dimensional packing in prolate granular materials,” *Phys. Rev. E*, vol. 67, no. 5, p. 051302, 2003.
- [185] I. Bartos and I. Jánosi, “Side pressure anomalies in 2d packings of frictionless spheres,” *Granular Matter*, vol. 9, pp. 81–86, 2007.
- [186] I. Zuriguel, T. Mullin, and R. Arévalo, “Stress dip under a two-dimensional semipile of grains,” *Phys. Rev. E*, vol. 77, p. 061307, 2008.

- [187] B. Glasser and I. Goldhirsch, "Scale dependence, correlations, and fluctuations of stresses in rapid granular flows," *Phys. Fluids*, vol. 13, no. 2, p. 407, 2001.
- [188] I. Goldhirsch and C. Goldenberg, "On the microscopic foundations of elasticity," *Eur. Phys. J. E*, vol. 9, no. 3, pp. 245–251, 2002.
- [189] M. Lätzel, S. Luding, and H. Herrmann, "Macroscopic material properties from quasi-static, microscopic simulations of a two-dimensional shear-cell," *Granular Matter*, vol. 2, no. 3, pp. 123–135, 2000.
- [190] M. Madadi, O. Tsoungui, M. Lätzel, and S. Luding, "On the fabric tensor of polydisperse granular materials in 2d," *Int. J. Solids and Struct.*, vol. 41, pp. 2563–2580, 2004.
- [191] H. Janssen, "Versuche über getreidedruck in silozellen," *Z. Vereines Deutsch. Ingen.*, vol. 39, p. 1045, 1895.
- [192] M. Sperl, "Experiments on corn pressure in silo cells ,À translation and comment of janssen's paper from 1895," *Granular Matter*, vol. 8, no. 2, pp. 59–65, 2006.
- [193] J. Mitchell and K. Soga, *Fundamentals of Soil Behavior*. New Jersey, USA: Wiley, 3rd ed., May 2005.
- [194] L. Barden, A. McGown, and K. Collins, "The collapse mechanism in partly saturated soil," *Engineering Geology*, vol. 7, no. 1, pp. 49–60, 1973.
- [195] A. Assallay, C. Rogers, and I. Smalley, "Formation and collapse of metastable particle packings and open structures in loess deposits," *Engineering Geology*, vol. 48, no. 1–2, pp. 101–115, 1997.
- [196] Y. Reznik, "A method for calculation of soil structural pressure values," *Engineering Geology*, vol. 78, no. 1–2, pp. 95–104, 2005.
- [197] P. Rognon, J.-N. Roux, D. Wolf, M. Naaim, and F. Chevoir, "Rheophysics of cohesive granular materials," *Europhys. Lett.*, vol. 74, no. 4, p. 644, 2006.

- [198] D. Kadau, L. Brendel, G. Bartels, D. Wolf, M. Morgeneyer, and J. Schwedes, "Macroscopic and microscopic investigation on the history dependence of the mechanical properties of powders," *Chemical Engineering Transactions*, vol. 3, pp. 979–984, 2003.
- [199] M. Röck, M. Morgeneyer, J. Schwedes, D. Kadau, L. Brendel, and D. Wolf, "Steady state flow of cohesive and non-cohesive powders. investigations in experiment and simulation," *Granular Matter*, vol. 10, no. 4, pp. 285–293, 2008.
- [200] N. Wagner and J. Brady, "Shear thickening in colloidal dispersions," *Physics Today*, vol. 62, no. 10, p. 27, 2009.
- [201] E. del Gado and W. Kob, "A microscopic model for colloidal gels with directional effective interactions: network induced glassy dynamics," *Soft Matter*, vol. 6, no. 7, pp. 1547–1558, 2010.
- [202] D. Kadau, H. Herrmann, J. Andrade, A. Araújo, L. Bezerra, and L. Maia, "Living quicksand," *Brief Communications to Granular Matter*, vol. 11, no. 1, pp. 67–71, 2009.
- [203] D. Kadau, J. Andrade, and H. Herrmann, "Collapsing granular suspensions," *Eur. Phys. J. E*, vol. 30, no. 3, pp. 275–281, 2009.
- [204] D. Kadau, H. Herrmann, and J. Andrade, "Mechanical behavior of "living quicksand": Simulation and experiment," *AIP Conf. Proc.*, vol. 1145, pp. 981–984, July 2009.
- [205] D. Kadau, "From powders to collapsing soil, à living quicksand: Discrete modeling and experiment," *AIP Conf. Proc.*, vol. 1227, pp. 50–57, September 2009.
- [206] D. Kadau, G. Bartels, L. Brendel, and D. Wolf, "Pore stabilization in cohesive granular systems," *Phase Transit.*, vol. 76, no. 4–5, pp. 315–331, 2003.

- [207] D. Kadau, G. Bartels, L. Brendel, and D. Wolf, "Contact dynamics simulations of compacting cohesive granular systems," *Comp. Phys. Comm.*, vol. 147, no. 1–2, pp. 190–193, 2002.
- [208] G. Bartels, T. Unger, D. Kadau, D. Wolf, and J. Kertész, "The effect of contact torques on porosity of cohesive powders," *Granular Matter*, vol. 7, no. 2–3, pp. 139–143, 2005.
- [209] D. Kadau and H. Herrmann, "Density profiles of loose and collapsed cohesive granular structures generated by ballistic deposition," *Phys. Rev. E*, vol. 83, no. 3, p. 031301, 2011.
- [210] O. Ditlevsen and K. Berntsen, "Empirically based gamma-distributed random wall pressure field in silo," *J. Eng. Mech.*, vol. 125, no. 5, pp. 561–569, 1999.
- [211] C. Goldenberg, A. Atman, P. Claudin, G. Combe, and I. Goldhirsch, "Scale separation in granular packings: Stress plateaus and fluctuations," *Phys. Rev. Lett.*, vol. 96, no. 16, p. 168001, 2006.
- [212] S. Green, "Particle simulation using cuda," tech. rep., NVIDIA Corporation, Santa Clara, USA, May 2010.
- [213] Q. Hou, K. Zhou, and B. Guo, "Bsgp: bulk-synchronous gpu programming," in *ACM Transactions on Graphics (TOG) - Proceedings of ACM SIGGRAPH 2008*, vol. 27, (NY, USA), ACM New York, August 2008.
- [214] J. Kuipers, *Quaternions and rotation sequences: a primer with applications to orbits, aerospace, and virtual reality*. Princeton University Press, 2002.
- [215] D. Evans, "On the representation of orientation space," *Molecular Physics*, vol. 34, pp. 317–325, 1977.
- [216] D. Evans and S. Murad, "Singularity free algorithm for molecular dynamic simulation of rigid polyatomic," *Molecular Physics*, vol. 34, pp. 327–331, 1977.

- [217] D. Fincham, "Leapfrog rotational algorithms," *Molecular Simulation*, vol. 8, no. 3-5, pp. 165-178, 1992.